Axions, Strings, and Dark-Matter Cosmology

TECHNISCHE
UNIVERSITÄT
DARMSTADT

Institut für Kernphysik AG Moore
Fachbereich Physik

Axions, Strings, and Dark-Matter Cosmology
Kosmologische Axionen, Strings und dunkle Materie

Genehmigte Dissertation von Vincent Benedikt Klaer aus Duisburg

1. Gutachten: Prof. Ph.D. Guy David Moore
2. Gutachten: Prof. Dr. phil. nat. Tetyana Galatyuk

Tag der Einreichung: 15.10.2019
Tag der Prüfung: 18.11.2019

Darmstadt — D 17

Erklärung zur Dissertation

Hiermit versichere ich, die vorliegende Dissertation ohne Hilfe Dritter nur mit den angegebenen Quellen und Hilfsmitteln angefertigt zu haben. Alle Stellen, die aus Quellen entnommen wurden, sind als solche kenntlich gemacht. Diese Arbeit hat in gleicher oder ähnlicher Form noch keiner Prüfungsbehörde vorgelegen.

Darmstadt, den 15.10.2019

_____

(Vincent Benedikt Klaer)

Zusammenfassung

Die Existenz dunkler Materie ist eines der ungelösten fundamentalen Probleme der Physik und kann nicht durch etablierte Theorien, wie die Allgemeine Relativitätstheorie oder das Standardmodell der Teilchenphysik, erklärt werden. Allerdings kann eine Erweiterung der Quantenchromodynamik (QCD), ein Teil des Standardmodells, eine Erklärung für dunkle Materie liefern. Es ist bekannt, dass die QCD invariant unter Ladungs- und Paritätssymmetrie (CP-Symmetrie) ist, wobei die Verletzung der Symmetrie durch den Parameter θ quantifiziert wird. Die Invarianz der QCD unter CP-Transformation ist nicht explizit gefordert, sondern nur implizit durch den verschwindenden θ-Parameter erfüllt.

Diese willkürlich erscheinende Erhaltung der CP-Symmetrie ist als das starke CP-Problem bekannt. Eine mögliche Lösung zu diesem Problem wurde von Peccei und Quinn vorgestellt, die den θ-Parameter nicht als Konstante, sondern als dynamisches Feld betrachten. Dies erfordert ein neues Teilchen, welches extrem leicht ist und kaum mit der uns bekannten Materie wechselwirkt, so wie es auch von dunkler Materie erwartet wird. Dieses neue Teilchen mit dem Namen Axion löst somit potentiell zwei Probleme: das starke CP-Problem sowie den Ursprung dunkler Materie.

Bis heute ist es allerdings nicht gelungen, dieses hypothetische Teilchen experimentell nachzuweisen. Das liegt mitunter daran, dass es nur sehr schwach wechselwirkt und somit sehr komplexe experimentelle Aufbauten für eine erfolgreiche Messung benötigt werden. Zusätzlich existieren nur wenige präzise theoretische Vorhersagen für die Masse des Axions, was die Suche erschwert.

In dieser Arbeit stellen wir eine neue Methode zur Bestimmung der Axionmasse vor. Diese ist erstmals in der Lage die verantwortlichen Produktionsmechanismen korrekt zu beschreiben und einen präzisen Wert der Axionmasse durch Gittersimulationen vorherzusagen. Die Herausforderung liegt in der korrekten Beschreibung der Produktionsmechanismen, genauer in der Simulation der korrekten String-Spannung. Zusätzlich werden neue Methoden zur mikroskopischen Untersuchung der String-Dynamik selbst vorgestellt, mit der zum ersten Mal theoretische Bewegungsgleichungen simuliert und verglichen werden können. Dies gibt ebenfalls Aufschluss über die Zuverlässigkeit der String-Simulation im Allgemeinen.

Abstract

The existence of dark matter is one of the unsolved fundamental problems of physics and cannot be explained by established theories such as general relativity or the standard model of particle physics. However, an extension of Quantum Chromodynamics (QCD), a part of the Standard Model, can explain dark matter. It is known that QCD is invariant under charge and parity symmetry (CP symmetry), the violation of symmetry is quantified by the parameter θ. The invariance of the QCD under CP transformations is not explicitly required, but only implicitly fulfilled by a very small θ parameter.

This seemingly arbitrary conservation of CP symmetry is known as the strong CP problem. A promising solution to this problem was presented by Peccei and Quinn, who consider the θ parameter not as a constant, but as a dynamical field. This requires a new particle that is extremely light and hardly interacts with the matter we know, as it is expected for dark matter. Therefore, this new particle, called axion, potentially solves two problems; the strong CP problem and the origin of dark matter.

To date, however, it was not possible to detect this hypothetical particle experimentally, which is, if the particle exist, because of its very weak interaction and therefore very complex experimental set-ups are required for a successful measurement. In addition, there are only a few precise theoretical predictions for the mass of the axion.

In this thesis we present a new method to determine the axion mass. This method is able to correctly describe the responsible production mechanisms for the first time and thus predict a precise value of the axion mass by lattice simulations. The challenge lies in the correct description of the production mechanisms, more precisely in the simulation of the correct string tension. Moreover we also present new methods for the microscopic investigation of the string dynamics themselves, with which theoretical equations of motion can be simulated and compared for the first time. This also provides information about the reliability of string simulations in general.

Contents

Preface

Partial results of the present work were published in advance in the following articles

- V.B.Klaer and G.D.Moore, "*How to simulate global cosmic strings with large string tension*",
  JCAP 1710 (2017) 043
  [arXiv:1708.07521]: Chapter 5.3

- V.B.Klaer and G.D.Moore, "*The dark-matter axion mass*",
  JCAP 1711 (2017) no.11, 049
  [arXiv:1707.05566]: Chapter 8

Due to stylistic reasons, the work is written in the first-person plural.

Chapter 1

Introduction

The universe consists of about 5% baryonic matter, 25% dark matter and 70% dark energy [1, 2]. While baryonic matter can be well described within the Standard Model (SM) of particle physics [3], there is no such description for dark matter and dark energy. All that is known about dark matter so far, is that it interacts almost only gravitationally, and that it is cold and therefore almost pressureless. A potential theory for dark matter can be an extension of quantum chromodynamics (QCD), which is part of the SM. QCD involves a term that breaks charge and parity (CP symmetry). However, the contribution of the term is weighted by the parameter $\bar{\theta}_3$ and is in order of 10^{-10}. The question of the parameter being so small is called the strong CP problem [4]. A possible solution was provided by Peccei and Quinn [5], who considered $\bar{\theta}_3$ not as a constant but as a field, thus introducing a new particle. This new particle, known as the axion, behaves similarly to dark matter. Thus, this approach solves two problems: the conservation of CP invariance and the consistency of dark matter. In this thesis we deal with the development and the determination of the mass of the axion, as well as a detailed studies of the axion production mechanisms.

In general, four fundamental interactions are known: these are the gravitational, electromagnetic, weak and strong interactions. The gravitational force has been known for thousands of years but was first expressed mathematically in 1687 by Isaac Newton. According to Newton's theory, the force between two bodies is inversely proportional to the square of their distances and accelerates towards the centre of mass. The basis of his theory includes an absolute space-time and therefore an absolute reference system, which was in contrast to the later measured constant speed of light. Albert Einstein claimed, after developing the Special Theory of Relativity, that there is no such absolute reference system. Additionally, Albert Einstein introduced the requirement that in all reference systems, whether accelerated or unaccelerated, the physical laws must take the same form, which led to his famous General Theory of Relativity in 1915. It describes gravity as a geometric property of the curved, four-dimensional space-time. The Einstein field equations can explain many physical effects like gravitational waves, black holes or gravitational lensing [6–8]. Einstein also introduced a cosmological constant Λ into his field equations to describe a static universe, which he later stated as his "biggest blunder". This cosmological constant is nowadays understood as the energy density of the vacuum, which is called dark energy [9].

Based on the brightness or redshift of distant type I supernovae, it can be seen that the universe is expanding with an accelerating rate. This can be described very well by the cosmological constant and is part of the successful Λ-CDM model, the standard model of cosmology, where CDM stands for cold dark matter [1]. First suggestions of dark matter were made by Kelvin in 1884. He observed the average velocity of stars orbiting around the center of the galaxy and estimated their mass. By doing so, he noticed differences between the mass of the observed stars and the mass estimated based on their average velocity. He therefore assumed that there had to be something like hidden stars which he named black bodies. Poincaré formed the term dark matter in discussing Kelvin's work [10]. First accepted studies about dark matter were made in the 1960's by Vera Rubin. Her measurements proved Kelvins observations of the too high orbital velocity of stars with increasing distance to the galaxy center [11].

The other three interactions can be summarized in the standard model (SM) of particle physics, which was invented in several steps by many physicists in the 1960's and 70's [3]. The standard model is a quantum field theory in which all particles are described as fields of the gauge symmetry group

$SU_c(3) \times SU_L(2) \times U_Y(1)$. It is constructed to satisfy the laws of special relativity and is invariant under charge, parity, and time reversal (CPT-symmetry). The force associated with the $SU_c(3)$ group is the strong interaction, which is described by Quantum Chromodynamics (QCD) and their massless gauge bosons are eight gluons G. The index c stands for color, since any particle which couples to gluons is interacting via the strong force and carries color. Since the standard model combines the weak and the electromagnetic interaction, the corresponding gauge bosons for these interactions can be derived from the group $SU_L(2) \times U_Y(1)$. Only left-handed fermions carry the quantum number of weak isospin, which is why it is denoted as L, where Y is associated with the quantum number of weak hypercharge. The model also contains a scalar field with a physical degree of freedom, the Higgs boson. This scalar field, the so called Higgs field, is responsible for the masses of the particles in the standard model. The standard model passed a lot of experimental tests in the last 40 years and last but not least the Higgs boson was discovered in 2012 as the last missing piece of the puzzle [12]. But as for any known current model, the standard model lacks some explanations like dark matter, matter anti-matter asymmetry or the neutrino oscillation [13].

In this work, the focus will be on dark matter. A lot of work is focused on finding an explanation for the constituents of dark matter and its direct detection. One can distinguish between baryonic dark matter and non-baryonic dark matter, where for baryonic matter the most promising candidate were the "Massive Astrophysical Compact Halo Objects" (MACHOs) [14]. These objects can be planets, brown dwarfs, black holes, white dwarfs or black dwarfs. It is assumed that only a little of the dark matter is made up by MACHOs, therefore it cannot solve the dark matter problem itself [15]. For non-baryonic matter "Weakly interacting massive particles" (WIMPs) were a promising candidate, since the supersymmetric extension of the standard model (SUSY) predicts particles with these properties. This is known as the WIMP miracle [16]. A little extension of the standard model gives another particle, which is called the axion [17], and will be of particular interest in this work. The name axion was chosen by Frank Wilczek after a detergent because it "cleans up" the strong CP problem in QCD [18].

In the standard model, only the CP violation by the phase of the Cabibbo-Kobayashi-Maskawa-Matrix (CKM) matrix is confirmed experimentally [19]. However, this is not the only contribution in the standard model that can lead to a violation of the CP symmetry. In addition, SU(3), SU(2) and U(1) have terms weighted by $\bar{\theta}_i$ that also break this symmetry. The contributions for SU(2) and U(1) can be shifted and are not physical and therefore do not contribute to a potential symmetry breaking. For $\bar{\theta}_3$ the term does not disappear after a shift, so this term has a physical contribution to the SM. A CP violating term in the QCD would cause an electrical dipole moment of the neutron which could then be measured. Recent experimental results show that $\bar{\theta}_3 \leq 1.97 \times 10^{-10}$ [20]. A solution for the strong CP problem was proposed by Roberto Peccei and Helen Quinn in 1978 [21]. They introduced a dynamical scalar field, which drives the evolution of the $\bar{\theta}_3$ parameter during time. The symmetry gets broken spontaneously and a Goldstone boson is generated, which is the axion. Since the symmetry is not exact, it has an explicit breaking term which turns the axion to a pseudo-goldstone boson which makes it massive [17]. The axion mass can be expressed by $m_a^2 = \chi / f_a^2$, where χ is the topological susceptibility of QCD and f_a the coupling of the axion [18, 22]. Experimental constraints restrict f_a to a range 10^8GeV and 10^{17}GeV, which causes the particle to be very light and barely interacting. This makes the axion to a perfect dark matter candidate which also solves the strong CP problem.

The mechanism of the PQ symmetry occurs over the cosmological time scale and can have started either before or after the inflation of the Universe [23]. Independent of the initial scenario for the breaking of the PQ symmetry, topological defects, like strings and domain walls will appear. If the symmetry breaking occurs before inflation, the contribution of the defects would be negligible, whereas if it appeared after inflation, the defects persist up to the baryonic freezout at Λ_{QCD}, where the axion starts to get massive. In both scenarios the misalignment mechanism is important for axion production. The topological defects which can appear are string and domain wall defects, where the domain walls start influencing the system at around $3\Lambda_{QCD}$ [23]. Both defects have an important contribution to the axion production [24–27]. The proposed PQ solution has a global U(1) symmetry and the equation of motion

can be simulated numerically on a lattice. Because of the spontaneous and explicit symmetry breaking these simulations build up a network of topological defects where strings appear first and after the tilt of the potential domain wall defects starts to affect the network.

The problem is that the string network evolution is not understood well enough. There is no consensus in the literature for the efficiency of axion production [26, 28–44]. Large-scale numerical simulations [24, 26] have not resolved this problem, because no simulation to date can correctly treat the tension of a global string. To see why this is a problem for simulations, consider the energy per length, or tension T, stored in the string, which is

$$T \equiv \pi f_a^2 \ln(m/H) = \pi f_a^2 \kappa \,, \tag{1.0.1}$$

where κ is the name of the magnitude of this logarithm, $H \sim 10^{-19}\,\mathrm{GeV}$ the Hubble parameter and $m \sim f_a \sim 10^{11}\,\mathrm{GeV}$ the saxion mass. Therefore the tension contains a logarithmically large factor $\ln(m/H)$, which, for the values quoted above, is $\ln(10^{30}) \simeq 70$. Comparing this value to achievable lattice simulations, maximum modern computers could go up to $\ln(10^4) \simeq 9$.

This huge difference is the string tension problem, which cannot be solved within the next centuries without a new method.

In this work, we present the first numerical simulation which solves the string tension problem and determines the axion mass. This is only valid if the PQ symmetry is broken after inflation and if the whole dark matter consists of axions. To achieve a deeper understanding of the behavior of string loops, we present two approaches to investigate strings on a more microscopic scale. First, a local string loop is cut from an evolving simulation and the string loop is rescaled and reevolved in a new simulation. The second approach constructs a single string on the lattice by using the Nambu-Goto solutions. The advantage of the second approach compared to the first one, is that the string trajectory for the Nambu-Goto string is known and can be compared. These constructed and cut strings are local strings and therefore their behaviors are not directly applicable to the global strings. However local strings are more robust since they do not have long range interactions, so they can be seen as a lower threshold for numerics with global strings.

The work is divided into two parts, where the first part discuss basic models and theories, which in turn are necessary to understand the numerical methods shown in the second part. In the second part, which begins with chapter 7, the results of these simulations are presented and discussed.

In chapter 2 the CP problem and the PQ solution is explained in more detail. A model developed by Kim-Shifan-Vainshtein-Zakharov (KSVZ), which integrates a light axion into the standard model Lagrangian is introduced. Experimental constraints for the axion mass as well as proposed experiments to detect the axion are discussed at the end of the second chapter.

The KSVZ model plays an important role for the axion cosmology, which is explained in chapter 3. The main important production mechanisms for the axion, such as topological defects, are shown in great detail as well as the different contributions of the production mechanisms for different cosmological scenarios. These topological defects are strings and domain walls, which appear if a symmetry gets spontaneously or explicitly broken. Additionally, it is described how the axion mass can be calculated by assuming that the current dark matter consists of axions.

Two effective field theories are described in chapter 4, which are the effective descriptions of local and global U(1) strings. Local strings are described by the Nambu-Goto action, if the string core is much smaller then the curvature radius of the string, whereas the Kalb-Ramond action describes global strings. With the Kalb-Ramond action we can create a model which can solve the string tension problem. The Nambu-Goto action is the basis for our string loop solution.

In chapter 5, global and local U(1) strings are explained in more detail. For extremely thin string cores compared to the string length, global strings should behave like local strings [29]. We also introduce

our novel two-Higgs model which posses a $U(1) \otimes U(1)$ symmetry and has two scalar fields and a gauge field. This model is capable of overcoming the string tension problem and therefore correctly yields the axion mass with the correct string tension.

The first part ends with chapter 6, where the string dynamics for Nambu-Goto strings are explained. The string loops introduced for flat spacetime should have an infinite lifetime and are used to initialize a string on the lattice. With this we can follow the expected and the simulated trajectory of the string.

The second part of the work, starting with chapter 7, begins with an introduction to the lattice discretization for a global U(1) theory. Here, we introduce the leapfrog algorithm to update the lattice.

The two-Higgs results are presented in chapter 8. We start by introducing the algorithm for lattice calculations and compare the new method with local and global simulations, which is done for string only networks. we then determine the specific parameters with the explicit breaking part of the potential, which leads to domain wall defects and annihilation of all string defects within a short time. After all topological defects are gone, the axion number density is extracted and the axion mass is estimated.

Surprisingly, the annihilation of strings does not produce many axions, which requires an investigation of strings in microscopic detail. This is done in chapter 9, where we investigate local strings, since the behavior of local and global strings should be the same for high tensional strings and the Nambu-Goto approximation for local strings is better understood as local strings do not have long range interactions. We present two ways to investigate single local strings. First, we discuss how to cut out a string at late times out of the lattice, refine the mesh it and reevolve the string. Since we do not know how the cut string should evolve, we secondly present a novel method to construct a string on the lattice by using the Nambu-Goto solution. With this method we can directly compare the lattice evolution with the Nambu-Goto solution.

Finally, the thesis is summarized in chapter 10, in which also an outlook for further investigation is given.

Chapter 2

Axions and the Strong CP Problem

In this chapter the focus is on the origin of the axion. Starting with the $U(1)_A$ problem which can be solved by instantons [18], where the instanton solution introduces a new quantity, which is the topological susceptibility $\chi(T)$ [45]. In addition, this solution generates the so called strong CP problem. This is solved by the PQ mechanism, which generates a new particle: the axion. The axion Lagrangian is derived by the "invisible" Kim-Shifan-Vainshtein-Zakharov (KSVZ) model, which also motivates the axion as a dark matter candidate. The Lagrangian is essential for the studies conducted in this thesis. Finally, existing and future experimental setups are presented, which constraints the axion mass.

2.1 Strong CP Problem

The theoretical framework of strongly interacting matter is Quantum Chromodynamics (QCD) [46]. The full Lagrangian of QCD can be written as

$$\mathscr{L}_{\mathrm{QCD}} = \mathscr{L}_{\mathrm{Gluon}} + \mathscr{L}_{\mathrm{Dirac}} + \mathscr{L}_{\mathrm{CP}}, \tag{2.1.1}$$

$$\mathscr{L}_{\mathrm{Gluon}} = -\frac{1}{4} G_a^{\mu\nu} G_{a,\mu\nu},$$

$$\mathscr{L}_{\mathrm{Dirac}} = \sum_f \bar{q}_f (i\slashed{D}_\mu - m_f) q_f,$$

$$\mathscr{L}_{\mathrm{CP}} = \bar{\theta}_3 \frac{g_3^2}{64\pi} \epsilon_{\mu\nu\alpha\beta} G_a^{\mu\nu} G_a^{\alpha\beta}.$$

The first term $\mathscr{L}_{\mathrm{Gluon}}$ is the gauge term of the local SU(3) gauge-group. $\mathscr{L}_{\mathrm{Dirac}}$ describes the interaction with quarks and $\mathscr{L}_{\mathrm{CP}}$ is the CP symmetry breaking term, which will be discussed in more detail.
We will sketch the derivation of the CP-breaking term by discussing the $U(1)_A$ problem of the flavor symmetry [47], where the resulting vanishing $\bar{\theta}_3$ term will be the strong CP problem [48]. If we consider the flavor symmetry, in the limit of massless quarks $m_f \to 0$ it results in a global group of vector and axial symmetries

$$U(N_f)_{\mathrm{L}} \otimes U(N_f)_{\mathrm{R}} \simeq SU(N_f)_{\mathrm{V}} \otimes SU(N_f)_{\mathrm{A}} \otimes U(1)_{\mathrm{V}} \otimes U(1)_{\mathrm{A}}. \tag{2.1.2}$$

For $N_f = 3$ the $U(1)_{\mathrm{V}}$ is an exact symmetry and corresponds to the baryon number. The $SU(3)_{\mathrm{V}}$ is slightly broken by differences in the quark masses and leads to the approximate symmetry of isospin and strangeness. For the axial symmetries[1], quark condensates $\langle \bar{u}u \rangle = \langle \bar{d}d \rangle \neq 0$ break down the symmetry spontaneously which leads to the octet of the lightest pseudoscalar mesons which, in the chiral limit, are presumed to be the massless Goldstone bosons corresponding to the eight generators of $SU(3)_{\mathrm{A}}$. For the $U(1)_{\mathrm{A}}$ symmetry, one would expect all massless hadrons to have a partner of opposite parity, which is not the case for the η, η' pair. This mystery named the $\eta - \eta'$ mass splitting has no natural explanation

---

[1]   Only the whole product is homeomorph to the left expression. Particularly the axial group is not a group.

and Weinberg referred this as the $U(1)_A$ problem [47]. However, 't Hooft showed that the $U(1)_A$ is not a true symmetry of QCD by limiting the gauge fields to be pure gauge, that is

$$A_\mu = i U \partial_\mu U^\dagger, \tag{2.1.3}$$

where U is the unitary matrix which leads to instanton solutions if U is not the unit matrix. This leads to an and explicit broken $U(1)_A$ though the chiral anomaly [49,50]. This changes the classical topological trivial vacuum of QCD which was stated before to a topologically non-trivial vacuum. The homotopy classes of the solutions are distinguished by the topological charge or the Pontryagin index [22]

$$Q = \int d^4x \, q = \frac{g_3^2}{64\pi^2} \int d^4x \, G_{\mu\nu}^a \tilde{G}_{\mu\nu}^a. \tag{2.1.4}$$

The fluctuations of the topological charge can be expressed by the topological susceptibility, which will be discussed further in this chapter,

$$\chi = \int d^4x \, \langle q(x) q(0) \rangle. \tag{2.1.5}$$

The integral for the topological charge is in fact a total derivative which can be expressed by rewriting Eq. (2.1.4) as

$$Q = \int d^4x \, \partial_\mu K_\mu, \tag{2.1.6}$$

with

$$K_\mu \equiv \frac{g_3^2}{16\pi^2} \epsilon_{\mu\alpha\beta\gamma} \left(A_\alpha^a \partial_\beta A_\gamma^a + \frac{1}{3} f^{abc} A_\alpha^a A_\beta^b A_\gamma^c \right). \tag{2.1.7}$$

At spatial infinity the boundary conditions ensure vanishing contributions and the expression reduces to

$$Q = \int dt \frac{d}{dt} \int d^3x \, K_0 \equiv n_{CS}(t = \infty) - n_{CS}(t = -\infty), \tag{2.1.8}$$

where n_{CS} is called the Chern-Simons number. This implies that field configurations with $Q \neq 0$ connect different vacua via tunneling. For a gauge field configuration which leads to $Q = 1$ it is called an instanton where for $Q = -1$ an anti-instanton. The ground states are not described by any of the topological vacuum states of QCD solely, rather it is a superposition of all vacua. The sum of the eigenvalues of the gauge transformation can be written as

$$|\theta\rangle = \sum_{n=-\infty}^{\infty} e^{in\theta} |n\rangle, \tag{2.1.9}$$

which is known as the θ vacuum. It can be seen from this expression, that $|\theta\rangle = |\theta + 2\pi\rangle$, therefore the period of θ is 2π. The θ can be absorbed by a shift in θ_3 where the vacuum reduces to

$$|0\rangle = \sum_{n=-\infty}^{\infty} |n\rangle. \tag{2.1.10}$$

For the vacuum term the effective interaction is given by [22]

$$\mathcal{L}_{\theta_3} = \theta_3 q = \theta_3 \frac{g_3^2}{64\pi^2} G_{\mu\nu}^a \tilde{G}_{\mu\nu}^a. \tag{2.1.11}$$

This interaction only contributes by a total divergence but cannot be neglected since it provides a phase to any transition between two vacuum states and is therefore present due to the instanton solution. There is another contribution to the transition between the vacua, which is the coupling of fermions with instantons, which mediates the transition [51]. The full instanton process is associated with the phase

$$\bar{\theta}_3 = \theta_3 + \sum_q \arg(m_q) = \theta_3 + \arg \det M. \tag{2.1.12}$$

Only $\bar{\theta}_3$ remains unchanged by redefinition, that is the change of the quark-mass matrix is in the same amount as the change for the θ_3 term. Therefore the consequence of solving the $U(1)_A$ problem implies a new factor $\bar{\theta}_3$ which can be measured, since a CP-symmetry breaking term causes a neutron induced electric dipole moment (NEDM), parametrized by $\bar{\theta}_3$ which provides currently the strongest constraint [52]. The recent theoretical estimate for the dipole moment is [53]

$$|d_n| = 1.52(71) \times 10^{-16} \, e \, \mathrm{cm} \bar{\theta}_3. \tag{2.1.13}$$

It can be compared to the recent experimental limit of the NEDM [20]

$$|d_n| \le 3.0 \times 10^{-26} \, e \, \mathrm{cm} \, (90\% \, \mathrm{CL}). \tag{2.1.14}$$

and this leads to the upper bound of

$$|\bar{\theta}_3| \le 1.97 \times 10^{-10}. \tag{2.1.15}$$

Therefore the solution of the $U(1)_A$ problem faces a new problem of the question of why $\bar{\theta}_3$ is so small. This is known as the strong CP problem.

One promising explanation for the strong CP problem was proposed by Peccei and Quinn [5], which turns $\bar{\theta}_3$ to a dynamical field and introduces a pseudo scalar boson the axion [48], which will be discussed in the next section. There are more explanations for the strong CP problem [54–56] but most of them are ruled out. Therefore this work will focus on the PQ solution.

2.2 PQ Solution

The most popular solution to the strong CP problem was published by Peccei and Quinn. They proposed a dynamical scalar field, which breaks spontaneously a global $U(1)$ symmetry, namely, the $U(1)_{\mathrm{PQ}}$. $\bar{\theta}_3$ becomes the phase of the complex scalar field [5]. The axion field is the Goldstone boson of the broken $U(1)_{\mathrm{PQ}}$ symmetry and the transformation of the field $a(x)$ is

$$a(x) \to a(x) + \alpha f_a, \tag{2.2.1}$$

where f_a is the unknown axion decay constant. If the symmetry would be exact the axion would only couple through derivatives, but since it is assumed that it is broken by standard model anomalies, the allowed Lagrangian for the standard model can be written as [4]

$$\mathscr{L}_{\text{tot}} = \mathscr{L}_{\text{SM}} + \bar{\theta}_3 \frac{g_3^2}{64\pi^2} G_b^{\mu\nu} \tilde{G}_{b\mu\nu} + \mathscr{L}_a, \tag{2.2.2}$$

$$\mathscr{L}_a = -\frac{1}{2}\partial^\mu a \partial_\mu a + J^\mu \partial_\mu a - \frac{a}{64\pi^2 f_a}\left[N g_3^2 G_b^{\mu\nu}\tilde{G}_{b\mu\nu} - k_2 g_2^2 W_b^{\mu\nu}\tilde{W}_{b\mu\nu} - k_1 g_1^2 B^{\mu\nu}\tilde{B}_{\mu\nu}\right]. \tag{2.2.3}$$

The constants k_1 and k_2 express the electroweak anomaly part for the axion symmetry, where B and W are the generators of the electroweak theory. The Noether current for the axion depends on the standard-model fields and includes model-dependent dimensionless coefficients, which depend on how the symmetry acts on the various fields. These factors are important for a complete study of the axion mass and its detection. However, the CP problem gets solved by the strong interaction term which contains the needed current with the chiral anomaly

$$\partial_\mu J_{\text{PQ}}^\mu = \frac{a}{64\pi^2} N g_3^2 G_b^{\mu\nu}\tilde{G}_{b\mu\nu}. \tag{2.2.4}$$

This causes a shift in the QCD vacuum angle to

$$\bar{\theta}_{3,\text{eff}} = \bar{\theta}_3 + N\frac{\langle a \rangle}{f_a}, \tag{2.2.5}$$

with the VEV $\langle a \rangle$ of the axion field. The excitation above the VEV of the field is

$$\tilde{a} = a - \langle a \rangle, \tag{2.2.6}$$

where $\tilde{a}$ is then the physical axion field. Minimizing the potential generated by the QCD chiral anomaly leads to a VEV which is

$$\langle a \rangle = -\frac{\bar{\theta}_3 f_a}{N}, \tag{2.2.7}$$

and leads to a dynamical solution for the strong CP problem. The axion mass can be obtained by

$$m_a^2 = \left(\frac{\partial^2 V(\tilde{a})}{\partial^2 \tilde{a}}\right)\bigg|_{\langle a \rangle}, \tag{2.2.8}$$

which is the curvature of the effective potential. Due to the chiral anomaly, the axion is not a true Goldstone boson; rather, it is a pseudo-Goldstone boson, since it gets a tiny mass from the weak CP violation.

Because of the periodicity of $\bar{\theta}_3$ the axion field has degenerated minima with $2n\pi$ where $n \in \mathbb{Z}$. The simplest *Ansatz* for an axion potential is given by

$$V(\tilde{a}) = \frac{m_{\tilde{a}}^2 \tilde{a}^2}{2}, \tag{2.2.9}$$

which satisfies Eq. (2.2.8) but does not take account to the periodicity of the axion field. However there is the one-to-one correspondence between the form of the axion potential $V(\tilde{a})$ and the vacuum

energy of the fundamental QCD parameter $\bar{\theta}_3$, where it is shown that the $\bar{\theta}_3$ vacuum corresponds to $(1 - \cos(\bar{\theta}_3))$ [57]. The approximated axion potential can then expressed as

$$V(\tilde{a}) = \chi \left(1 - \cos\left(\frac{N\tilde{a}}{f_a} \right) \right), \tag{2.2.10}$$

where χ is the previous introduced topological susceptibility. Which is quite close to the leading order of the effective axion potential close to vacuum derived in [58]

$$V(a) = -m_\pi^2 f_\pi^2 \sqrt{1 - \frac{4m_u m_d}{(m_u + m_d)^2} \sin^2\left(\frac{a}{2f_a} \right)}, \tag{2.2.11}$$

where m_u, m_d and m_π are the quark and the pion mass.
Deriving the mass by using Eq. (2.2.8) and Eq. (2.2.10) we obtain

$$m_{\tilde{a}}^2 = \frac{N^2 \chi}{f_{\tilde{a}}^2}. \tag{2.2.12}$$

In the following we write $a = \tilde{a}$. The topological susceptibility is an aspect of current research and is actually temperature dependent [45]. For $T \ll T_C$, where T_C is the critical temperature of QCD, it has a constant behavior and is calculated to be [59]

$$\chi(T_0) = (75.44(34)\text{MeV})^4. \tag{2.2.13}$$

Above T_C it has a non-trivial behavior with

$$\chi(T) = T^{-\left(n + \frac{n_f}{3} \right)} \left(1.02(35)\,\text{GeV}^4 \right), \tag{2.2.14}$$

where $n \approx 7$ and n_f is the number of flavors. This approximation of the chiral susceptibility can be derived from the dilute instanton gas model [60] and is still an important question of the exact structure of the chiral susceptibility. Recent lattice studies predicts precise estimates for high temperatures $T > 1\,\text{GeV}$ [45, 61]. The first assumption was the PQWW model, they assumed for the symmetry breaking scale $f_a = v_F$ with $v_F \simeq 250\,\text{GeV}$, which is in the region of the electroweak symmetry breaking scale, but experiments have ruled out this assumption [62]. Nowadays, there are two important models, which expect an energy scale much higher than $250\,\text{GeV}$ and are called "invisible axions":

- **KSVZ-Model**: The Kim-Shifan-Vainshtein-Zakharov model introduces a heavy quark which carries PQ charge. The axion couples to the heavy quark at tree level. It only has induced couplings. [63, 64]

- **DFSZ-Model**: The Dine-Fishler-Srednicki-Zhitnitskii model introduces an additional Higgs doublet. The axion couples to standard model fermions at tree level, since they carry PQ charge. [65, 66].

Both models predict a very light, very weakly coupled and very long-lived axion, although they are not totally invisible [67]. These predictions fulfill all of the constraints for dark matter and therefore the axion is a dark matter candidate.

2.2.1 KSVZ Model

The KSVZ model introduces hadronic axions with only induced couplings to SM fermion. The new heavy quark Q and the complex field σ carries PQ charge. The singlet field σ interacts with the heavy quark Q via the Yukawa interaction, where its coupling to the invariant Q and the Higgs potential are

$$\mathscr{L}_Y = -f\bar{Q}_L\sigma Q_R - f^*\bar{Q}_R\sigma^*Q_L\,, \tag{2.2.15}$$

$$V(\phi,\sigma) = -\mu_\phi^2\phi^\dagger\phi - \mu_\sigma^2\sigma^*\sigma + \lambda_\phi(\phi^\dagger\phi)^2 + \lambda_\sigma(\sigma^*\sigma)^2 + \lambda_{\phi\sigma}\phi^\dagger\phi\sigma^*\sigma\,. \tag{2.2.16}$$

With f a complex coupling constant and ϕ the Higgs doublet in the standard model. The standard Higgs is mixed with σ but not with the axion field and can therefore be neglected. Under the $U(1)_{\text{PQ}}$ symmetry the fields transforms as

$$Q_L \to e^{\frac{i}{2}\alpha}Q_L\,, \tag{2.2.17}$$

$$Q_R \to e^{-\frac{i}{2}\alpha}Q_R\,, \tag{2.2.18}$$

$$\sigma \to e^{i\alpha}\,, \tag{2.2.19}$$

which are invariant expressions for Eq. (2.2.15) and Eq. (2.2.16). The anomaly part for the KSVZ axion can be expressed as

$$\mathscr{L}_{\text{anomaly}} = \frac{a}{f_a}\left(\frac{g_3}{64\pi}G_b^{\mu\nu}\tilde{G}_{b\mu\nu} + 3q_Q^2\frac{g_1}{4\pi}F^{\mu\nu}\tilde{F}_{\mu\nu}\right). \tag{2.2.20}$$

Therefore one can write with the kinetic term the effective KSVZ axion Lagrangian as

$$\mathscr{L}_a^{\text{KSVZ}} = \mathscr{L}_{\text{kin}} + \mathscr{L}_Y + \mathscr{L}_{\text{anomaly}}\,, \tag{2.2.21}$$

where the second part describes the interaction with electromagnetic fields. The $\mathscr{L}_a^{\text{KSVZ}}$ is added to the standard model and solves the strong CP problem. The axion Lagrangian can be summarized to

$$\mathscr{L}_a = (\partial_\mu\phi)^2 - \frac{\lambda}{8}(2\phi^*\phi - f_a^2)^2 - \frac{\lambda}{6}T^2|\phi|^2 - \chi(1 - \cos(N\arg(\phi)))\,. \tag{2.2.22}$$

The KSVZ axion mass can be computed by using Eq. (2.2.12) and Eq. (2.2.13) which yields [2]

$$m_a = 5.691(51)\mu\text{eV}\left(\frac{10^{12}\,\text{GeV}}{f_a}\right). \tag{2.2.23}$$

2.3 Experiments on Axions

A lot of experiments try to find the proposed axion. Using the PQ mechanism, one also can derive axion like particles (ALPs) with different theories. Even if we only consider the QCD-axion in this thesis, for the experimental review, we also take partly account of the ALPs. A good review of current experiments which this section follows, can be found in [68]. In table 2.1 possible detection methods are listed with

---

[2] The factor N is set to 1, due to the domain wall problem, which will be explained in the next chapter.

Table 2.1.: The first detection method block is refered to laboratory axions. The second block to solar axions and the third to dark matter axions [68].

Detection method	$g_{a\gamma}$	g_{ae}	g_{aN}	$g_{A\gamma n}$	$g_{a\gamma}g_{ae}$	$g_{a\gamma}g_{aN}$	$g_{ae}g_{aN}$	$g_N\bar{g}_N$	Model dependency
Light shining through wall	×								no
Polarization experiments	×								no
Spin-dependent 5th force			×				×	×	no
Helioscopes	×				×	×			Sun
Primakoff-Bragg in crystals	×				×				Sun
Underground ion. detectors	×	×	×			×	×		Sun
Haloscopes	×								DM
Pick up coil & LC circuit	×								DM
Dish antenna & dielectric	×								DM
DM-induced EDM (NMR)			×	×					DM
Spin precession in cavity		×							DM
Atomic transitions		×	×						DM

the specific axion to standard model particle interactions. We will only consider experiments which have direct photon coupling by

$$\mathscr{L}_{g_{a\gamma}} = g_{a\gamma} a \vec{E}\vec{B}, \tag{2.3.1}$$

where a is the axion field, $\vec{E}$ is the electrical and $\vec{B}$ the magnetic field. The coupling is

$$g_{a\gamma} = \frac{\alpha}{2\pi} \frac{C_{a\gamma}}{f_a}, \tag{2.3.2}$$

with α the fine structure constant and $C_{a\gamma}$ the model dependent factor

$$C_{a\gamma} = \frac{E}{N} - 1.92(4), \tag{2.3.3}$$

where the color and electric anomaly factors N and E are model dependent. For the KSVZ model the ratio is $\frac{E}{N} = 0$ whereas for the DFSZ I and DFSZ II model it is $\frac{E}{N} = \frac{8}{3}$ and $\frac{E}{N} = \frac{2}{3}$. The decay process of the axion to two photons, seen in figure 2.1, is strongly dependent on f_a and $C_{a\gamma}$.
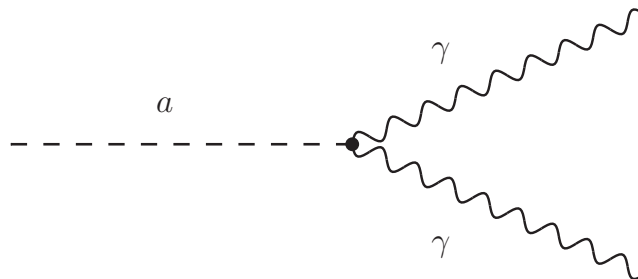

Figure 2.1.: Axion coupling to two photons
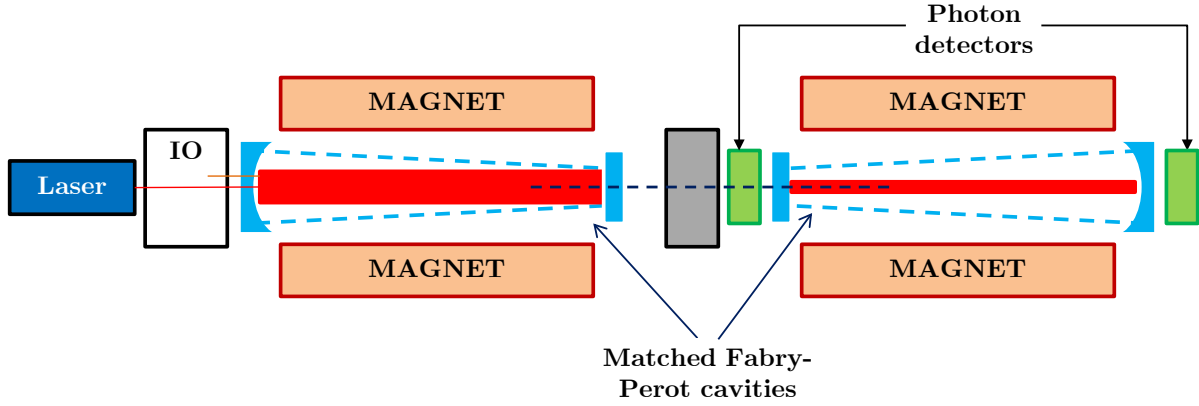
2.3.1 Light Shining Through Wall

Figure 2.2.: Figure taken from [69]. An experimental sketch of the light shining though wall experiment. It shows the principle of resonant photon regeneration. The Fabry-Perot cavities in both the production and regeneration regions must be actively locked in order to gain in sensitivity.

The light shining through wall experiments try to find the axion by converting it from a photon to an axion, let it pass through a wall and converting it back to a photon. Figure 2.2 shows a sketch of such an experiment, where on the left side the laser provides the photon source. The strength of the magnet has a direct influence on the probability of this process and can be written as

$$\mathscr{P}(\gamma \rightarrow a \rightarrow \gamma) = \mathscr{P}(\gamma \rightarrow a)\mathscr{P}(a \rightarrow \gamma) \propto C \left(g_{a\gamma} B_{\mathrm{e}} \right)^4 , \qquad (2.3.4)$$

where C is an experimental setup specific constant and B_{e} the external magnetic field. The limitation of these laboratory experiments is currently at around $g_{a\gamma} < 3.5 \times 10^{-8}\,\mathrm{GeV}^{-1}$ and set by the OSQAR (Optical Search for QED Vacuum Birefringence, Axions and Photon Regeneration) experiment in CERN [70]. The IAXO experiment aims in future with larger laser power and stronger magnets to reach up to $g_{a\gamma} \sim 3 \times 10^{-12}\,\mathrm{GeV}^{-1}$ [71].

2.3.2 Helioscope

Instead of using a laser beam as source for photons which then convert to axions, one uses the sun as an axion source and tries to convert them back to photons, see figure 2.3. Assuming that the energy of the reconverted photon is equal to the incoming axion, one expects energies of a few keV. The probability of this process is approximately

$$\mathscr{P}(a \rightarrow \gamma) \propto C \left(g_{a\gamma} B_{\mathrm{e}} \right)^2 , \qquad (2.3.5)$$

where again C is an experimental setup factor. The current constraints from the CAST (CERN Axion Solar Telescope) experiment are $g_{a\gamma} < 6.6 \times 10^{-11}\,\mathrm{GeV}^{-1}$, and the future experiments are planned to reach $g_{a\gamma} \sim 10^{-12}\,\mathrm{GeV}^{-1}$ [71, 72].

2.3.3 Haloscope

The haloscope experiments can be distinguished between conventional and dielectric haloscope experiments, where both use the Primakoff process in which axions get converted to photons due to the presence of a magnetic field. The conventional haloscope uses a cavity resonator. The frequency of the
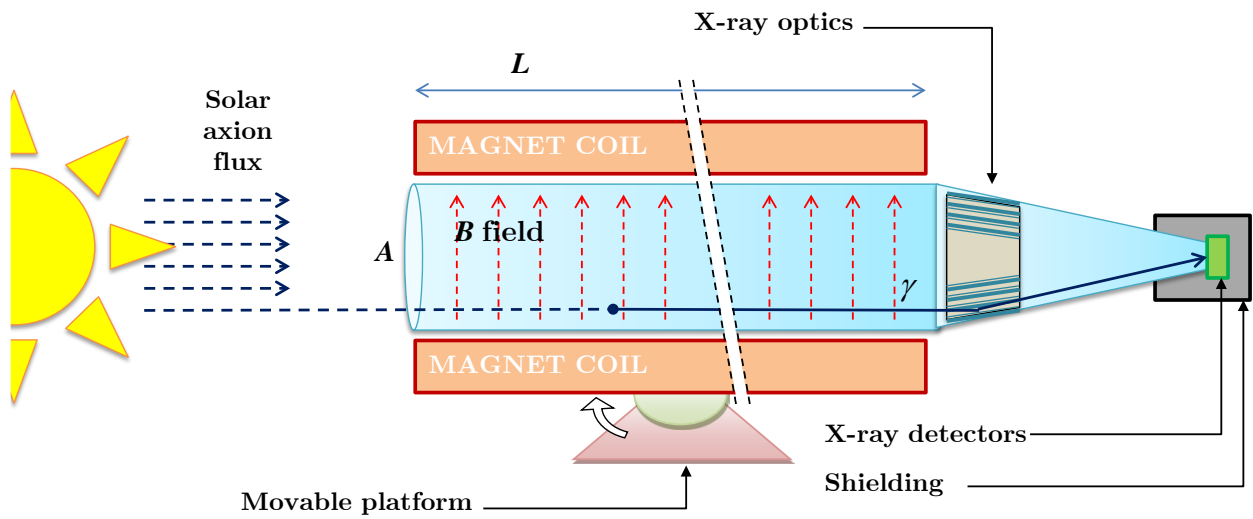
Figure 2.3.: Figure taken from [68]. It sketches a solar axion experiment of an axion helioscope with X-ray focusing. The quasi-parallel beam of photons , which is achieved by converting solar axions into photons by a magnetic field, is concentrated by an appropriate X-ray optics onto a small spot area.
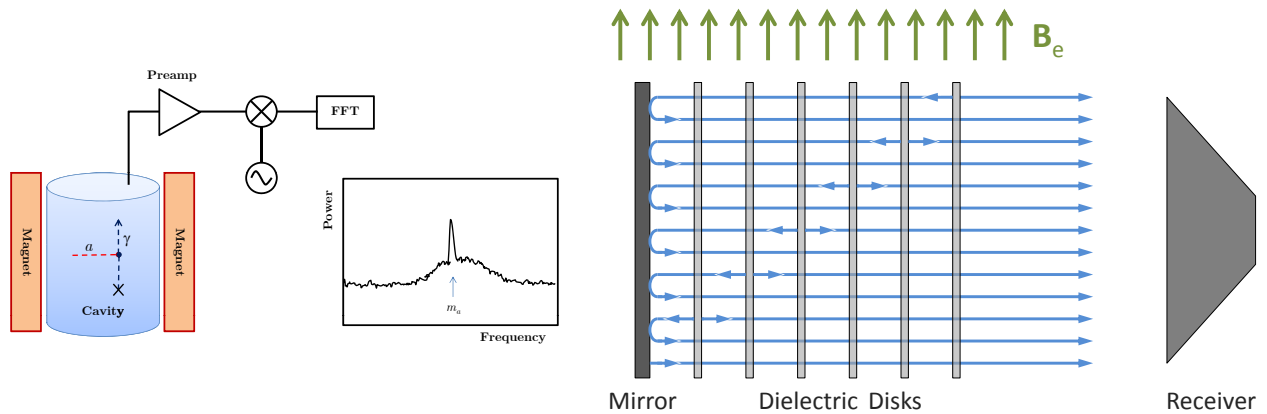

Figure 2.4.: Left the conventional haloscope, taken from [68]. Right the dielectric haloscope with multiple disk to enlarge the range, taken from [73]

cavity must match to the unknown axion mass within an error of $\sim m_a/Q$, where Q is the quality factor of the cavity. If one would like to test a large bandwidth of frequencies, the design of the experiment needs to be tunable to different frequencies. If the frequency matches to the axion mass m_a, the conversion is enhanced by a factor $m_a + m_a/Q$. Getting to smaller and smaller frequencies, the requirement to the experiment is more and more challenging, since the sensitivity of the experiments has dependences on the Volume and the Quality factor. The current Axion Dark Matter Experiment (ADMX) reaches frequencies in the range of 460 MHz to 890 MHz which corresponds to an axion mass between $1.9\,\mu$eV and $3.65\,\mu$eV [74]. Future plans for ADMX frequency limits go up to 10 GHz which corresponds to an axion mass of $m_a \approx 40\,\mu$eV. A schematical setup for a conventional haloscope experiment is seen in figure 2.4 on the left side. To achieve lower frequencies one tries to overcome the volume problem by using a magnetized area, where the axion photon conversion will happen at the magnetized surface. The theoretical

idea of the so called dish antenna used by the Broadband Radiometric Axion SearcheS (BRASS) [75] experiment, is to use the Maxwell-Axion equations

$$\nabla \vec{E} = \rho - g_{a\gamma} \vec{B} \nabla a \,, \qquad (2.3.6)$$

$$\nabla \times \vec{B} - \dot{\vec{E}} = \vec{J} + g_{a\gamma}(\vec{B}\dot{a} - \vec{E} \times \nabla a) \,, \qquad (2.3.7)$$

$$\nabla \vec{B} = 0 \,, \qquad (2.3.8)$$

$$\nabla \times \vec{E} + \dot{\vec{B}} = 0 \,, \qquad (2.3.9)$$

where a solution to these equations is

$$\vec{E}_a(t) = -g_{a\gamma} \vec{B}_e a(t) \,. \qquad (2.3.10)$$

That is the axion induced E_a field oscillates at the same frequency $\omega \sim m_a$ as the dark matter field. Due to the dielectric constant ϵ of the electric field in medium, the electric field would have a discontinuity at the boundary. To preserve continuity of the E_a field, photon-like waves are needed to match the boundary conditions and are emitted from the surface. These emitted photon are detectable and lead to the axion mass, where BRASS want to search in a frequency range of 2.4 GHz to 2.4 THz which is related to an axion mass from 20 μeV to 800 μeV. An improvement of this experimental design is MADMAX [76], which aims to have instead of one magnetized surface $N_d = 80$ disks lined up in a magnetic field, see figure 2.4 on the right side. The emitted waves can be enhanced by an factor of N_d^2 which leads to a potential frequency range of 10 GHz to 100 GHz and an axion mass range of 40 μeV to 400 μeV but with a higher sensitivity as the BRASS experiment could reach.

In figure 2.5 experimental constraints and planned experiments distinguished by dashed lines are shown. The lower bound to the axion coupling constant for the KSVZ axion can be given by $f_a > 4 \times 10^8$ GeV, where an upper bound is a bit harder to specify. We see that haloscope experiments (ADMX) have ruled out a specific region around 10^{12} GeV $< f_a < 10^{13}$ GeV for QCD-axion models but above that, the QCD-axion could still exist.
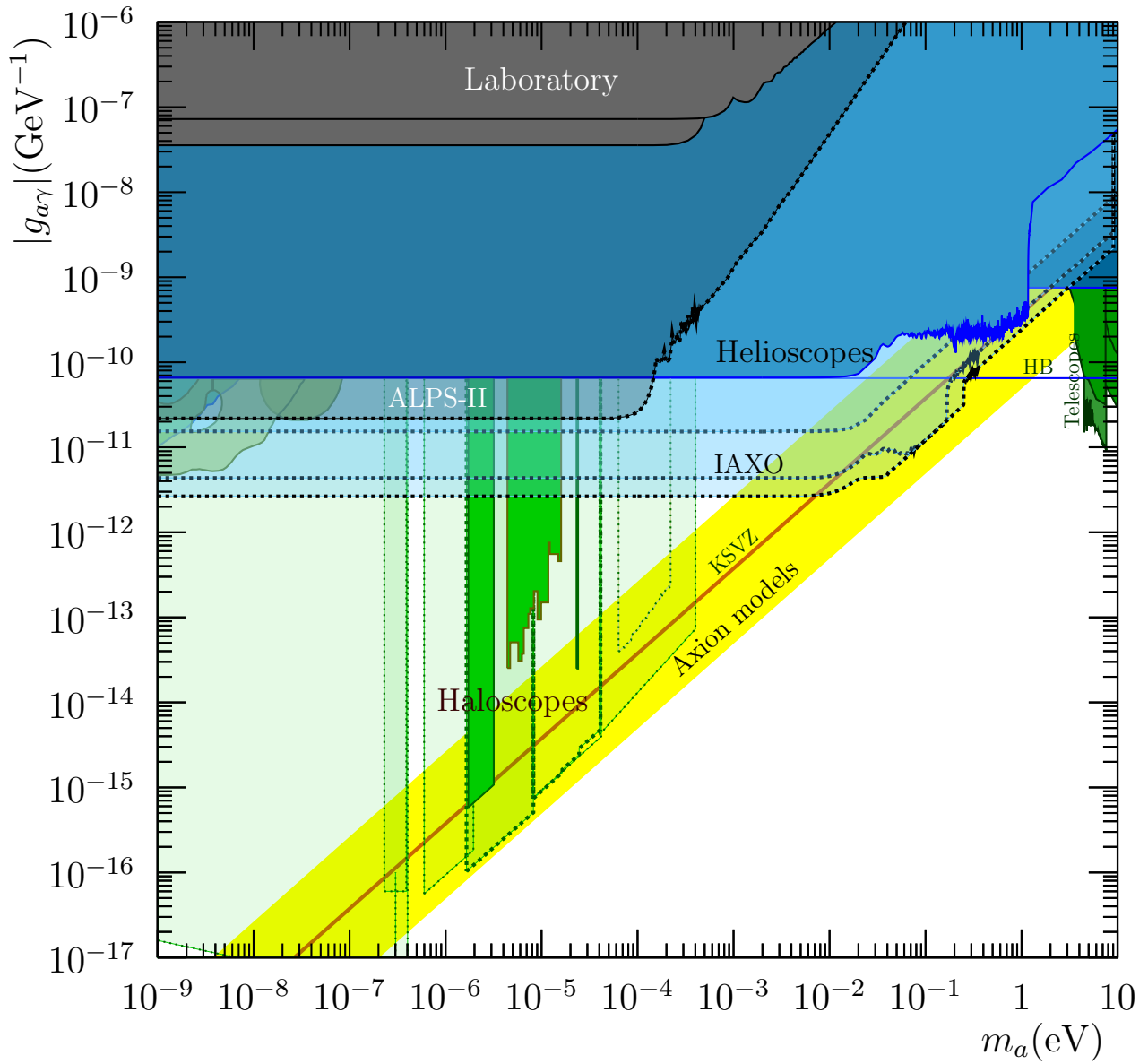
Figure 2.5.: Figure taken from [68]. Overall plot in the ($g_{a\gamma}$, m_a) plane. The laboratory, helioscope and haloscope areas are colored in black, blue and green respectively. The intended experiments are shown in semi-transparent colors.

Chapter 3

Axion Cosmology

In the previous chapter the axion Lagrangian was derived by the KSVZ model. In this chapter the different contributions of the axion Lagrangian are explained, where the different contributions of the potential are, due to the cosmological evolution, temperature dependent. The Friedman-Robertson-Walker (FRW) metric that follows the cosmological principle of the Universe is explained afterwards, which also includes the flat space solution [77–79]. The breaking of the PQ symmetry leads to topological defects, namely string and domain wall defects, which contributes to the axion production and are also explained in this chapter [4, 80]. Another important axion source is the misalignment mechanism and is also explained in this chapter [81]. The way the PQ symmetry gets broken has a huge impact to the production rate of axions. If one expect that the PQ symmetry is broken before or after the inflation of the Universe the different production mechanisms contribute differently. Finally the relation between dark matter and axions is explained. The corresponding numerical calculations are discussed in chapter 8.

3.1 Temperature Dependency

In the previous chapter we concluded with the axion Lagrangian, Eq. (2.2.22), which we want to discuss now in more detail. The Lagrangian can be split up into three parts

$$-\mathscr{L}_a = \mathscr{L}_{\text{kin}} + V_{\text{PQ}}(\phi) + V_{\text{anomaly}}(\phi), \tag{3.1.1}$$

$$\mathscr{L}_{\text{kin}} = (\partial_\mu \phi)^2, \tag{3.1.2}$$

$$V_{\text{PQ}}(\phi) = \frac{\lambda}{8} \left(2\phi\phi^* - f_a^2 \right)^2 + \frac{\lambda}{6} T^2 |\phi|^2, \tag{3.1.3}$$

$$V_{\text{anomaly}}(\phi) = \chi(T)(1 - \cos(N\theta)), \tag{3.1.4}$$

where again $\chi = \frac{m_a^2 f_a^2}{N^2}$ is the topological susceptibility, T is the temperature, and $\theta = \arg(\phi)$. We will now discuss the consequences of the potentials introduced to the axion Lagrangian. The contribution of each part in the potential term is highly dependent on temperature and therefore of the evolution of the Universe. The complex field is described by

$$\phi = \frac{f_a}{\sqrt{2}} e^{i\theta}. \tag{3.1.5}$$

(a) Unbroken   **(b)** Spontaneously broken   **(c)** Explicitly broken
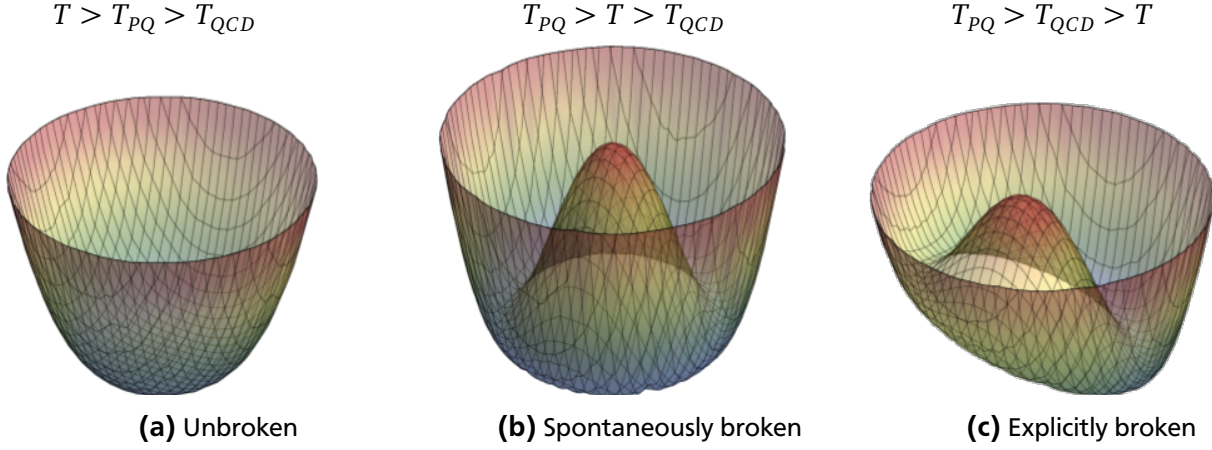
Figure 3.1.: Schematic illustrations of potentials. **(a)** is an unbroken potential which represents the behavior of the field before PQ symmetry is broken. **(b)** is the case where PQ symmetry is broken but the QCD anomaly doesn't contribute. In **(c)** both symmetries are broken.

Figure 3.1 shows the behavior of the potential for different temperature regions. If the temperature $T > T_{PQ} = \sqrt{3} f_a$ the PQ symmetry is restored, which is ensured by the second part of $V_{PQ}(\phi)$. This leads to a vacuum expectation value (VEV) of $\langle \phi \rangle = 0$. Below the temperature T_{PQ} the symmetry gets spontaneously broken and the VEV changes to $\langle \phi \rangle = \frac{f_a}{\sqrt{2}}$ for $T \ll T_{PQ}$. This is a set of values that minimizes the potential and is called the vacuum manifold. If the temperature drops below $T_{QCD} = \Lambda_{QCD}$ the anomaly part plays an additional role and breaks the PQ symmetry explicitly, which changes the VEV to $\langle \phi \rangle = \frac{f_a}{\sqrt{2}} e^{i\theta_0}$. Therefore the VEV changes from a set of vacua to a single vacuum value.

The effective Lagrangian for the case in which PQ symmetry is broken spontaneously but not explicitly reduces to

$$-\mathscr{L}_{\text{eff}} = (\partial_\mu \phi)^2 + \frac{\lambda}{8} \left(2\phi\phi^* - f_a^2 \right)^2 . \tag{3.1.6}$$

The term $\frac{\lambda}{6} T^2 |\phi|^2$ gets less important than $\frac{\lambda}{8} \left(2\phi\phi^* - f_a^2 \right)^2$ when the temperature drops below T_{PQ}, due to the quadratic order; it is therefore neglected in the effective Lagrangian. Since PQ symmetry is spontaneously broken we define

$$\phi(x) = \left(\frac{f_a}{\sqrt{2}} + \frac{\sigma(x)}{\sqrt{2}} \right) e^{i\theta(x)} . \tag{3.1.7}$$

The effective Lagrangian is then expressed as

$$-\mathscr{L}_{\text{eff}} = \frac{1}{2} (\partial \sigma)^2 + \left(\frac{f_a}{\sqrt{2}} + \frac{\sigma}{\sqrt{2}} \right)^2 (\partial \theta)^2 + \frac{1}{2} \lambda f_a^2 \sigma^2 - \frac{\lambda}{8} \left(f_a^2 \sigma^2 + f_a \sigma^3 + \sigma^4 \right), \tag{3.1.8}$$

where the massless Goldstone boson is θ and σ is the massive radial excitation with mass $m_\sigma = \sqrt{\lambda} f_a$. The massive particle σ is often called the saxion. If the temperature drops below T_{QCD}, the effective Lagrangian changes to

$$-\mathscr{L}_{\text{eff}} = (\partial_\mu \phi)^2 + \frac{\lambda}{8} \left(2\phi\phi^* - f_a^2 \right)^2 + \chi(T)(1 - \cos(N\theta)) . \tag{3.1.9}$$

There are different mechanisms which are important for the axion production which we will explain now.

3.2 Friedman-Robertson-Walker Metric and Hubble Parameter

The cosmological principle states that all positions and all spatial directions are equal [82]. This means that the universe is homogeneous and isotropic. The metric that satisfies the homogeneity and isotropy requirements is the Friedmann-Lemaître-Robertson-Walker metric (FRW). The metric can be expressed as

$$ds^2 = -dt^2 + a(t)^2 dx^2, \tag{3.2.1}$$

where $a(t)$ is an unknown scale factor and dx^2 ranges over a 3-dimensional space of uniform curvature and is expressed by

$$dx^2 = \frac{dr^2}{1 - kr^2} + r^2(d\theta^2 + \sin^2(\theta)d\phi^2). \tag{3.2.2}$$

In this equation k is the curvature factor of the universe, where for $k = 0$ the metric reduces to Cartesian coordinates. We can define the Hubble parameter in terms of the scale factor a with

$$H = \frac{\dot{a}(t)}{a(t)}. \tag{3.2.3}$$

using the Einstein equation one obtains two equations of motion

$$\dot{\rho}(t) = -3(\rho + P)\frac{\dot{a}(t)}{a(t)}, \tag{3.2.4}$$

$$\dot{a}(t)^2 = \frac{8\pi G}{3}\rho a^2, \tag{3.2.5}$$

where G is the gravitational constant $G = \frac{1}{m_{pl}^2}$, ρ is the energy density and P is the pressure. With Eq. (3.2.4) and Eq. (3.2.5) one obtains

$$H^2 = \frac{8\pi}{3m_{pl}^2}\rho, \tag{3.2.6}$$

$$\rho = a^{-3(1+w)}, \tag{3.2.7}$$

where $w = \frac{P}{\rho}$ is the equation of state parameter for cosmological scenario. For $w = 1$ it describes the kination era, for $w = \frac{1}{3}$ radiation , for $w = 0$ matter, for $w = -\frac{1}{3}$ describes curvature and $w = -1$ is for a cosmological constant. Inserting Eq. (3.2.3) and Eq. (3.2.7) in Eq. (3.2.6) we obtain

$$\frac{1}{a(t)}\frac{da(t)}{dt} = Ca^{-3(1+w)/2}, \tag{3.2.8}$$

where $C = \frac{8\pi}{3m_{pl}^2}$ is a constant. Solving Eq. (3.2.8) leads to

$$a(t)^{3(1+w)/2} = C't, \tag{3.2.9}$$

where $C' = \frac{2C}{3(1+w)}$. One can remove the constants by introducing a reference time $t = t_0$ where $a(t) = a(t_0)$ is

$$\frac{a(t)^{3(1+w)}}{a(t_0)^{3(1+w)}} = \left(\frac{t}{t_0}\right)^2 \rightarrow a(t) = a(t_0)\left(\frac{t}{t_0}\right)^{\frac{2}{3(1+w)}}. \tag{3.2.10}$$

By inserting Eq. (3.2.10) into the definition of the Hubble parameter Eq. (3.2.3) we will get

$$H = \frac{2}{p}t^{-1}, \tag{3.2.11}$$

where $p = 3(1+w)$ is a parametrization. Now let us introduce conformal time, defined as

$$d\tau = a(t)^{-1}dt. \tag{3.2.12}$$

The reason for this definition is seen by the FRW metric; with this definition we can rewrite the metric as

$$ds^2 = a(t)^2(-d\tau + dx_i dx_i). \tag{3.2.13}$$

We can calculate the relation of time to conformal time with

$$\tau = \frac{p}{p-2}a^{-1}t. \tag{3.2.14}$$

For the scaling parameter we get $a = \tau^{\frac{2}{p-2}}$. Since the metric includes the square of the scaling parameter it is useful to introduce a new parameter n which describes the relation of the time and the conformal time parameter. It can be expressed by

$$n = \frac{4}{p-2}. \tag{3.2.15}$$

The metric for example will then be

$$g_{\mu\nu} = \tau^n(-d\tau^2 + dx^2). \tag{3.2.16}$$

The relation for time and conformal time can be expressed by

$$\tau = \left(1 + \frac{n}{2}\right)a^{-1}t. \tag{3.2.17}$$

Finally we will show in a table the key values for the same expansion rates for the different parameters

Table 3.1.: Desciption of the parameters introduced above

	w	p	n
curved	$-\frac{1}{3}$	2	∞
matter	0	3	4
radiation	$\frac{1}{3}$	4	2
kination	1	6	1
flat	∞	∞	0
constant	-1	0	-2

3.3 Axion Production Mechanism

The introduced effective Lagrangian with temperature dependence provides two different main production mechanisms, which are the misalignment mechanism and topological defects [80, 81]. The topological defects split up into string defects and domain wall defects.

3.3.1 Topological Defects

Topological defects are regions where the field is forced to leave the vacuum manifold because of topology. In this thesis we will use and explain strings and domain walls, other topological defects such as monopoles are not relevant for this model, and are therefore not discussed.
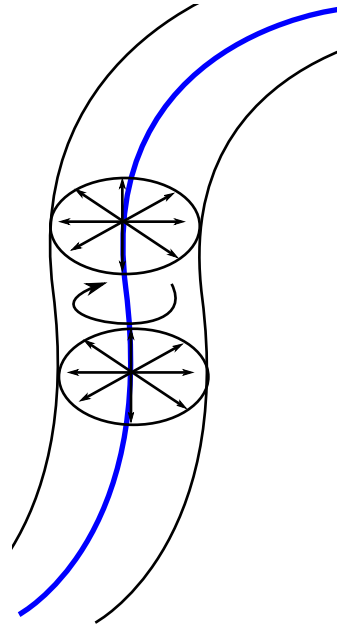
String Defects

Figure 3.2.: In blue the string defect, where the arrows pointing away from the string. The field has to wind by a factor of 2π around the fields.

String defects are one of the most important production mechanisms for axion cosmology. The potential can be described by

$$V_s = \frac{\lambda}{8}(2\phi^*\phi - f_a^2)^2 \,. \tag{3.3.1}$$

If the symmetry of the potential gets spontaneously broken after a phase transition, the VEV changes from $\langle\phi\rangle = 0$ to $\langle\phi\rangle = \frac{f_a}{\sqrt{2}}e^{i\theta}$. The parameter θ is the arbitrary phase. The set of values of ϕ which minimize the potential is called the vacuum manifold. It describes the amount of different vacua of the potential. If we have one value for $\langle|\phi|\rangle = \frac{f_a}{\sqrt{2}}$, it describes a circle in the complex plane. In other words θ can take values between $[0, 2\pi]$ at each point in space. An important fact is that the θ values will be uncorrelated and randomly chosen in causally disconnected regions of space. The total change of θ around a closed loop in space has to be equal to $2\pi n$. In this case $n \in \mathbb{Z}$ denotes the winding number, which counts how often the field ϕ winds around its vacuum manifold. Since $n \in \mathbb{Z}$ can take negative and positive values, this indicates the direction ϕ moves along the vacuum manifold. If we continuously shrink the loop, it will wind around the vacuum manifold. But it's not possible to change the winding number discontinuously to $n = 0$. For this reason the phase θ has at least one point at which it is undefined if $n \neq 0$. Therefore inside any loop for which $\Delta\theta = 2\pi n$, there must be $|n|$ tubes of false vacua inside (or more), which are called strings. Those connected tubes can have no ends and must be loops or infinite. See figure 3.2 for an illustration with winding number $n = 1$. If $|n| > 1$ it is possible to separate the loops such that each loop includes only one string.

Domain Walls

Domain walls occurs when a discrete symmetry is spontaneously broken. The term in $\mathscr{L}_a$ which leads to an explicit broken symmetry is:

$$V_e(\phi, \phi^*) = \frac{m_a^2 f_a^2}{N^2}\left(1 - \cos(N \arg(\phi))\right). \tag{3.3.2}$$

Thus, the spontaneously broken $Z(N)$ symmetry, which is a subgroup of $U(1)_{PQ}$, implies an N fold degeneracy of the vacuum. In other words, the degenerated vacua are at equidistant points on the circle at the bottom of the "Mexican hat" potential. Figure 3.3 shows an hybrid defect, where a wall is connected to a string, for the case that only one VEV exist. For changing $\theta = 0$ to $\theta = 2\pi$, there must be some 2D surface with $\theta \simeq \pi$. This is the domain wall defect, where the change of θ depends on the wall thickness $l \sim 1/m_a$. The change across the wall is 2π. The field values outside the wall take the VEV, where inside the wall the field changes continuously between these two values. If we distinguish between the different N, we have two cases to look at:

- **N=1**: If $N = 1$, there is just one minimum the field can take. It corresponds to the potential in figure 3.1c (where it is tilted). Because of this single minimum, the network of domain walls is unstable, since both sides of the domain walls are in the same vacuum.

- **N>1**: If $N > 1$, the field can take different vacuum expectation values, therefore the field is on either side of a domain wall and cannot be in the same vacuum. In this case domain walls can shrink under tension but can't annihilate pieces of each other. Thus domain wall networks would be stable till the present day, which is in conflict with observations. This phenomena is called the domain wall problem [83]. One possible solution for this problem is adding a small term to the Lagrangian that breaks the $Z(N)$ symmetry and reduces the different vacua to a single one.

We will focus on $N = 1$ which isn't in conflict with observations and it's not necessary to add any new term to the Lagrangian $\mathscr{L}_a$.

As we already discussed for strings, the field changes by 2π, such that a string can arise. If we look at a string-wall network, strings will arise by moving around the explicitly broken potential. Therefore, one domain wall forms at every string see figure 3.3. However, a domain wall does not need to be bounded on a string and can arise without any other defects and oscillates for many times. The energy can be

calculated in the same way as for the string. We can approximate $\sqrt{2}\phi = f_a e^{i\theta}$ in case of $m_s^2 \gg m_a^2$ and choose the θ-variation along the z-axis that yields

$$E = \int dx \int dy \int_{-\infty}^{\infty} dz \left(\frac{f_a^2}{2} (\partial_z \theta)^2 + f_a^2 m_a^2 (1 - \cos(\theta)) \right), \tag{3.3.3}$$

$$\sigma = \frac{E}{A} = f_a^2 \int_{-\infty}^{\infty} dz \left(\frac{1}{2} (\partial_z \theta)^2 + m_a^2 (1 - \cos(\theta)) \right). \tag{3.3.4}$$

To integrate eqn. Eq. (3.3.4) we change the integration value from dz to $d\theta$. We obtain after extremizing the expression in eqn. Eq. (3.3.4):

$$\sigma = f_a^2 \int_{-\infty}^{\infty} dz (\partial_z \theta)^2, \tag{3.3.5}$$

where we can use the relation $(\partial_z \theta)^2 = m_a 2(1 - \cos(\theta))$

$$\sigma = f_a^2 \int_{-\infty}^{\infty} dz \frac{d\theta}{dz} (\partial_z \theta) = m_a f_a^2 \int_0^{2\pi} d\theta_a (2 - 2\cos(\theta))^{\frac{1}{2}}. \tag{3.3.6}$$

For the surface tension of a wall we obtain $\sigma = 8 f_a^2 m_a$. The energy density in walls can be written as [4]

$$\rho_{wall}(t) \geq \frac{\sigma}{t}, \tag{3.3.7}$$

where t is the age of the universe and A parametrizes the average surface area of walls in a Hubble volume t^3.

3.3.2 Misalignment Mechanism

Before the axion mass is affected by the chiral anomaly of QCD, the axion field has a random VEV in the range from $\theta = 0$ to $\theta = 2\pi$. After the axion begins to start feeling its mass, the true minimum becomes $\theta = 0$ for which it begins to coherently oscillate about this minimum, as shown in figure 3.4. This homogeneous mode corresponds to the creation of zero momentum axions.
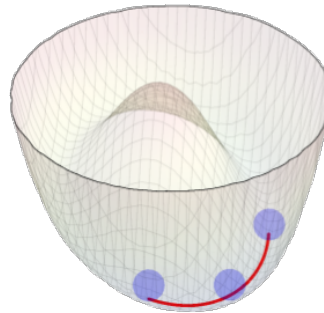

Figure 3.4.: The oscillation of the field is around its true minimum, which is symbolized by the red line.

It is convenient to assume that the universe is described by a flat Robertson-Walker-Friedman (FRW) metric

$$ds^2 = dt^2 - R(t)^2 d\vec{x}^2, \tag{3.3.8}$$
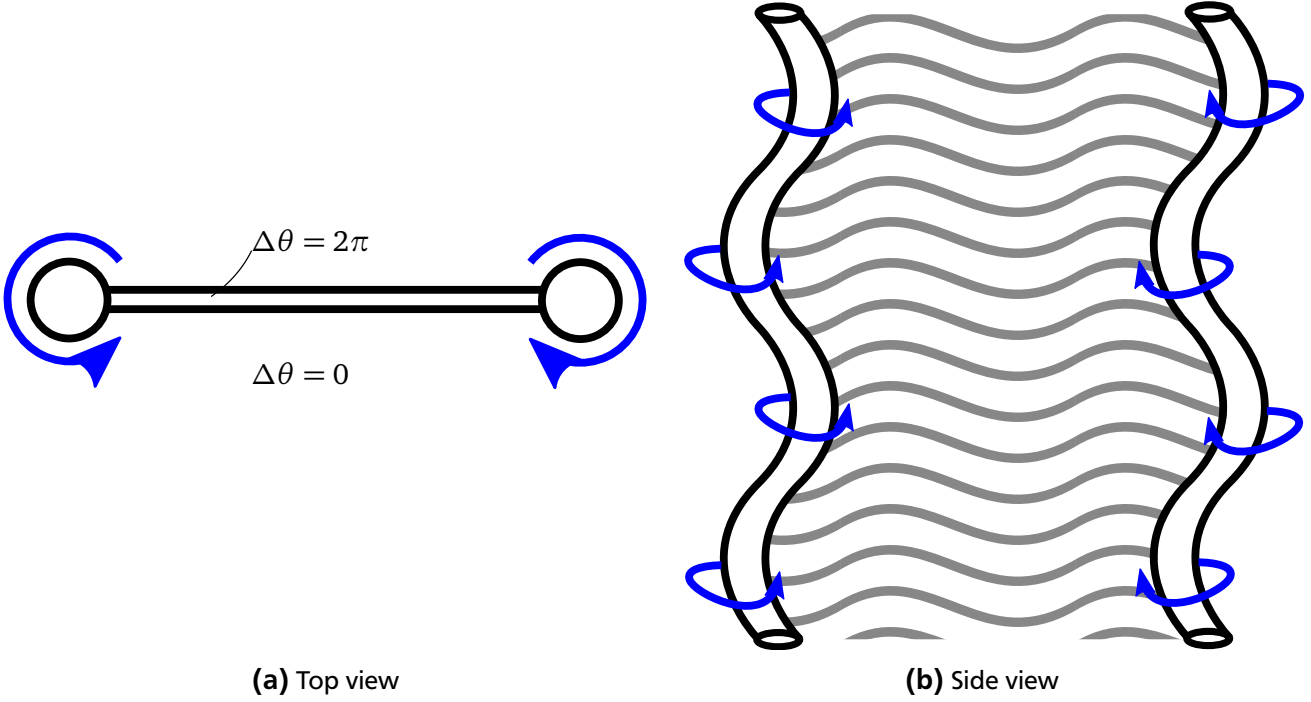
(a) Top view   **(b)** Side view

Figure 3.3.: In both figures a domain wall is connected to a string. If we go around the string, we need to leave the vaccum value, since one has to wind the potential. The change of the phase happens now inside the domain wall and not uniformly as before the symmetry gets explicitly broken.

where $R(t)$ describes the scale factor and the components of $\vec{x}$ are the co-moving spatial coordinates. The equation of motion for the axion field $a(x)$ can be expressed as

$$g^{\mu\nu}D_\nu\partial_\mu a(x) - \frac{\partial}{\partial a(x)}V_e[a(x)] = 0, \tag{3.3.9}$$

$$\left(\partial_t^2 + 3H\partial_t - \frac{1}{R^2}\nabla^2\right)a(x) + \frac{m_a^2(t)f_a}{N}\sin\left(\frac{Na(x)}{f_a}\right) = 0, \tag{3.3.10}$$

where D_μ is the covariant derivative, $g^{\mu\nu}$ the FRW metric tensor, V_e is the explicitly symmetry breaking term and $H = \frac{\dot{R}}{R} = c^2 R^{-k}$ is the Hubble constant. The parameter k describes the dominated era of the universe:

$$
\begin{aligned}
k_{kin} &= 6 & \rightarrow & & H &= \frac{1}{3t} & & \text{kinetic} \\
k_{rad} &= 4 & \rightarrow & & H &= \frac{1}{2t} & & \text{radiation} \\
k_{mat} &= 3 & \rightarrow & & H &= \frac{2}{3t} & & \text{matter}
\end{aligned}
\tag{3.3.11}
$$

The axion field only depends on time, if the field can be taken to be regionally homogeneous, the field would take the form $a(x) = a(t)$. This is already the case, if symmetry is broken before inflation, and topological defects are inflated away. For the case that symmetry breaks after inflation, the axion field

takes random values in space after inflation. To handle it as regionally uniform we have to average over these values, therefore Eq. (3.3.10) reduces to

$$\left(\frac{d^2}{dt^2} + \frac{3}{2t}\frac{d}{dt}\right)a(t) + \frac{m_a^2(t)f_a}{N}\sin\left(\frac{Na(t)}{f_a}\right).$$

(3.3.12)

An illustrating plot for the misalignment mechanism is given in figure 3.5 which is taken out of [81]. The mechanism can be separated in three different phases.

- $t \ll t_1$: Since $H \gg m_a$, the axion mass m_a is negligible. Solving the second order differential equation leads to a constant solution for the axion field.

- $t \approx t_1$: In this case the axion mass becomes comparable to $3H \approx m_a$. Therefore the explicit breaking part is no longer negligible. The initial value which the axion field takes by breaking spontaneously the symmetry is called the misalignment angle.

- $t > t_1$: This part is characterized by the continued oscillation of the axion field which looks like pressureless matter. In this case the axion number of zero momentum axions per co-moving volume is an adiabatic constant.

The critical time t_1 describes the point where the axion begins to feel its mass. In other words t_1 is the point where $U(1)_A$ gets explicitly broken. It turns out that light axions contribute more to the energy balance than heavy axions do, due to the energy red-shift with time [81].
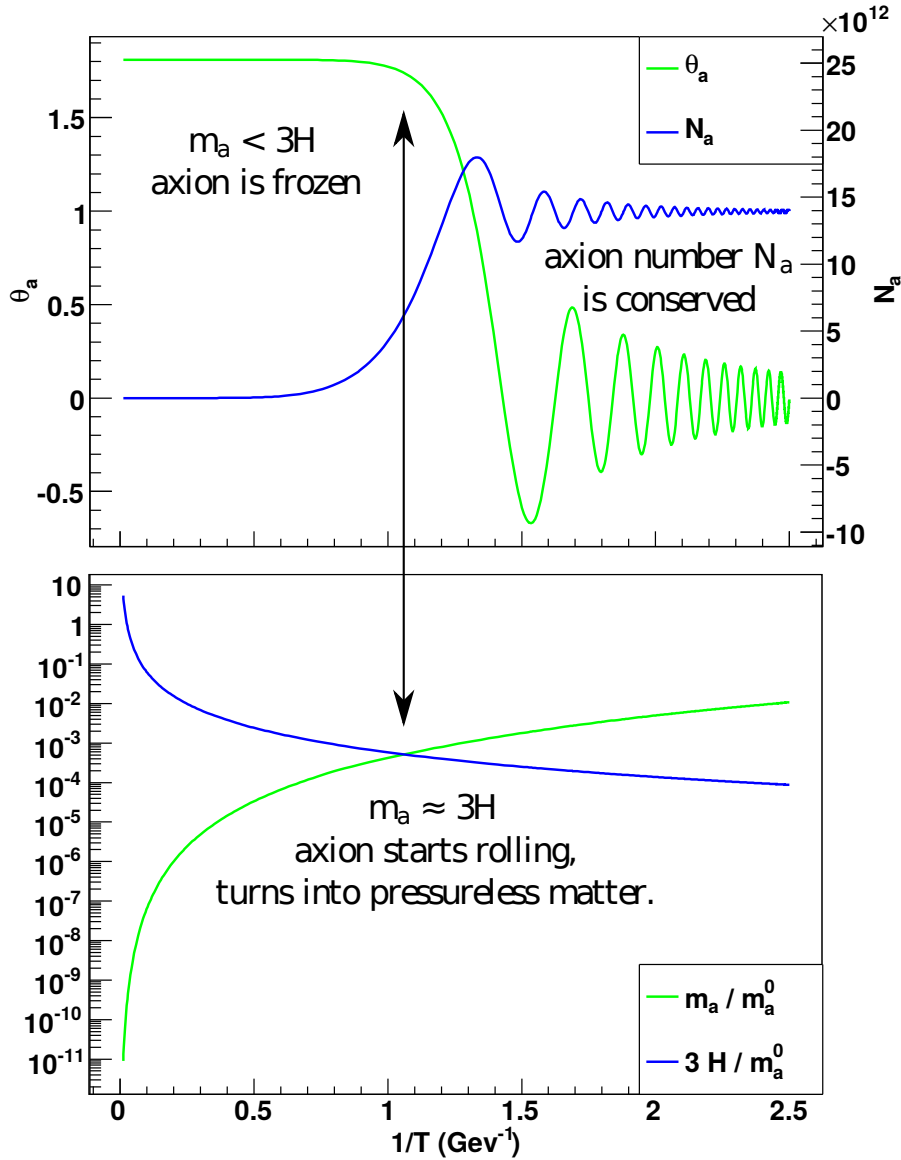
Figure 3.5.: This figure is taken from [81] and describes three different stages. At the beginning the axion zero mode is frozen; this corresponds to the late-time solution of Eq. (3.3.12) with m_a neglected. The second stage when the axion starts to feel its mass if $m_a \approx 3H$, and evolves to its minimum at $\theta_a = 0$ (θ_a is equivalent to $a(t)$ in Eq. (3.3.12)). After a few oscillations the axion number per comoving volume stays constant as long as the axion mass and the scale factor change slowly. This can be used to extrapolate the result to today.

3.4 Inflation

The way the axion production mechanism can contribute to the mass of the axion, strongly depends on the time when PQ symmetry gets broken. Inflation may have an important role to the axion mass, because during inflation the Universe reheated which can lead to two different scenarios for the axion cosmology.

- $T_{PQ} > T_{reheat}$:
  PQ symmetry gets broken before or during inflation and won't get restored during reheating. The axion field would be homogenized over large distances. The disconnected regions of space-time, where $\theta \in [0, 2\pi]$, stretch to cosmic scale during inflation. Therefore, after inflation the universe

has a uniform initial $\theta_0 \in [0, 2\pi]$. This means any topological defects will be inflated away. Only the misalignment mechanism will contribute to this scenario.

- $T_{PQ} \leq T_{reheat}$:
  PQ symmetry gets broken after inflation, the disconnected regions will not be inflated away. This leads to uncorrelated axion fields on scales larger then the horizon. During this process, complicated dynamical phenomena, such as domain walls and strings form.

For the further discussion, we only focus on the more complex case with $T_{PQ} \leq T_{reheat}$.

3.5 Axion and Dark Matter

To calculate the relation between axions and dark matter, we have to make some assumptions. First we suppose that all dark matter consists of axions. Where the modern dark matter density to entropy ratio can be calculated by using the Planck results [2]

$$\frac{\rho_{\mathrm{dm}}}{s} \simeq 0.39 \times 10^{-9}\,\mathrm{GeV}. \tag{3.5.1}$$

$$\tag{3.5.2}$$

Secondly, we assume that the FRW metric describes the cosmological epoch where axions are produced. That is, we expect that after axions got produced, the number density per unit coordinate volume remains constant which is

$$n_a a(t)^3 = \mathrm{const}, \tag{3.5.3}$$

where n_a is the axion number defined by

$$n_a(T) = \frac{\rho(T)}{m_a(T)}. \tag{3.5.4}$$

Note that this expected adiabatic behavior appears after a time t_* which is around the time where the symmetry gets explicitly broken. The energy density for bosons is given by

$$\rho(T) = \frac{\pi^2}{30} g_* T^4 = \rho_{\mathrm{const}} T^4, \tag{3.5.5}$$

where the effective number of light degrees of freedom is $g_*(1\,\mathrm{GeV}) \simeq 73$ [45]. At this time we have

$$m_a(T_*)^2 = H(T_*)^2, \tag{3.5.6}$$

where after that it ensures adiabatic evolution for the axion field which is

$$\frac{dm_a}{dt} \ll m_a^2. \tag{3.5.7}$$

The Hubble parameter derived in the previous section is

$$H(T)^2 = \frac{8\pi}{3m_{\mathrm{P}}^2} \rho(T) = H_{\mathrm{const}} T^4, \tag{3.5.8}$$

and the plank mass is $m_P \simeq 1.22 \cdot 10^{19}$ GeV. For the axion mass we can write

$$m_a(T)^2 = \frac{\chi(T)}{f_a^2} = \chi_{\text{const}} \frac{T^{-n}}{f_a^2}, \tag{3.5.9}$$

where the topological susceptibility for high temperature is given by [84]

$$\chi(T) = \left(\frac{1\,\text{GeV}}{T}\right)^n \left(1.02(35) \times 10^{-11}\,\text{GeV}^4\right), \tag{3.5.10}$$

and the dilute instanton model dependent factor $n \approx 7.66$ [57]. By using Eq. (3.5.6) and inserting Eq. (3.5.8) and Eq. (3.5.9) we obtain for the temperature

$$T_* = \left(\frac{\chi_{\text{const}}}{H_{\text{const}}^2} \frac{1}{f_a^2}\right)^{\frac{1}{4+n}}. \tag{3.5.11}$$

The ratio of axion number-density to entropy density is approximately the same at the end of axion production as it is today. The relation can therefore be expressed as

$$\frac{\rho_a(T_0)}{m_a(T_0)s(T_0)} = \frac{\rho_a(T_*)}{m_a(T_*)s(T_*)}, \tag{3.5.12}$$

where $T_0 \simeq 0$ GeV and the entropy density

$$s(T) = \frac{2\pi^2}{45} g_* T^3 = s_{\text{const}} T^3. \tag{3.5.13}$$

Using Eq. (3.5.5) it reduces to

$$\frac{\rho_a(T_0)}{s(T_0)} = \frac{m_a(T_0)n_a(T_*)}{s(T_*)}, \tag{3.5.14}$$

with $m_a(T_0) = \sqrt{\frac{\chi(T_0)}{f_a^2}}$ and $\chi(T_0) = (0.074\text{GeV})^4$. Taking our first assumption, that is $\frac{\rho_a(T_0)}{s(T_0)} = \frac{\rho_{\text{dm}}}{s}$, the only undetermined function is $n_a(T_*)$ which is for the modern Universe

$$n_a(T_*) \simeq KH(T_*)f_a^2. \tag{3.5.15}$$

The factor K is a constant, which determines the produced density of axions and is achieved after one expects adiabatic evolution for the fields in our lattice simulation [25]

$$K = \frac{\tau^2}{\tau_*} \int \frac{d^3k}{(2\pi)^2} \left(\frac{\sqrt{k^2 + m_a^2}}{2} \langle \theta^2(k)\rangle + \frac{1}{2\sqrt{k^2 + m_a^2}} \langle (\partial_t \theta(k))^2\rangle\right), \tag{3.5.16}$$

with τ_* the time, when the axion mass gets physically significant. To calculate the axion decay constant we use Eq. (3.5.15) and insert the previous evaluated temperature T_*, which yields

$$f_a = \left(\frac{KH_{\text{const}}\chi(T_0)}{s_{\text{const}}\left(\frac{\rho_{\text{dm}}}{s}\right)}\right)^{\frac{4+n}{6+n}} \left(\frac{\chi_{\text{const}}}{H_{\text{const}}^2}\right)^{\frac{1}{6+n}}. \tag{3.5.17}$$

Calculating the factor K leads therefore to f_a and to the axion mass m_a.

Chapter 4

Effective String Action

In this and in the next chapter we will explain in more detail about string actions. In this chapter we explain the effective action of the global and local field theories, which is also important for the construction of the two-Higgs model which we will also explain in the next chapter. We will start in this chapter with explaining the Nambu-Goto action, which is the effective theory of local $U(1)$ strings and the Kalb-Ramond action, which is the effective action of global $U(1)$ strings. The Nambu-Goto action will also play an important role in chapter 9, there we present a method to construct an initial string by using the loop solution of the Nambu-Goto action, which is described in chapter 6, and apply it to lattice simulation.

4.1 Nambu Goto Action

Our goal in this section is to derive the effective string action for local strings, for this we will introduce first the Nambu-Goto action and show afterwards that the Lorentz-contracted local string action is the Nambu-Goto action in first order approximation. The Nambu-Goto action is the easiest form to build a string action. Starting by the area functional for spacetime surfaces described by [85]

$$A = \int d\tau \int d\sigma \sqrt{\left(\frac{\partial X^\mu}{\partial \tau}\frac{\partial X_\mu}{\partial \sigma}\right)^2 - \left(\frac{\partial X}{\partial \tau}\right)^2\left(\frac{\partial X}{\partial \sigma}\right)^2}, \tag{4.1.1}$$

where X^μ is the string coordinates which describes the surface by mapping spactime coordinates. The action can be build by multiplying the string tension μ to the area functional

$$S = -\mu \int d\tau \int d\sigma \sqrt{(\dot{X}X')^2 - \dot{X}^2 X'^2}, \tag{4.1.2}$$

with $\dot{X} \equiv \frac{\partial X^\mu}{\partial \tau}$ and $X' \equiv \frac{\partial X^\mu}{\partial \sigma}$. The Nambu-Goto action can be written in a manifestly reparametrization invariant way, starting with

$$-ds^2 = dX^\mu dX_\mu = \frac{\partial X^\mu}{\partial \xi^\alpha}\frac{\partial X_\mu}{\partial \xi^\beta} d\xi^\alpha d\xi^\beta, \tag{4.1.3}$$

where the indices α and β are running from 1 to 2 and the parameters are $\xi^1 = \tau$ and $\xi^2 = \sigma$. Defining an induced metric with

$$\gamma_{\alpha\beta} = \frac{\partial X^\mu}{\partial \xi^\alpha}\frac{\partial X_\mu}{\partial \xi^\beta} = \begin{bmatrix} \dot{x}^2 & \dot{x}x' \\ \dot{x}x' & x'^2 \end{bmatrix}, \tag{4.1.4}$$

will lead to the known form of the Nambu-Goto action

$$S = -\mu \int d\tau d\sigma \sqrt{-\gamma}, \tag{4.1.5}$$

where $\gamma = \det(\gamma_{\alpha\beta})$. The equations of motion for the Nambu-Goto action is

$$\nabla^2 x^\mu + \Gamma^\mu_{\nu\rho} \gamma^{ab} \partial_a x^\nu \partial_b x^\rho = 0 \,, \tag{4.1.6}$$

where

$$\Gamma^\mu_{\nu\rho} = \frac{1}{2} g^{\mu\lambda} \left(\partial_\rho g_{\lambda\nu} + \partial_\nu g_{\lambda\rho} - \partial_\lambda g_{\nu\rho} \right) \,, \tag{4.1.7}$$

is the four-dimensional Christoffel symbol. The covariant Laplacian is given by

$$\nabla^2 x^\mu = \frac{1}{\sqrt{-\gamma}} \partial_a \left(\sqrt{-\gamma} \gamma^{ab} \partial_b x^\mu \right) \,. \tag{4.1.8}$$

To see now, that the Nambu-Goto action describes the local action with thin strings and large curvature radius, we consider the spacetime point nearer the worldsheet than its curvature radius with

$$x^\mu = X^\mu(\tau, \sigma) + \rho^A n^\mu_A(\tau, \sigma), \tag{4.1.9}$$

where $n^\mu_A (A = 1, 2)$ are the two orthonormal vectors perpendicular to the worldsheet and ρ^A are the coordinates in these directions, where $X^\mu(\tau, \sigma)$ describes the worldsheet. The action for the local string is

$$S = \int d^4x \mathcal{L}, \tag{4.1.10}$$

$$\mathcal{L} = -\left(|D_\mu \phi|^2 + \frac{F_{\mu\nu} F^{\mu\nu}}{4} + V(\phi) \right), \tag{4.1.11}$$

where we introduce the curved coordinate system $\xi^\mu = (\tau, \sigma, \rho)$ and will integrate over ρ. The action then reads

$$S = \int d\tau d\sigma d^2\rho \sqrt{-\det M_{\alpha\beta}} \mathcal{L} \,, \tag{4.1.12}$$

where one obtain by calculating the Jacobian the change from x^μ to ξ^μ [86]

$$\sqrt{-g} \det \left(\frac{\partial x}{\partial \xi} \right) = \sqrt{-\det M_{\alpha\beta}} \,, \tag{4.1.13}$$

$$\sqrt{-\det M_{\alpha\beta}} = \sqrt{-\gamma} \left(1 + \mathcal{O} \left(\frac{\delta}{R} \right) \right) \,. \tag{4.1.14}$$

Where δ is the string width and R the curvature radius. This finally reads for the action

$$S = -\mu \int d\tau d\sigma \sqrt{-\gamma} \left(1 + \mathcal{O} \left(\frac{\delta}{R} \right) \right) \,, \tag{4.1.15}$$

$$\mu = -\int d^2\rho \mathcal{L} \,. \tag{4.1.16}$$

Therefore at lowest order the effective action is the Nambu-Goto action.

4.2 Kalb Ramond Action

The analytic description of the global U(1)-string is more difficult due to its topological coupling to the Goldstone boson field. That is, we need a description that includes the change of the phase θ by 2π if a string is present.

An effective description for the U(1)-string where the action is given by

$$S = \int d^4 x (\partial_\mu \phi)^2 + |\phi|^2 (\partial_\mu \theta)^2 - V(\phi), \tag{4.2.1}$$

is the Kalb-Ramond action [87, 88]. To see this, we start with the equivalence of a real massless scalar field and a two index antisymmetric tensor $B^{\mu\nu}$, which is

$$\eta \partial_\mu \theta = \frac{1}{2} \epsilon_{\mu\nu\lambda\rho} \partial^\nu B^{\lambda\rho}, \tag{4.2.2}$$

where the equation of motion for θ is $\partial_\mu \partial^\nu \theta = 0$. A similar identity is

$$\epsilon^{\mu\nu\lambda\rho} \partial_\lambda \partial_\rho \theta = 0, \tag{4.2.3}$$

and requires the constraint

$$\partial_\mu (\partial^\mu B^{\nu\lambda} + \partial^\lambda B^{\mu\nu} + \partial^\nu B^{\lambda\mu}) = 0. \tag{4.2.4}$$

The field variable $B^{\mu\nu}$ can be expressed as a dependency of the field strength tensor

$$H^{\mu\nu\lambda} = \partial^\mu B^{\nu\lambda} + \partial^\lambda B^{\mu\nu} + \partial^\nu B^{\lambda\mu}, \tag{4.2.5}$$

where the action is given by

$$S_H = \frac{1}{6} \int H^2 d^4 x. \tag{4.2.6}$$

This is only valid for an action without a potential and therefore without string solutions. For the presence of strings the field equation for $H^{\mu\nu\lambda}$ is

$$\partial_\lambda \left(\frac{\eta}{|\phi|^2} H^{\mu\nu\lambda} \right) = \epsilon^{\mu\nu\lambda\rho} \partial_\lambda \partial_\rho \theta = 4\pi j^{\mu\nu}, \tag{4.2.7}$$

where the current $j^{\mu\nu} \neq 0$ in the string core. More generally, the commutators $[\partial_\mu, \partial_\nu] \neq 0$ in the presence of a string, and can be seen as a projection onto the worldsheet. The additional factor to the action reads

$$4\pi \int B_{\mu\nu} j^{\mu\nu} d^4 x = 2\pi \eta \int B_{\mu\nu} d\sigma^{\mu\nu}, \tag{4.2.8}$$

where

$$j^{\mu\nu} = \frac{\eta}{2} \int \delta^4 [x - x(\xi^a)] d\sigma^{\mu\nu}. \tag{4.2.9}$$

The factor ξ^a describes the wordsheet parametrization with $\xi^0 = \tau$ and $\xi^1 = \sigma$. The effective action with a description of a spontaneous symmetry breaking potential and therefore with the presence of strings yields the form

$$S = \underbrace{-\mu \int \sqrt{-\gamma} d\tau d\sigma}_{\mathscr{L}_{\text{NG}}} + \underbrace{\frac{1}{6} \int d^4 x H^2}_{\mathscr{L}_{\text{GS}}} + \underbrace{2\pi\eta \int B_{\mu\nu} d\sigma^{\mu\nu}}_{\mathscr{L}_{\text{KR}}}, \qquad (4.2.10)$$

and is the Kalb-Ramond action. The first part $\mathscr{L}_{\text{NG}}$ is the Nambu-Goto action introduced in the previous section, where the string tension appears by integrating over the massive $|\phi|$ modes. The second $\mathscr{L}_{\text{GS}}$ term compensates the singularity which appears at the string core, where $|\phi| = 0$ and also contains the dynamics far away from the string core. The last term $\mathscr{L}_{\text{KR}}$ represents the interaction of the string with the antisymmetric field $B_{\mu\nu}$, that is the string forces the Goldstone field θ to wind by 2π. Accordingly, including the second and the third term leads to an interaction between the field and the Nambu-Goldstone boson. The description of the string interaction with Goldstone bosons has a similarity to the interaction of a pointlike electron in electromagnetism.

Chapter 5

String Field Theory

In this chapter at first global $U(1)$ strings are explained, which are similar to the axionic strings introduced in chapter 3.[1] After discussing global strings, local strings are explained, which do not have long range string interactions. Because of that it is easier to simulate local string dynamics than global. However, to simulate correct axion physics, we need to simulate correct string tension κ, which is not possible with the axion Lagrangian gained from chapter 3. Therefore, we present in the last section of this chapter our novel two-Higgs method. This theory consists of two scalar and a gauge field, allows the study of the evolution from global to local string tension. With this new approach it is possible to calculate the correct string tension at any cosmic domain, after PQ symmetry is broken and therefore to an estimate for the axion mass.

5.1 Global U(1) Strings

Global strings arise by breaking a global U(1) symmetry. The easiest theory containing string solutions is that of a complex scalar field. The Lagrangian can be described by

$$-\mathcal{L} = \partial_\mu \phi^* \partial^\mu \phi + V(\phi), \tag{5.1.1}$$

$$V(\phi) = \frac{\lambda}{2}\left(\phi\phi^* - \frac{1}{2}f_a^2\right)^2, \tag{5.1.2}$$

and the equation of motion is

$$\partial_\mu \partial^\mu \phi - \lambda\phi\left(\phi\phi^* - \frac{1}{2}f_a^2\right) = 0. \tag{5.1.3}$$

With this expression we can start to derive the energy with:

$$T^{\mu\nu} = \frac{\partial\mathcal{L}}{\partial(\partial_\mu\phi)}\partial^\nu\phi - \mathcal{L}g^{\mu\nu}, \tag{5.1.4}$$

$$E = \int T^{00}d^3x. \tag{5.1.5}$$

Using Eq. (5.1.1) leads to

$$T^{00} = |\nabla\phi|^2 + \dot{\phi}^2 + \frac{\lambda}{8}(2|\phi|^2 - f_a^2)^2. \tag{5.1.6}$$

---

[1]   In this chapter we use the $[-+++]$ metric convention

If we assume that a string is lying along the z-axis, the field in cylindrical coordinates will read

$$\phi = \frac{f_a f(r)}{\sqrt{2}} e^{i\theta} . \tag{5.1.7}$$

The function $f(r)$ has the boundary conditions $f(r \gg \frac{1}{m_s}) \to 1$ and $f(r \to 0) \to 0$, where $m_s^2 = \lambda f_a^2$ is the saxion mass which arise out of the radial excitation of the potential minimum. The energy can be expressed as

$$E = \frac{1}{2} \int dz \int r \, dr \int d\phi \left[(f_a \partial_r f)^2 + |\frac{f f_a}{r} \partial_\phi e^{i\theta}|^2 + \frac{\lambda f_a^4}{4} (1 - f^2)^2 \right], \tag{5.1.8}$$

where the integral and the derivative are expressed in cylindrical coordinates. Evaluating the energy far away from the string core $\delta = \frac{1}{m_s}$, the expression Eq. (5.1.8) reduces to

$$E \approx \int_0^L dz \int_{r > \delta}^l r \, dr \int_0^\pi d\phi \frac{f_a^2}{r^2}, \tag{5.1.9}$$

$$E \approx f_a^2 L \pi \ln\left(\frac{l}{\delta}\right), \tag{5.1.10}$$

where l is an infrared cutoff which is taken to be the distance to the next string $l \propto \frac{1}{H}$. The expression $\mu = \frac{E}{L}$ is called string tension and is energy per unit length. Using the Euler-Lagrange equation and definition Eq. (5.1.7) we get [24]

$$f'' + \frac{f'}{r} - \frac{f}{r^2} - \frac{m_s^2}{2} f(1 - f^2) = 0, \tag{5.1.11}$$

with the condition $f(0) = 0$ and $f(r \to \infty) \to 1$ one obtains near 0

$$f(r) = c m_s r - \frac{c}{16}(m_s r)^3 + \frac{c + 16c^3}{768}(m_s r)^5 + ..., \tag{5.1.12}$$

where $c \approx 0.41$ is a constant. To calculate the velocity, we consider a string, which is stretched along the z axis and moving in the x direction. If the string is at rest, the field is

$$\phi(x, y, z) = e^{-i\phi_0} f_a \frac{x + iy}{r} f(r). \tag{5.1.13}$$

Inserting Eq. (5.1.12) in Eq. (5.1.13) one obtains near the string core with $r = \sqrt{x^2 + y^2}$

$$\phi(x, y) = e^{-i\phi_0} f_a c m_s (x + iy) \left(1 - m_s^2 \frac{x^2 + y^2}{16} + ...\right). \tag{5.1.14}$$

For a moving string at $t = 0$, with Lorentz transformation $x = \gamma x$, and $\partial_t \phi = -v \partial_x \phi$ one finds

$$-e^{-i\phi_0} \partial_t \phi(x, y; v) = f_a c m_s \gamma v . \tag{5.1.15}$$

Calculating $|\partial_t\phi|^2$ the velocity can expressed as

$$v^2 = \frac{\partial_t\phi^*\partial_t\phi}{f_a^2 m_s^2 c^2 + \partial_t\phi^*\partial_t\phi}, \tag{5.1.16}$$

where we inserted $\gamma = \frac{1}{\sqrt{1-v^2}}$.

5.2 Local U(1) Strings

Local strings arise in a spontaneously broken U(1) gauge theory, which is cylindrically symmetric. This requires a vector field A_μ, where then the Lagrangian can be written as

$$-\mathcal{L} = \frac{F_{\mu\nu}F^{\mu\nu}}{4} + |D_\mu\phi|^2 + V(\phi), \tag{5.2.1}$$

$$V(\phi) = \frac{\lambda}{2}\left(\phi\phi^* - \frac{1}{2}\eta^2\right)^2, \tag{5.2.2}$$

where $D_\mu = \partial_\mu + ieA_\mu$ and $F_{\mu\nu} = \partial_\mu A_\nu - \partial_\nu A_\mu$ with e the electric charge of the ϕ field. In the local case there is the Higgs particle with mass $m_H = \sqrt{\lambda}\eta$ and the Nambu-Goldstone boson which gains a mass by interacting with the vector field $m_A = e\eta$. For the mass ratio one can define

$$\beta = \frac{m_A^2}{m_H^2}, \tag{5.2.3}$$

where β describes the attraction of the string core, if $\beta < 1$ the string configuration is called Type-I strings. In this case where for $\beta > 1$ it is called Type-II strings. In case for $\beta = 1$, which is the case we will focus, it is called the Bogomol'nyi limit [89]. It is possible to calculate the velocity by using the field equations, but the coupled ordinary differential equations do not have analytical solutions. Therefore one has to calculate numerically the solution for every specific m_A and m_H. The equation of motion is:

$$D_\mu D^\mu\phi - \lambda\phi\left(\phi\phi^* - \frac{1}{2}\eta^2\right) = 0, \tag{5.2.4}$$

$$\partial_\mu F^{\mu\nu} + ie(\phi^*D^\mu\phi - D_\mu\phi\phi^*) = 0. \tag{5.2.5}$$

The solution for a stationary string along the z axis with $\xi = m_H r$ has

$$\phi_\rho = \frac{e^{i\varphi}f(\xi)}{\sqrt{2}}, \tag{5.2.6}$$

$$A_\varphi = \frac{g(\xi)}{\xi}, \tag{5.2.7}$$

for which the equation of motion become

$$g'' - \frac{g'}{\xi} = \frac{m_A^2}{m_H^2}f^2(g-1), \tag{5.2.8}$$

$$f'' - \frac{f'}{\xi} = \frac{f}{\xi^2}(1-g)^2 + \frac{1}{2}f(f^2-1). \tag{5.2.9}$$

The asymptotic behavior for the functions $f(m_H r)$ and $g(m_H r)$ are for small r

$$f(\xi) = f_1 \xi + \mathcal{O}(\xi^3), \tag{5.2.10}$$

$$g(\xi) = g_2 \xi^2 + \mathcal{O}(\xi^4), \tag{5.2.11}$$

where f_1 and g_2 are constants which can obtained numerically. The magnetic flux enclosed by the string is [90]

$$\Phi = \int \boldsymbol{B} d\boldsymbol{S} = \oint \boldsymbol{A} d\boldsymbol{l} = \int_0^{2\pi} \xi A_\varphi(\xi) d\varphi = 2\pi g(\xi), \tag{5.2.12}$$

where the flux is going to zero outside the string core ensured by $\lim_{\xi \to \infty} g(\xi) = 1$. The difference for local and global strings can be seen in its energy density. For local strings the energy density is much more localized so the energy density vanishes outside the core. The energy of the local string can be expressed by

$$E = \int d^3 x \left(|D_\mu \phi|^2 + \frac{1}{2}(E^2 + B^2) + V(\phi) \right), \tag{5.2.13}$$

where E and B are the electric and magnetic fields. The energy of a local string per unit length is given by

$$\mu = \pi \eta^2 \delta \left(\frac{m_A}{m_H} \right), \tag{5.2.14}$$

where $\delta \left(\frac{m_A}{m_H} \right)$ is a dimensionless function which increase monotonically [91].

5.3 Two-Higgs Strings

In this section we present the developed model we have published in [92].
We are interested in the large-scale structure of string networks and the infrared behavior of any (pseudo)Goldstone modes they radiate. For these purposes it is not necessary to keep track of all physics down to the scale of the string core. Rather, it is sufficient to describe the desired IR behavior with an *effective theory* of the strings and the Goldstone modes around them. This consists of removing the physics very close to the string core with an equivalent set of physics. It has long been known how to do this [29]. The string cores are described by the Nambu-Goto action [93–95], which describes the physics generated by the string tension arising close to the string core. The physics of the Goldstone mode is described by a Lagrangian containing the scalar field's phase. And they are coupled by the Kalb-Ramond action as introduced in chapter 4:

$$\mathscr{L} = \mathscr{L}_{\text{NG}} + \mathscr{L}_{\text{GS}} + \mathscr{L}_{\text{KR}}. \tag{5.3.1}$$

Compared to axionic strings $\mathscr{L}_{\text{NG}}$ tracks the effects of the string tension, which we name $\kappa \pi f_a^2$, stored locally along its length. Next, $\mathscr{L}_{\text{GS}}$ says that the axion angle propagates under a free wave equation, as expected for a Goldstone boson, and its decay constant is f_a. And $\mathscr{L}_{\text{KR}}$ incorporates the interaction between strings and axions, also controlled by f_a. The interaction can be summarized by saying that the string forces θ_a to wind by 2π in going around the string (in the same sense that the $e J_\mu A^\mu$ interaction in electrodynamics can be summarized by saying that it enforces that the electric flux emerging from a charge is e).

It should be emphasized that in writing the equation 5.3.1, we are implicitly assuming a separation scale $r_{\min}$; at larger distances from a string $r > r_{\min}$ we consider $\nabla \varphi$ energy to be associated with θ_a; for $r < r_{\min}$ the gradient energy is considered as part of the string tension [29].

Any other set of UV physics which reduces to the effective description of Eq. (5.3.1) would present an equally valid way to study this string network. Our plan is to find a model without a large scale hierarchy, such that the IR behavior is also described by Eq. (5.3.1) with a large value for the string tension. Optimally, we want a model which is easy to simulate on the lattice with a spacing not much smaller than $r_{\min}$. Reading Eq. (4.2.10), the model must have Goldstone bosons with a decay constant f_a and strings with a large and tunable tension $T = \kappa \pi f_a^2$, with $\kappa \gg 1$. There can be other degrees of freedom, but only if they are very heavy (with mass $m \sim r_{\min}^{-1}$), and we will be interested in the limit that their mass goes to infinity. Finally, the string must have the correct Kalb-Ramond charge. Provided everything is derived from an action, this will be true if the Goldstone boson mode always winds by 2π around a loop which circles a string.

We do this by writing down a model of *two* scalar fields φ_1, φ_2, each with a U(1) phase symmetry. A linear combination of the phases is gauged; specifically, the fields are given electrical charges $q_1 \in \mathbb{Z}$ and $q_2 = q_1 - 1$ under a single U(1) gauge field. The orthogonal phase combination represents a global U(1) symmetry which will give rise to our Goldstone bosons. The role of the gauge symmetry will be to attach an abelian-Higgs string onto every global string, which will enhance the string tension. The added degrees of freedom are all massive off the string, achieving our intended effective description. The model falls under the general rubric of "frustrated cosmic strings" [96], but our motivation and some specifics (particularly our initial conditions) are different.

Specifically, the Lagrangian is

$$
\begin{aligned}
-\mathscr{L}(\varphi_1, \varphi_2, A_\mu) = &\frac{1}{4e^2} F_{\mu\nu} F^{\mu\nu} + \left| (\partial_\mu - i q_1 A_\mu) \varphi_1 \right|^2 + \left| (\partial_\mu - i q_2 A_\mu) \varphi_2 \right|^2 \\
&+ \frac{m_1^2}{8 v_1^2} \left(2\varphi_1^* \varphi_1 - v_1^2 \right)^2 + \frac{m_2^2}{8 v_2^2} \left(2\varphi_2^* \varphi_2 - v_2^2 \right)^2 \\
&+ \frac{\lambda_{12}}{2} \left(2\varphi_1^* \varphi_1 - v_1^2 \right) \left(2\varphi_2^* \varphi_2 - v_2^2 \right).
\end{aligned}
\tag{5.3.2}
$$

For simplicity we will specialize to the case

$$
\lambda_{12} = 0, \quad m_1 = m_2 = \sqrt{e^2 (q_1^2 v_1^2 + q_2^2 v_2^2)} \equiv m_e.
\tag{5.3.3}
$$

The model has 6 degrees of freedom; two from each scalar and two from the gauge boson. Symmetry breaking, $\varphi_1 = e^{i\theta_1} v_1 \sqrt{2}$ and $\varphi_2 = e^{i\theta_2} v_2 \sqrt{2}$, spontaneously breaks both U(1) symmetries and leaves five massive and one massless degrees of freedom. Specifically, expanding about a vacuum configuration, the fluctuations and their masses are

$$
\begin{array}{lll}
v_1 \to v_1 + h_1, & m = m_1 & (5.3.4) \\
v_2 \to v_2 + h_2, & m = m_2 & (5.3.5) \\
A_i \neq 0, & m = \sqrt{e^2 (q_1^2 v_1^2 + q_2^2 v_2^2)} \equiv m_e & (5.3.6) \\
(\theta_1, \theta_2) \to (\theta_1, \theta_2) + \omega(q_1, q_2), & \text{eaten by } A & (5.3.7) \\
(\theta_1, \theta_2) \to (\theta_1, \theta_2) + \theta_a \left(\frac{q_2}{q_1^2 + q_2^2}, \frac{-q_1}{q_1^2 + q_2^2} \right) & m = 0. & (5.3.8)
\end{array}
$$

We see that the choices in Eq. (5.3.3) have made all heavy masses equal.[2] To clarify, note that a gauge transformation $A_\mu \to A_\mu + \partial_\mu \omega$ changes $\theta_1 \to \theta_1 + q_1 \omega$ and $\theta_2 \to \theta_2 + q_2 \omega$. Therefore the linear combination of θ_1, θ_2 fluctuations with $\delta \theta_1 \propto q_1$ and $\delta \theta_2 \propto q_2$ is precisely the combination which can be shifted into A^μ by a gauge change, and is therefore the combination which is "eaten" by the A-field to become the third massive degree of freedom. The remaining phase difference $q_2 \theta_1 - q_1 \theta_2$ is gauge invariant,

$$q_2 \theta_1 - q_1 \theta_2 \to_\omega q_2(\theta_1 + q_1 \omega) - q_1(\theta_2 + q_2 \omega) = q_2 \theta_1 - q_1 \theta_2 + 0\omega \tag{5.3.9}$$

and represents a global, Goldstone-boson mode.

The model breaks two U(1) symmetries, so we must describe strings in terms of a double (m, n) representing the winding number of each scalar field around the string. In the absence of gauge interactions (for $e \to 0$) the φ_1, φ_2 fields would not interact and the tension of the $(1, 1)$ string would be the sum of the tensions of a $(1, 0)$ and a $(0, 1)$ string. Therefore the $(1, 1)$ string would be neutrally stable to splitting into $(1, 0)$ and $(0, 1)$ strings. Gauge interactions strongly change this, such that $(1, 0)$ and $(0, 1)$ strings strongly attract and $(1, 1)$ strings are stable. To show this we analyze the form of a (j, k) string. For the *Ansatz*

$$\sqrt{2}\varphi_1(r, \phi) = e^{ij\varphi} f_1(r) v_1,$$
$$\sqrt{2}\varphi_2(r, \phi) = e^{ik\varphi} f_2(r) v_2,$$
$$A_\phi(r) = \frac{g(r)}{r}, \tag{5.3.10}$$

we find the equations of motion from Eq. (5.3.2) are

$$g'' - \frac{g'}{r} = e^2 v_1^2 f_1^2 q_1(q_1 g - j) + e^2 v_2^2 f_2^2 q_2(q_2 g - k), \tag{5.3.11}$$

$$f_1'' + \frac{f_1'}{r} = \frac{f_1}{r^2}(j - q_1 g)^2 + \frac{m^2}{2} f_1(f_1^2 - 1), \tag{5.3.12}$$

$$f_2'' + \frac{f_2'}{r} = \frac{f_2}{r^2}(k - q_2 g)^2 + \frac{m^2}{2} f_2(f_2^2 - 1). \tag{5.3.13}$$

Here f_1, f_2 represent the progress of the two scalar fields towards their large-radius asymptotic vacuum values, while $2\pi g(r)$ is the magnetic flux enclosed by a loop at radius r, which trends at large r towards the total enclosed magnetic flux. The large-r behavior is well behaved only if $f_1 \to 1$, $f_2 \to 1$, and

$$\lim_{r \to \infty} g(r) = \frac{j q_1 v_1^2 + k q_2 v_2^2}{q_1^2 v_1^2 + q_2^2 v_2^2} = \frac{1}{2\pi}(\text{enclosed magnetic flux}). \tag{5.3.14}$$

The magnetic flux is therefore a compromise between the value j/q_1, which cancels large-distance gradient energies for the first field, and k/q_2, which cancels large-distance gradient energies for the second field. Unless $q_2 j - q_1 k = 0$, the gradient energies are not canceled at long distance. Indeed, we can

---

[2] We set $\lambda_{12} = 0$ so that the fluctuations in $|\varphi_1|$ and $|\varphi_2|$ are unmixed; our other choices ensure that all heavy fields have the same mass. We could consider other cases but we see no advantage in doing so if the goal is to implement the model on the lattice. The lattice spacing is limited by the inverse of the heaviest particle mass, while the size of the string core and the mass of extra degrees of freedom off the string will be set by the inverse of the lightest particle mass. So we get a good continuum limit with the thinnest strings, and therefore the best resolution of the network, by having all heavy masses equal.

understand the difference $(q_2 j - q_1 k)$ as the global (axionic) charge of the string. The gradient energy at large distance is given by

$$
\begin{aligned}
T &\simeq 2\pi \int r \, dr \left(|D_\phi \varphi_1|^2 + |D_\phi \varphi_2|^2 \right) \\
&\simeq \pi \int r \, dr \left(\frac{v_1^2}{r^2} \left(j - q_1 g \right)^2 + \frac{v_2^2}{r^2} \left(k - q_2 g \right)^2 \right) \\
&\simeq \pi \int \frac{dr}{r} \frac{v_1^2 v_2^2 (j q_2 - k q_1)^2}{q_1^2 v_1^2 + q_2^2 v_2^2},
\end{aligned}
\tag{5.3.15}
$$

which is proportional to the squared global charge of the string. Naming $q_{\text{global}} = j q_2 - k q_1$, comparing Eq. (1.0.1) with Eq. (5.3.15), we identify the Goldstone-mode decay constant as

$$
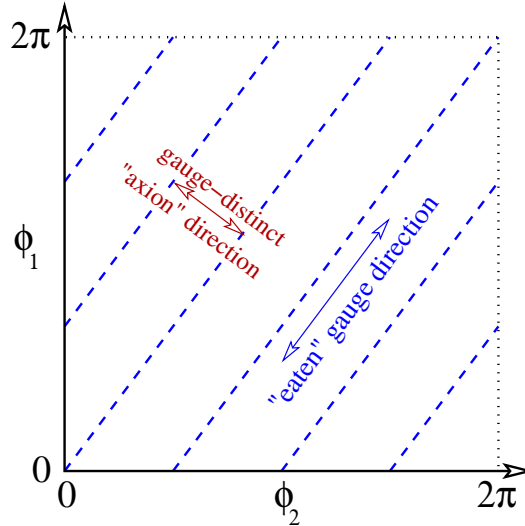f_a^2 = \frac{v_1^2 v_2^2}{q_1^2 v_1^2 + q_2^2 v_2^2}.
\tag{5.3.16}
$$

Figure 5.1.: Space of φ_1, φ_2 phases (θ_1, θ_2) for the case $(q_1, q_2) = (4, 3)$. The dashed (blue) line indicates phase pairs which are equivalent under gauge transformations. An appropriate vector potential can cancel any gradient energy in the direction of the dashed lines.

Because q_1 and q_2 are of the same sign, the resulting large-distance energy is smaller for the $(1, 1)$ string than for the sum of the $(1, 0)$ and $(0, 1)$ strings, and therefore there is an attractive interaction between $(1, 0)$ and $(0, 1)$ strings, which like to bind into a $(1, 1)$ string. Alternatively we could say that the global charge of the $(1, 0)$ string is q_2 and the $(0, 1)$ string is $-q_1$, so they are strongly attracted by the Goldstone-mediated interaction and bind into a $(1, 1)$ string.

For a more intuitive explanation, consider Figure 5.1. It shows the set of possible phases (θ_1, θ_2) for the two scalar fields, in the case $(q_1, q_2) = (4, 3)$. The figure includes a dotted line to indicate which phase choices are gauge-equivalent. Moving along the dotted line corresponds to changing the gauge, or moving through space along a gauge field; a vector potential of the right size can cancel a gradient energy along this field direction. The orthogonal direction, which is unaffected by a gauge field, is the global (axion) field direction. A change in this direction from one blue dotted line to the next represents a full 2π rotation in the (axial) Goldstone direction, which explains the value of f_a found in Eq. (5.3.16). Figure 5.2 then shows how gradient energies behave in a $(1, 0)$ or $(1, 1)$ string. As the scalar field value
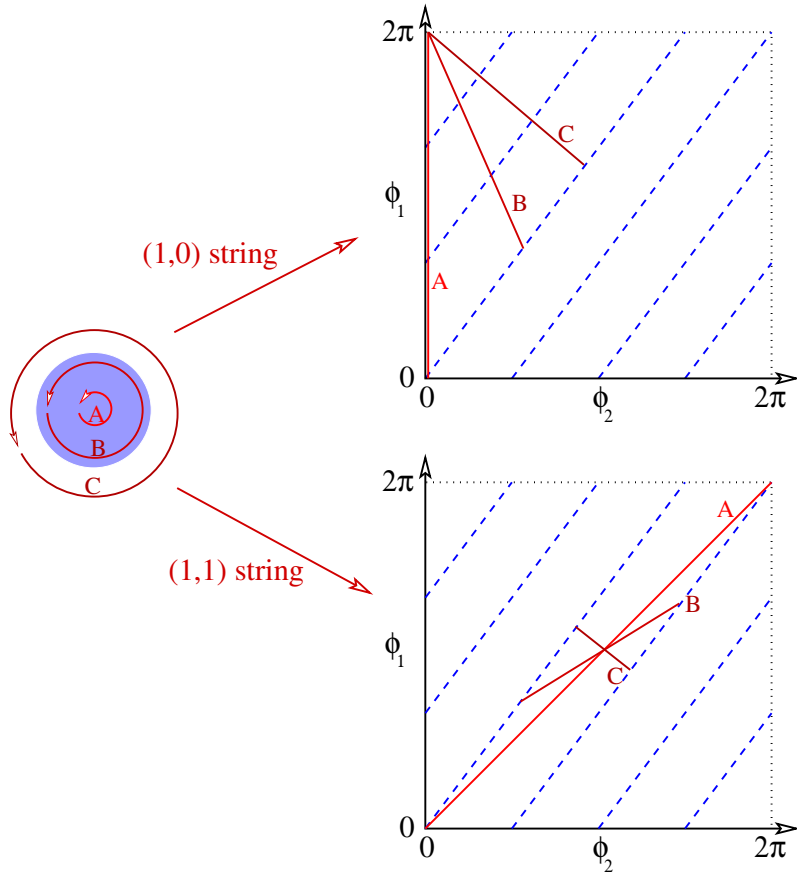
Figure 5.2.: Left: cross-section of a string, showing the magnetic field strength "bundle" and three possible loops one can take around the center of the string. Right: path through (ϕ_1, ϕ_2) space taken along each loop, for a $(1,0)$ string (top) and a $(1,1)$ string (bottom). As more magnetic flux is enclosed, the component of $(\Delta\theta_1, \Delta\theta_2)$ along the gauge-direction is canceled, but the component in the "global" direction is not. This component is small for the $(1,1)$ string.

varies around a loop, the gradient energy in the dotted-blue direction is partly canceled by A_ϕ gauge field. The extent of cancellation depends on the enclosed flux. As one goes from a small loop within the string core to a large loop outside the core, more and more of the scalar gradient along the dotted-line direction is canceled by the enclosed flux. For the innermost loop there is no enclosed flux, and the gradient energy is given by the distance between the point $(\theta_1, \theta_2) = (0,0)$ to the point $(2\pi, 0)$ or $(2\pi, 2\pi)$ for the $(1,0)$ or the $(1,1)$ string respectively. For a loop enclosing the entire flux, all gradient energy arising from the gauge-direction is canceled. This nearly completely removes the gradient energy for the $(1,1)$ string, but the reduction is modest for the $(1,0)$ string. Therefore the $(1,1)$ string has a small gradient energy outside the core, representing a small residual coupling to the (axion) Goldstone field, but the $(1,0)$ string has a large gradient energy and a large coupling.

For our simulation to correspond with the global string model, it should have Goldstone modes between a network of strings with charge-1 under the Goldstone fields. That is, we want a network of $(1,1)$ strings only, with no other string types. Because the $(1,1)$ string is stable, achieving this is simply a matter of choosing the right initial conditions. We choose θ_1 randomly and independently at each point, $A_\mu = 0 = E_i = \dot\varphi_1 = \dot\varphi_2$ initially, and $\theta_2 = \theta_1$. In this case only $(1,1)$ strings are present initially, and the network never develops any other sort of string or structure. Since $q_2\theta_1 - q_1\theta_2$ is initially random, there are no long-range correlations in the Goldstone field and the Kibble mechanism ensures a network of $(1,1)$ strings, whose evolution should approach the scaling behavior of a network with a tension set by

the $(1, 1)$ string tension and the Goldstone mode interaction strength found above. Our initial conditions also obey Gauss' Law, which is then preserved by the evolution.

Now let us estimate the effective value of κ, the ratio of the string tension to the string interaction via Goldstone modes, for such a $(1, 1)$ string. The energy of the string's core is the energy of an abelian Higgs string with $m_h = m_e$ and with $f^2 = v_1^2 + v_2^2$, which is

$$T_{\text{abelian}} \simeq \pi(v_1^2 + v_2^2). \tag{5.3.17}$$

The value of κ is therefore

$$\kappa = \frac{T}{\pi f_a^2} \simeq \frac{v_1^2 + v_2^2}{\frac{v_1^2 v_2^2}{q_1^2 v_1^2 + q_2^2 v_2^2}} = \frac{(v_1^2 + v_2^2)(q_1^2 v_1^2 + q_2^2 v_2^2)}{v_1^2 v_2^2} \xrightarrow{v_1 = v_2} 2(q_1^2 + q_2^2). \tag{5.3.18}$$

This is not quite correct; the solution only coincides with the abelian-Higgs solution for large $q_1 \gg 1$. For finite q_1 we must compute the true solution, and account for the $1/r^2$ tail of energy arising from the long-distance Goldstone-mode content of the string. Therefore we solve Eq. (5.3.11), Eq. (5.3.12), Eq. (5.3.13) numerically by multiparameter shooting to establish the string solution and its energy. Artificially separating the short and long distance energy contributions by choosing $r_{\min} = \pi/m$ and writing the energy-per-length stored in fields out to radius R as

$$T_R = \int_{r_{\min}}^{R} \frac{dT}{dr} dr \equiv (\bar{\kappa} + \ln(mR/\pi)) \pi f_a^2, \tag{5.3.19}$$

(or equivalently, $\bar{\kappa} = \lim_{R \to \infty} T_R / \pi f_a^2 - \ln mR/\pi$), we find the values of $\bar{\kappa}$ shown in Table 5.1. The table shows that Eq. (5.3.18) is quite accurate, for our choice of $r_{\min}$. For future use, the table also records the small-distance behavior of f_1, f_2, and g, defined as

$$\begin{aligned}
f_1(r) &= c_1 mr + \mathcal{O}(r^3), \\
f_2(r) &= c_2 mr + \mathcal{O}(r^3), \\
g(r) &= d(mr)^2 + \mathcal{O}(r^4).
\end{aligned} \tag{5.3.20}$$

Note that all results in the table are for the case of equal masses and equal vacuum values; we could achieve $\bar{\kappa}$ values intermediate between those shown by considering asymmetric vacuum values $v_1 > v_2$.

q_1	q_2	$\bar{\kappa}$	c_1	c_2	d
5	4	82.290	0.618084	0.582967	0.0547499
4	3	50.288	0.621225	0.576319	0.0697357
3	2	26.283	0.625697	0.563648	0.0954803
2	1	10.267	0.630809	0.532107	0.1476050

Table 5.1.: Numerical value of extra string tension $\bar{\kappa}$, and small-distance behaviors of radial functions, for several charge combinations.

To summarize, the model of Eq. (5.3.2) has an infrared description consisting of one Goldstone mode and strings. The strings have a tension $\kappa \pi f_a^2$ with tunable κ given by Eq. (5.3.18). The Goldstone phase winds by 2π in circling the string, so the Kalb-Ramond charge of the string is correct. This description breaks down at a scale $m_1 = m_2$, which is both the scale setting the thickness of the string and the scale of massive excitations off the strings.

Implementing this new method numerically leads to a simulation of tunable string tensions, where the

desired string tension for axion cosmology is in range $\kappa \in [48, 67]$. This range can be achieved by using $q_1 = 4$ and $q_2 = 3$.

Chapter 6

Nambu-Goto String Dynamics

In chapter 4 the equation of motion for the Nambu-Goto (NG) action was introduced, which is the effective string action for the local $U(1)$ symmetry. In this chapter the NG equation of motion is solved in the flat and FRW metric. The solution of the NG-action in flat space is used in the numerical part in chapter 9, to provide the exact string position and velocity when constructing a local string on the lattice. For this the loop solution for strings in flat space is needed [97]. Different string behaviors namely cusps, kinks and self-intersection are also explained in this chapter, where most of them can be shown on the Kibble-Turok sphere [98, 99]. Also we present a novel loop solution, which is cuspless, kinkless and non self-intersection. This solution is very important for constructing a string on a lattice if one would like to investigate the differences between the Nambu-Goto loop solution and local field strings. Strings with kinks, cusps or self-intersection can not be resolved correctly on the lattice due to the loss of validity of the Nambu-Goto action hence the curvature radius of the strings gets much smaller as the string core itself. No kind of solution which fulfills all conditions was published to our knowledge so far.

6.1 Minkowski Spacetime

The solution for the Nambu-Goto equation of motion, introduced in chapter 4, in Minkowski spacetime given by

$$g_{\mu\nu} = \eta_{\mu\nu} = \begin{bmatrix} 1 & 0 & 0 & 0 \\ 0 & -1 & 0 & 0 \\ 0 & 0 & -1 & 0 \\ 0 & 0 & 0 & -1 \end{bmatrix}, \tag{6.1.1}$$

can be expressed by using Eq. (4.1.8) to

$$\nabla^2 x^\mu = 0, \tag{6.1.2}$$

since $\Gamma^\mu_{\nu\rho} = 0$. Because of the degrees of freedom under the worldsheet reparametrization, we can choose a gauge, where a common choice is

$$\gamma_{01} = 0 \rightarrow \dot{x}^\mu x'_\mu = 0, \tag{6.1.3}$$

$$\gamma_{00} + \gamma_{11} = 0 \rightarrow \dot{x}^\mu \dot{x}_\mu + x'^\mu x'_\mu = 1, \tag{6.1.4}$$

which is called conformal gauge. The dots and primes denote derivatives with respect to t and σ. The equation of motions then reduce to

$$\partial_t \left(\frac{(\dot{x}x')x'^\mu + x'^2\dot{x}^\mu}{\sqrt{(\dot{x}x')^2 - \dot{x}^2 x'^2}} \right) + \partial_\sigma \left(\frac{(\dot{x}x')\dot{x}^\mu + \dot{x}^2 x'^\mu}{\sqrt{(\dot{x}x')^2 - \dot{x}^2 x'^2}} \right) = \ddot{x}^\mu - x''^\mu = 0, \tag{6.1.5}$$

which is the wave equation. Since we used $\tau = t$, the physical velocity of the string is $\dot{x}$. All constraints are therefore

$$\dot{x}x' = 0, \qquad (6.1.6)$$

$$\dot{x}^2 + x'^2 = 1, \qquad (6.1.7)$$

$$\ddot{x} - x'' = 0. \qquad (6.1.8)$$

The energy-momentum tensor can be expressed as

$$T^{\mu\nu} = \mu \int d\sigma (\dot{x}^\mu \dot{x}^\nu - x'^\mu x'^\nu) \delta^3(x - x(\sigma, t)), \qquad (6.1.9)$$

which leads to the energy

$$E = \int T^{00} d^3 x = \mu \int d\sigma. \qquad (6.1.10)$$

That is σ is proportional to the string energy. The general solution of the wave equation is [97, 100, 101]

$$x(\sigma, t) = \frac{1}{2} [a(\eta) - b(\xi)] \frac{L}{2\pi}, \qquad (6.1.11)$$

where $a(\eta)$ and $b(\xi)$ are called the right and left moving string parts, with $\xi = \frac{2\pi(\sigma - t)}{L}$ and $\eta = \frac{2\pi(\sigma + t)}{L}$. For a normalized string we choose $L = 2\pi$. Taking the time and spatial derivative of the solution we get

$$\dot{x}(\sigma, t) = \frac{1}{2} [\partial_\sigma a(\sigma + t) \partial_t t - \partial_\sigma b(\sigma - t) \partial_t(-t)] = \frac{1}{2} [a' + b'], \qquad (6.1.12)$$

$$x'(\sigma, t) = \frac{1}{2} [\partial_\sigma a(\sigma + t) - \partial_\sigma b(\sigma - t)] = \frac{1}{2} [a' - b']. \qquad (6.1.13)$$

Inserting Eq. (6.1.6), Eq. (6.1.6) and Eq. (6.1.12), Eq. (6.1.13) we yield

$$\dot{x}x' = a'^2 - b'^2 = 0 \qquad \rightarrow \qquad a'^2 = b'^2, \qquad (6.1.14)$$

$$\dot{x}^2 + x'^2 = \frac{a'^2 + b'^2}{2} = 1 \qquad \rightarrow \qquad a'^2 = b'^2 = 1. \qquad (6.1.15)$$

We will now consider solutions which form a closed string.

6.1.1   Oscillating Loop Solution

For a closed string we require the periodicity

$$x(\sigma + L, t) = x(\sigma, t), \qquad (6.1.16)$$

where the left and right moving parts also obey

$$a(t + L) = a(t) \qquad b(t + L) = b(t). \qquad (6.1.17)$$

The periodicity for time is the same as for space, therefore the actual periodicity until a string repeats its motion is $L/2$ since

$$x(\sigma + L/2, t + L/2) = x(\sigma, L + t) = x(\sigma + L, t) = x(\sigma, t). \tag{6.1.18}$$

The periodicity can be even shorter, if the string has a special loop trajectory. The average velocity is

$$\langle \dot{x}^2 \rangle = \int \frac{dt}{2\pi} \int \frac{d\sigma}{2\pi} \dot{x}^2 = \int \frac{dt}{2\pi} \int \frac{d\sigma}{2\pi} \left(\frac{1}{2} - \frac{1}{2} a'b' \right) = \frac{1}{2}, \tag{6.1.19}$$

where $\int a'b' = 0$ because of integration over an periodic string. Therefore the average velocity in flat space is constant. The easiest loop solution is a static planar circular loop given by

$$x(\sigma, t) = \begin{bmatrix} \sin(\eta) + \sin(\xi) \\ -\cos(\eta) - \cos(\phi)\cos(\xi) \\ -\sin(\phi)\cos(\xi) \end{bmatrix}, \tag{6.1.20}$$

where ϕ is a constant parameter. In terms of $a'(\eta)$ and $b'(\xi)$ which we use as the standard notation for string loop solutions it is expressed as

$$a'(\eta) = \begin{bmatrix} \cos(\eta) \\ \sin(\eta) \\ 0 \end{bmatrix}, \tag{6.1.21}$$

$$b'(\xi) = \begin{bmatrix} \cos(\xi) \\ \cos(\phi)\sin(\xi) \\ \sin(\phi)\sin(\xi) \end{bmatrix}. \tag{6.1.22}$$

There is a wide set of loop solutions, which can be seen in appendix E. Loops can have interesting properties, which includes self intersection, cusps and kinks. To have a better impression of these loop behaviors it is useful to map the solution on the Kibble-Turok sphere.

6.1.2 Kibble Turok Sphere

The right- and left-moving functions $a(\sigma + t)$ and $b(\sigma - t)$ can be mapped on a unit sphere which is called Kibble-Turok sphere, see figure 6.1a. For a closed loop with its center of mass at rest we have

$$\int_0^L x' d\sigma = \int_0^L \frac{1}{2}(a' - b') = 0, \tag{6.1.23}$$

$$\int_0^L \dot{x} d\sigma = \int_0^L \frac{1}{2}(a' + b') = 0. \tag{6.1.24}$$

Because of

$$\int a' d\sigma = \int b' d\sigma = 0, \tag{6.1.25}$$

neither of the two curves can lie only in one hemisphere. If there is for one value $\sigma = \sigma_0$ and $t = t_0$ such one point which is $a'(\sigma_0, t_0) = b'(\sigma_0, t_0)$, then

$$\dot{x}(\sigma_0, t_0 + nL) = 1, \qquad (6.1.26)$$

where $n \in \mathbb{N}$. This is called a cusp, where the string moves at on point with the speed of light and achieves $\gamma \to \infty$. A schematic representation for a cusp can be seen in figure 6.1b. Cusps represents an intersection point on the Kibble-Turok sphere for a' and b'. If the functions a' or b' are discontinuous the string posses sharp curves which are called kinks, see figure 6.1c. Loops can also self-intersect which happens if

$$\int_{\sigma}^{\sigma+l} a'(\tilde{\sigma} - t) d\tilde{\sigma} - \int_{\sigma}^{\sigma+l} b'(\tilde{\sigma} + t) d\tilde{\sigma} \neq 0 \qquad \forall \sigma, l, t \in [0, 2\pi]. \qquad (6.1.27)$$

Unfortunately this cannot be depicted on the Kibble-Turok sphere. But one can create a movie, starting with the left and right moving part on the Kibble-Turok sphere. Calculating Eq. (6.1.27) step by step and mapping it onto the sphere, the left and right moving parts start to shrink to the center of the sphere until they reached their minimum and starts to grow again. If they do not touch during this process the string will never self intersect.

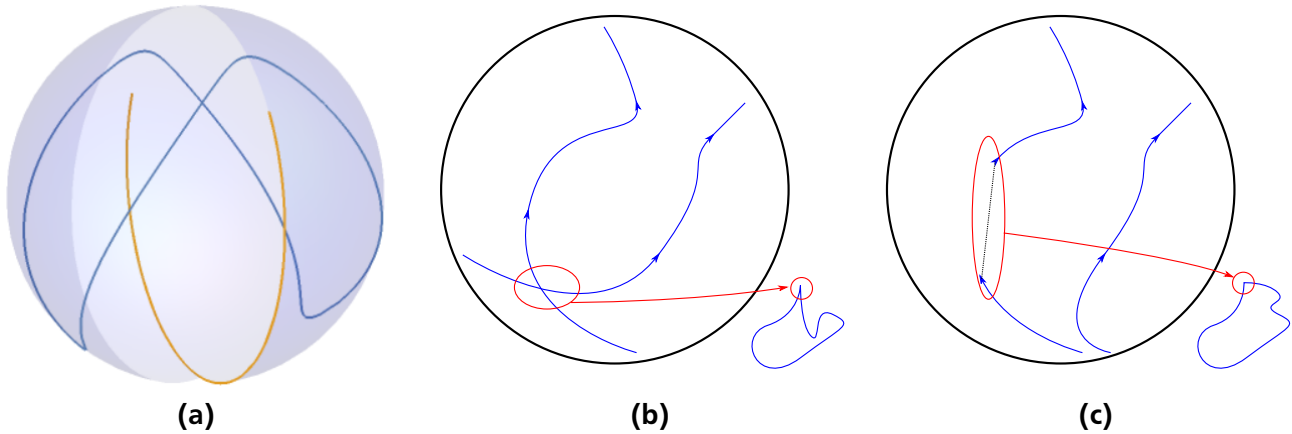(a)   (b)   (c)

Figure 6.1.: Schematic picture of the Kibble-Turok sphere in 6.1a, where the equation of motion mapped on this sphere is cuspless, kinkless and non self-intersecting. In figure 6.1b a sketch of the sphere with a cusp is shown, where in figure 6.1c a kink is depicted.

Coming back to loop solutions, as mentioned before, we want to simulate local strings with initial conditions given by loop solutions. The principle to implement a string on the lattice is independent of the loop solution but the resolution of the lattice is constant and therefore strings with kinks, cusps or self-intersections will have at a specific time t_* a string segment, which cannot be resolved correctly on the lattice. Also cusps and kinks are singular points, where the curvature radius goes to zero and the Nambu-Goto action is not anymore an effective description for local strings. Despite that, for strings which intercommute or self-intersect, it is known that the velocity has to be at least $v > 0.9$, at the intersection point, to have a reconnecting string [102]. To avoid these problems we need a string which is kinkless, cuspless, and non self-intersecting.

A solution which provides all three conditions can be constructed by regarding the repetition of the left a' and right b' moving part of the string solution;

$$
a' = \begin{bmatrix} \cos(\eta)\sqrt{1-a_z^2} \\ \sin(\eta)\sqrt{1-a_z^2} \\ \frac{3}{4}\cos(2\eta) \end{bmatrix},
\tag{6.1.28}
$$

$$
b' = \begin{bmatrix} \sqrt{\frac{8}{9}}\sin(2\xi)\sqrt{1+8\cos^6(2\xi)} \\ 0 \\ -(\frac{2}{3}\cos(4\xi)+\frac{1}{3}\cos(8\xi)) \end{bmatrix}.
\tag{6.1.29}
$$

Note that this solution has no analytical expression for $x(\sigma, t)$, since the integral of a' turns out to be elliptical. This solution fulfills always Eq. (6.1.27) and the kibble turok sphere of this solution can be seen in figure 6.1a.

6.1.3 Intercommuting Strings

String interactions with two strings can be described by two different loop solutions

$$
x_1(\sigma, t) = a_1 - b_1,
\tag{6.1.30}
$$
$$
x_2(\sigma, t) = a_2 - b_2,
\tag{6.1.31}
$$

where a_i and b_i are again the left and right moving parts. If these strings intersect, there is a time $t = t_*$ where this intersection occurs. At this time

$$
x_1(\sigma_*, t_*) = x_2(\sigma_*, t_*),
\tag{6.1.32}
$$

but not necessarily

$$
a_1(\sigma_*, t_*) = a_2(\sigma_*, t_*) \quad \& \quad b_1(\sigma_*, t_*) = b_2(\sigma_*, t_*),
\tag{6.1.33}
$$

is fulfilled. Note that the intersection occurs only at a specific point σ_*. We can again place the functions a_1', a_2', b_1' and b_2' on the surface of the Kibble-Turok sphere, which is shown in figure 6.2a. The point of intersection is marked on each function as a dot, where we can have two possible outcomes. First they just pass through as it can be seen in figure 6.2b. The strings then did not influence each other. Second they can intercommute as it can be seen in figure 6.2c. If strings intercommute, kinks appear and the new string gets a more complex structure. However, the Nambu-Goto solution does not provide any answer to the question of the intersection behavior.
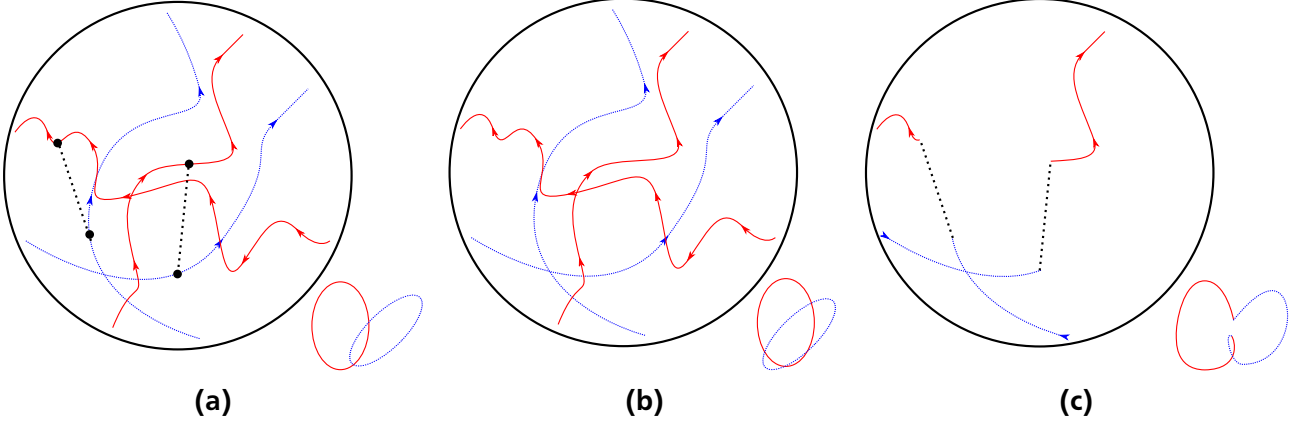
Figure 6.2.: Two left and right moving string trajectories are intercommuting in figure 6.2a, where the dashed line indicates the possible outcome. In figure 6.2b the two strings pass through each other and do not intercommute where in figure 6.2c the strings intersects and a kink appears.

6.2 Friedman-Robertson-Walker Spacetime

Strings in an expanding Universe can be described by the FRW-metric, where we use the conformal time τ with $d\tau = dt/a$. The metric is then

$$g_{\mu\nu} = a(\tau)^2 n_\mu \nu = a(\tau)^2 \begin{bmatrix} 1 & 0 & 0 & 0 \\ 0 & -1 & 0 & 0 \\ 0 & 0 & -1 & 0 \\ 0 & 0 & 0 & -1 \end{bmatrix}, \tag{6.2.1}$$

Fixing the gauge the same as in flat space with the exception that we can only keep the traverse gauge condition

$$\dot{x} x' = 0, \qquad \xi^0 = \tau. \tag{6.2.2}$$

The equation of motions for the general Nambu-Goto action Eq. (4.1.6) reduces to

$$\ddot{x} + 2H(1 - \dot{x}^2) = \epsilon^{-1}(x'\epsilon^{-1})', \tag{6.2.3}$$

$$\dot{\epsilon} + 2H\epsilon\dot{x}^2 = 0, \tag{6.2.4}$$

where $H = \dot{a}/a$ and $\epsilon = \frac{x'}{\sqrt{1-\dot{x}^2}}$. The dots here are derivatives respectively to conformal time τ. The Hubble parameter has a damping effect on the string motion. The energy-stress tensor is given by

$$T^{\mu\nu} = \frac{\mu}{a^4} \int d\sigma \left(\epsilon \dot{x}^\mu \dot{x}^\nu - \frac{x'^\mu x'^\nu}{\epsilon} \right) \delta^3(x - x(\sigma, \tau)). \tag{6.2.5}$$

The energy can be expressed by

$$E = \mu a(\tau) \int \epsilon d\sigma, \tag{6.2.6}$$

where the rate of change of the energy is

$$\dot{E} = H\left(1 - 2\left\langle v^2 \right\rangle\right)E\,. \tag{6.2.7}$$

The averaged string velocity is

$$\langle v \rangle^2 = \frac{\int \dot{x}^2 d\sigma}{\int d\sigma}\,. \tag{6.2.8}$$

Unlike for flat space metric the rate of change for the energy in the FRW metric is $\dot{E} \neq 0$. Due to the stretching of the Universe, on large scales one would expect that the velocity is reduced in comparison to the flat space velocity, that is $\langle v_{\text{FRW}}^2 \rangle < \langle v_{\text{flat}}^2 \rangle$.

6.2.1 Scaling Solution

To understand the evolution of a network of strings, scaling is an important factor. One tries to find statistical properties of a string network, which stays the same a different times after scaling is reached. We can rewrite Eq. (6.2.4) by using the string energy density

$$\rho \approx \frac{E}{a^3}\,, \tag{6.2.9}$$

and Eq. (6.2.8), which leads to

$$\frac{d\rho}{dt} + 2H(1 + v^2)\rho = 0\,. \tag{6.2.10}$$

This equation has long strings or infinite strings and loops included. Strings are expected to behave like Brownian strings if they are long strings. The correlation length L, which describes the average distance of two strings, divide long strings $L > l$ and loops $L < l$ into two segments. The network density for Brownian strings can be reexpressed by

$$\rho_\infty = \frac{\mu}{L^2}\,, \tag{6.2.11}$$

where ∞ stands for long strings. The equation of motion can be rewritten in terms of the correlation length

$$2\frac{dL}{dt} = 2HL(1 + v_\infty^2) + \frac{L}{\rho_\infty}\left(\frac{d\rho_\infty}{dt}\right)_{\text{to loops}}\,. \tag{6.2.12}$$

The last term is the contribution of energy losses due to small loops, which is expressed as

$$\left(\frac{d\rho_\infty}{dt}\right)_{\text{to loops}} = \tilde{c}\,v_\infty\frac{\rho_\infty}{L}\,. \tag{6.2.13}$$

The parameter $\tilde{c}$ is the chopping efficiency and is in literature assumed to be a constant parameter.

Chapter 7

Numerical Methods

The main results this thesis provides are determined by numerical simulations. Therefore, we will present some more insight into the applied simulation techniques. The focus in this chapter is on lattice simulations for field theories, which will be discussed in great detail for the global U(1) symmetry introduced in chapter 5. Lattice simulations can be realized by constructing a grid with points, where each point is connected by a link, see figure 7.1. For U(1) field theory in (3+1)D, where 3D denotes the spatial directions and 1D the time direction. The scalar fields ϕ live on the lattice points and the vector fields A on the links. For a global U(1) symmetry there are no vector fields which is equivalent to set the links to the identity.
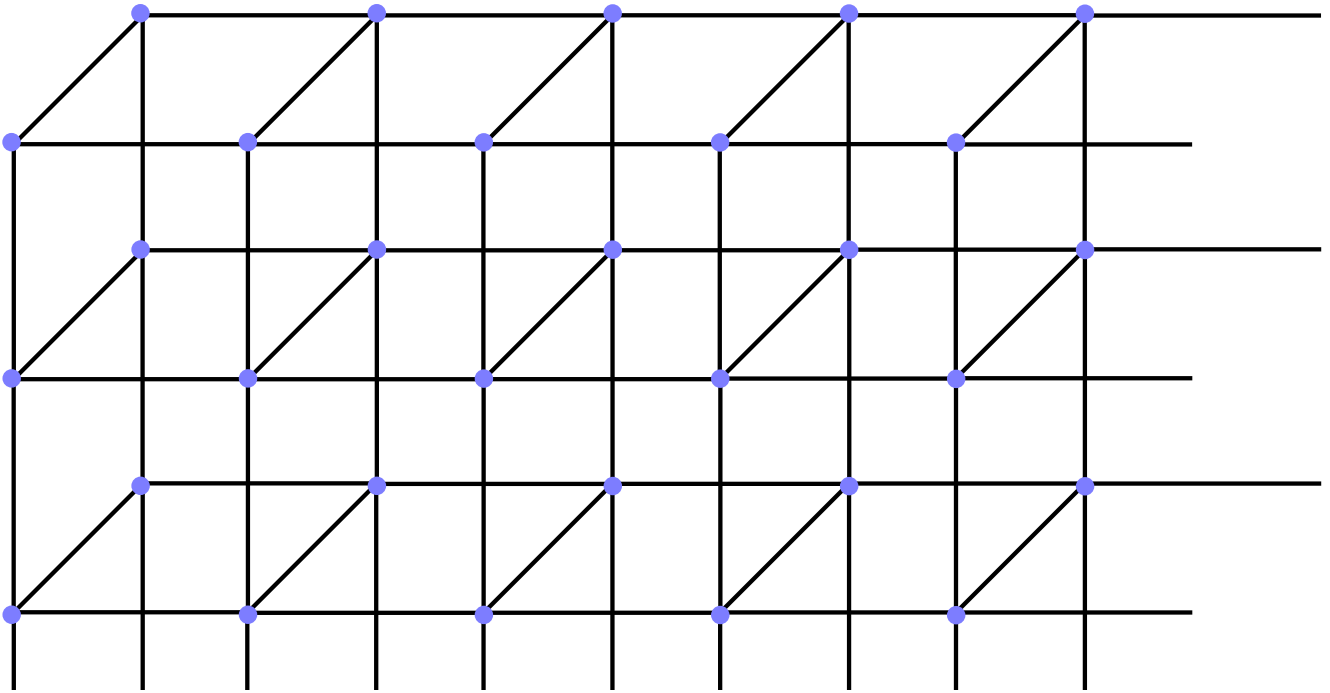

Figure 7.1.: Sketch of a lattice, where the blue points indicate the region, where scalar fields ϕ are living and the black links corresponds to the vector fields A.

7.1 Lattice Discretization

Considering a spontaneous and explicit broken global U(1) symmetry, we start with the action in FRW-spactime, as introduced in chapter 3,

$$S = \int d^4x\, \tau^n (-(\partial_\tau \phi)^2 + (\nabla \phi)^2 + V(\phi)), \tag{7.1.1}$$

where the fields are

$$\phi = \frac{1}{\sqrt{2}}(\phi_r + i\phi_i) = \frac{f(r)}{\sqrt{2}}(\cos(\theta) + i\sin(\theta)),\tag{7.1.2}$$

with θ the phase of the axion field. The potential is

$$V(\phi) = \frac{\lambda}{8}(f_a^2 - 2|\phi|^2)^2 - \frac{L}{\sqrt{2}}(\phi + \phi^*),\tag{7.1.3}$$

where $L = m_a^2 f_a^2$. The last part of the potential uses the common approximation for

$$V(\phi)_{\text{anomaly}} = \chi(T)(1 - \cos(\theta)) \propto (\phi + \phi^*).\tag{7.1.4}$$

The equation of motion is then

$$0 = \partial_\tau(\tau^n \dot{\phi}) + t^n \nabla^2 \phi + \tau^n \frac{\partial V}{\partial \phi^*}.\tag{7.1.5}$$

Our goal is to discretize the equation of motion which then updates the field configuration for every time step $\Delta\tau$. For this finite differences are needed, where three forms are commonly known as: forward, backward, and central differences. For the derivative of a function $\partial_\tau \phi(x, \tau)$, one obtains in first order

$$\partial_\tau \phi(x, \tau) \approx \frac{\phi(x, \tau + \Delta\tau) - \phi(x, \tau)}{\Delta\tau},\tag{7.1.6}$$

$$\partial_\tau \phi(x, \tau) \approx \frac{\phi(x, \tau) - \phi(x, \tau - \Delta\tau)}{\Delta\tau},\tag{7.1.7}$$

$$\partial_\tau \phi(x, \tau) \approx \frac{\phi(x, \tau + \frac{\Delta\tau}{2}) - \phi(x, \tau - \frac{\Delta\tau}{2})}{\Delta\tau}.\tag{7.1.8}$$

Using first the central and then the forward and backward difference we get for the first part of Eq. (7.1.5)

$$\partial_\tau(\tau^n \dot{\phi}) = \frac{\left(\tau + \frac{\Delta\tau}{2}\right)^n \dot{\phi} - \left(\tau - \frac{\Delta\tau}{2}\right)^n \dot{\phi}}{\Delta\tau^2}\tag{7.1.9}$$

$$= \frac{\left(\tau + \frac{\Delta\tau}{2}\right)^n (\phi(\vec{x}, \tau + \Delta\tau) - \phi(\vec{x}, \tau)) - \left(\tau - \frac{\Delta\tau}{2}\right)^n (\phi(\vec{x}, \tau) - \phi(\vec{x}, \tau - \Delta\tau))}{\Delta\tau^2},$$

and therefore Eq. (7.1.5) reads

$$\underbrace{\phi(\vec{x}, \tau + \Delta\tau) - \phi(\vec{x}, \tau)}_{\dot{\phi}_{\tau + \Delta\tau}} = \frac{\left(\tau - \frac{\Delta\tau}{2}\right)^n}{\left(\tau + \frac{\Delta\tau}{2}\right)^n} \underbrace{[\phi(\vec{x}, \tau) - \phi(\vec{x}, \tau - \Delta\tau)]}_{\dot{\phi}_\tau}\tag{7.1.10}$$

$$+ \frac{\tau^n}{\left(\tau + \frac{\Delta\tau}{2}\right)^n} \Delta\tau^2 \left[\nabla^2 \phi(\vec{x}, \tau) + \frac{\partial V}{\partial \phi^*}\right].$$

This leads to an expression to calculate the difference of the fields $\phi(x, \tau + \Delta\tau)$ for the next time step. With Eq. (7.1.6) we also have a rule for the next time step with

$$\phi(\vec{x}, \tau + \Delta\tau) = \Delta\tau \dot{\phi}_{\tau + \Delta\tau} + \phi(\vec{x}, \tau).\tag{7.1.11}$$

Therefore the field gets updated by the calculated time difference of the field, this approach is called leapfrog. The spatial derivative in the Eq. (7.1.5) is

$$\nabla^2 \phi(\vec{x}, \tau) = \frac{1}{a^2} \sum_{i=0}^{3} \frac{4}{3} \left(\phi(\vec{x} + \Delta \vec{x}_i, \tau) + \phi(\vec{x} - \Delta \vec{x}_i, \tau) \right) - \frac{1}{12} \left(\phi(\vec{x} + 2\Delta \vec{x}_i, \tau) + \phi(\vec{x} - 2\Delta \vec{x}_i, \tau) \right)$$

(7.1.12)

$$- \frac{5}{2} \phi(\vec{x}, \tau),$$

where a is the spatial step size and refereed as the lattice spacing. This is the improved second order form of the Laplacian finite-differences and we call lattice calculation improved if this form is implemented. The ratio of lattice spacing to time spacing has to obey the Courant-number

$$c = \frac{\dot{\phi} \Delta \tau}{a},$$

(7.1.13)

where it is claimed that a simulation is stable if $c < 1$. The boundaries for the lattice are chosen to be periodic

$$\phi \left(\left[n_x, n_y, n_z \right], \tau \right) = \phi(\vec{0}, \tau),$$

(7.1.14)

under the assumptions that $x_i < n_i$ with n_i the lattice size. This represents for the connection for a 3D lattice the surface of a 4D torus. To get a more clear picture, consider a 2D lattice, which is a sheet with points, mapping this sheet on a 3D torus surface shows the constraints how fields are connected. That is, if a wave propagates through the boundary, it reenters the lattice at the other side.

7.2 Lattice Units

Before we can start simulating the equation of motion we derived, we will redefine the units of the equation to be consistent with lattice, that is we choose $f_a = 1$ and the saxion mass $m_s^2 = \lambda$. Due to the dependency of the topological susceptibility and the axion mass, we expect that the axion mass depends on temperature with $m_a^2 = T^{-m}$, where $m \approx 7.66$. If we consider simulations in the radiation dominated era, with the Hubble parameter $H \propto$ we can achieve the relation $T \propto \tau^{-1}$, which leads to $L = \tau^m$. It is usual to define

$$m_a(\tau_0)\tau_0 = 1,$$

(7.2.1)

where τ_0 is the time where the axion starts gaining mass or the time where the explicit breaking of the potential starts to show up. We can write

$$\frac{L}{\tau^n} = \frac{L_0}{\tau_0^n},$$

(7.2.2)

$$L = \left(\frac{\tau}{\tau_0^2} \right)^2.$$

(7.2.3)

The saxion mass corresponds to the string core size $\delta = m_s^{-1} = \tau^{-1}$, which decreases during the evolution by conformal time. This leads to a problem if the size shrinks during time below the lattice spacing. One can fix the saxion mass to the lattice size with am_s which is then constant during time evolution, this is also called fat string solution. To simulate cosmological axions one has to choose initial conditions

for ϕ and $\Delta\phi$, where $\phi_r = \cos(\theta)$ and $\phi_i = \sin(\theta)$ with $\theta \in [0, 2\pi]$ a random number and for $\dot{\phi} = 0$. That is, the simulation starts right after spontaneous symmetry breaking $T < T_{PQ}$ and leads to a dense string network. For $T \sim T_{QCD}$ the anomaly potential $V(\phi)_{\text{anomaly}}$ starts rising and domain walls form. This leads to a collapse of the string wall network. The phase of the fields, after all topological defects disappeared, can then be used to calculate the axion density of the simulation. Now the challenging part for performing such simulations is to tune the time τ_0 when the axion gains its mass or domain walls start to form. The physical interesting region is at $m_s\tau \sim f_a/H$ where $f_a \sim 10^{11}$ GeV and $H \sim 10^{-19}$ GeV, which leads to $m_s\tau \sim 10^{30}$. As we have seen the saxion mass depends on the lattice spacing where the size of the lattice is limited by RAM. Nowadays, supercomputers are able to achieve $m_s\tau \sim 10^4$ which is extremely small in comparison to 10^{30}. In the next chapter we will present the two-Higgs method, which provides a solution for this problem.

Chapter 8

Two-Higgs Simulations

In section 5.3 the theoretical setup of the two-Higgs method was already discussed. In this chapter we will perform analysis to achieve the axion mass by using the correct string tension numerically. First, it is explained how the new method is implemented on the lattice. Furthermore, we compare string networks for the new method with global and local $U(1)$ string networks, which is mainly part of our publication (Klaer et al., 2017 [92]). In the second part, we present the results, when the explicit symmetry gets broken, which leads to a string domain wall network. These simulations allow us to extract the axion number density at the end of the simulation and determine the axion mass for the first time with the correct string tension. This is mainly part of our publication (Klaer et al., 2017 [103]).

8.1   Lattice Implementation

For an FRW spacetime in comoving coordinates and conformal time t, the action is

$$S = \int_0 dt \int d^3x \, t^n \mathscr{L} \tag{8.1.1}$$

where k is determined by the expansion rate, as introduced in section 3.2.[1] In our case only radiation is relevant, for which $k = 2$.[2] The Lagrangian of the two-Higgs model, introduced in section 5.3, reads

$$-\mathscr{L} = \frac{1}{4e^2} F_{\mu\nu}F^{\mu\nu} + \left|(\partial_\mu - iq_1 A_\mu)\varphi_1\right|^2 + \left|(\partial_\mu - iq_2 A_\mu)\varphi_2\right|^2$$

$$+ \frac{m_1^2}{8v_1^2}\left(2\varphi_1^*\varphi_1 - v_1^2\right)^2 + \frac{m_2^2}{8v_2^2}\left(2\varphi_2^*\varphi_2 - v_2^2\right)^2$$

$$+ \frac{\lambda_{12}}{2}\left(2\varphi_1^*\varphi_1 - v_1^2\right)\left(2\varphi_2^*\varphi_2 - v_2^2\right). \tag{8.1.2}$$

Our approach is to write a spacetime-lattice discretization of the action and to determine the update rule by extremization of this action. This leads automatically to a leapfrog update rule. We use noncompact formulation of U(1), recording gauge fields $A_i(x)$ (which "live" on links) directly and computing link variables

$$U_i(x) = \mathrm{P} \cdot \exp \int_x^{x+a\hat{i}} -iA_i dl = \mathrm{e}^{-iaA_i(x)} \tag{8.1.3}$$

when needed. In the following, when directly expressing the gauge field, we write aA_i as simply A_i, absorbing the factor of the lattice spacing. We use an a^2 improved action, both for the scalar fields and the gauge fields. To our knowledge this has not been done correctly before in simulating abelian Higgs fields for cosmic string networks. Our implementation is almost the same as a previous attempt to a^2-

---

[1]   We introduced there the expansion rate n which represents our k

[2]   The potential terms would scale as t^{2k} if we kept the masses fixed in physical units. But since the masses are an artifice to regulate string thickness, we keep them fixed in lattice units and scale them in the same way as the other terms.

improve the abelian Higgs mechanism [104], except that we correctly modify the electric field part, see below. The improved scalar field "hopping" term is (4/3) times a nearest-neighbor term minus (1/12) a next-nearest neighbor term,

$$S_{\nabla\varphi} = \sum_{t=\delta n_t a} \sum_{x=a\vec{n}_x} \left[\sum_{i=1,2,3} t^k \left(\frac{4|U_i^q(x,t)\varphi(x+a\hat{i},t) - \varphi(x,t)|^2}{3} \right. \right.$$
$$\left. \left. - \frac{|U_i^q(x,t)U_i^q(x+a\hat{i},t)\varphi(x+2a\hat{i},t) - \varphi(x,t)|^2}{12} \right) \right]$$
$$- (t+\delta a/2)^k \frac{|U_0^q(x,t)\varphi(x,t+\delta a) - \varphi(x,t)|^2}{\delta^2}, \qquad (8.1.4)$$

with q the charge for the specific field considered, and δ the ratio of temporal to spatial discretization; we typically use $\delta = 1/6$ which is adequate [24]. In practice we fix to temporal gauge, $U_0 = 1$, which is numerically convenient but not very relevant as long as we ask only gauge invariant questions.

The noncompact magnetic field action is (5/3) a square plaquette term minus (1/12) a sum on rectangular plaquettes (the abelian version of the tree-level a^2 improved or Symanzik action [105, 106]),

$$S_B = \sum_{t,x,i>j} \frac{5t^k}{6e^2} \left(A_i(x) + A_j(x+a\hat{i}) - A_i(x+a\hat{j}) - A_j(x) \right)^2$$
$$- \sum_{t,x,i\neq j} \frac{t^k}{24e^2} \left(A_i(x) + A_i(x+a\hat{i}) + A_j(x+2a\hat{i}) - A_i(x+a[\hat{i}+\hat{j}]) - A_i(x+a\hat{j}) - A_j(x) \right)^2 \qquad (8.1.5)$$

while the electric field action is

$$S_E = -\sum_{t,x,i} (t+a\delta/2)^k \left[\frac{2}{3} \frac{(A_i(x,t+\delta a) - A_i(x,t))^2}{\delta^2} \right.$$
$$\left. - \frac{1}{24} \frac{(A_i(x,t+a\delta) + A_i(x+a\hat{i},t+a\delta) - A_i(x,t) - A_i(x+a\hat{i},t))^2}{\delta^2} \right]. \qquad (8.1.6)$$

This last modification, explained in detail in [107], is necessary to make the evolution truly improved – for instance, without it the gauge boson dispersion relation has a^2 corrections. Unfortunately it causes the A-field update to be implicit. To see this, first define $E_i(x,t) = A_i(x,t+a\delta) - A_i(x,t)$. Then S_E can be written as $\sum_{x,i}(7/12)E_i^2(x) - (1/12)E_i(x)E_i(x+a\hat{i})$. Because the Lagrangian is not simply diagonal in the $E \sim \dot{A}$, there is a difference between the time derivative of A and the canonical momentum of A. It is convenient to define the quantity $P_i(x) = -(1/12)E_i(x-a\hat{i}) + (7/6)E_i(x) - (1/12)E_i(x+a\hat{i})$, which in the continuous-time limit is the canonical momentum of the A field. Its time-update is simple, but the relation between P and E must be inverted to update the A field. Because the relation is nearly diagonal, this inversion can be done perturbatively and proves not to be a large numerical overhead.[3] (In [107] this was the dominant cost, because the reference works with SU(2) where E is a gauge non-singlet and parallel transportation is involved in inverting the E-P relation.) The Lagrangian introduced in

---

[3] This procedure can be thought of as putting a tridiagonal matrix M, with diagonal elements $[\frac{-1}{12}, \frac{7}{6}, \frac{-1}{12}]$, in the Hamiltonian for a column of E-fields in one direction, $H(E) = \sum_i EME/2$. An alternative with a simpler update would be to define N a tridiagonal matrix with diagonal elements $[\frac{1}{12}, \frac{5}{6}, \frac{1}{12}]$ and to use $H(E) = EN^{-1}E/2$. These are equivalent at order a^2. In the latter case we would have $P = N^{-1}E$ or $E = NP$. One then stores and updates P, and easily generates $E = NP$ when needed to perform the A-field update. No matrix inversions are required. In each case the energy in electric fields is determined from $\sum_x E_i P_i/2$. We did not implement this procedure, but we would use it if we were writing the code from new.

8. Two-Higgs Simulations

5.3.2 does not provide the topological susceptibility part of the potential (which breaks the global U(1) symmetry, "tilting" the potential for the axion field). It can be implemented as

$$t^2 \chi(t)\left(1 - \cos \text{Arg}\, \theta_a\right) \Rightarrow \frac{f_a^2 t^{n+2}}{t_*^{n+4}} F(2\varphi_1^* \varphi_1) F(2\varphi_2^* \varphi_2)\left(1 - \cos\left(q_2 \text{Arg}\, \varphi_1 - q_1 \text{Arg}\, \varphi_2\right)\right) \qquad (8.1.7)$$

$$F(r) \equiv \begin{cases} \frac{25}{16} r\left(\frac{8}{5} - r\right), & r < \frac{4}{5}, \\ 1, & r > \frac{4}{5}. \end{cases} \qquad (8.1.8)$$

The function $F(r)$ is inserted to soften the behavior of the susceptibility term in string cores; without this term the introduced potential becomes violently nondifferentiable wherever $\varphi^* \varphi \sim 0$ for either field, which causes problems for space-discretized equations of motion. The modification only changes the tilted potential inside string cores, where its effect is very subdominant to the leading potential terms. But without this modification we do not get consistently stable evolution near string cores. Our results are insensitive to the specific form of $F(r)$, provided $F(1) = 1$, $F'(1) = 0$, $F(0) = 0$, and $F'(r)$ is continuous, which motivated our choice. A similar modification is common in single-scalar simulations of axionic strings, where most authors [41,43] have made the substitution $(1 - \cos \text{Arg}\, \varphi) \rightarrow \sqrt{2}\, \text{Re}\, \varphi$, a substitution which is correct only for the angular dynamics and only where $2\varphi^* \varphi = 1$. This replacement is justified because it is simpler, is nonsingular at 0, and is only of much influence outside string cores, where it is nearly equivalent to the correct form. We have explicitly checked that in the single-scalar model, axion production and string dynamics are nearly indistinguishable whether we use $(1 - \cos \text{Arg}\, \varphi)$ or $\sqrt{2}\, \text{Re}\, \varphi$ as the "tilt" in the potential.

To identify the plaquettes pierced by a string, we are using the gauge-invariant definition of Kajantie *et al* [108], applied to one of the fields (we use φ_1). We measure string velocity by a slight generalization of the method of [24]; we use the small-r expansion of $f_1(r)$:

$$f_1(r) = c_1 mr + e_1(mr)^3 + \ldots \qquad e_1 = -\frac{c_1(1 + 4q_1 d)}{16}, \qquad (8.1.9)$$

and we use the string velocity estimate that near the center of a string core, [24]

$$\gamma^2 v^2 = \frac{|\partial_t \phi|^2}{2m^2 c_1^2 v^2}\left(1 - \frac{4e_1 \phi^* \phi}{c_1^2 v^2}\right) - \frac{4e_1(\varphi^* \partial_t \varphi + \varphi \partial_t \varphi^*)^2}{m^2 c_1^4 v^4} + \mathcal{O}\left(\frac{\varphi^4(\partial_t \varphi)^2}{m^2 v^6}\right), \qquad (8.1.10)$$

which should converge to the correct velocity in the small-a limit as $(ma)^4$.[4] The values of c_1 and d are in Table 5.1. For each plaquette pierced by a string, we average $\gamma^2 v^2$ over the plaquette's four corners, and use this average to determine v, γ. Finally, we interpolate the position within a plaquette where the string pierces it, by fixing to the gauge where each link is $\pm 1/4$ the value of the magnetic flux through the plaquette, and interpolating the φ_1 field to find its zero [110]. We construct strings as the series of straight segments connecting these interpolating points [110]. The overhead to identify and record strings is a small fraction of the numerical effort. We have compared the results using the other field φ_2 for string identification, and consistently find string length and mean velocity to agree within 1%. We also check the average distance between a point on the φ_2 string network and the nearest point on the φ_1 string network: for $q_1 = 4$ and $mt = 512$ we find an average distance of $0.065/m$. Therefore each scalar describes essentially the same string network; in particular our procedure for getting only $(1,1)$ type strings is successful.

---

[4]   There are other estimators, such as that used in [109], which may be less spacing-sensitive at the spacing we consider. It would be interesting to compare them systematically. One virtue of our choice is that $v < 1$ is manifest, since one computes $\gamma^2 v^2$ rather than v directly.

8.1.1   Test of the Methodology

In this section we will present string only results obtained on $2048 \times 2016 \times 2000$ lattices with relatively coarse spacing $ma = 1$. We compare the 2-scalar model at a few values of q_1 with the abelian-Higgs model on the one hand, and a scalar-only global model on the other. In each case we take $ma = 1.0$, except for the scalar-only model, which has thicker strings relative to the mass (c_1 of Eq. (5.3.20) is $c_1 = 0.412$) and which is therefore less sensitive to the mass value. Therefore for the scalar-only case we used $ma = 1.5$. We have not extrapolated to finer lattice spacing. Our preliminary study indicates that doing so will increase the network density by a few percent, and increase string velocities by closer to 10 percent. We intend to make a more complete study, including continuum extrapolation, in the future. Our main goals are to show that the numerics are relatively straightforward to conduct, and that many properties of the string networks evolve smoothly from their behavior in the global theory with low tension towards the behavior observed in local (abelian-Higgs) networks as the string tension is increased. But not all at the same rate; the string velocity shifts rather quickly, while the network density takes a much larger tension to become more abelian-Higgs-like. We intend to make a more comprehensive study in the future.

We will focus on the density of the string network, the mean string velocity, and how "kinky" the strings are. The general expectation is that the network should evolve towards a scaling solution, where the density of strings and other string properties scale with the system age (see for instance [111, 112]). We introduce the scaled network density ξ and mean inter-string distance L_{sep}, defined as

$$L_{\text{sep}}^{-2} \equiv V^{-1} \int_{\text{all string}} \gamma dl, \qquad \xi \equiv \frac{t^2}{(1 + k/2)^2 L^2}. \tag{8.1.11}$$

Here $\int \gamma dl$ is the invariant string length, V is the space volume and t the time, all in comoving conformal coordinates. The factor $(1 + k/2)^{-2}$ converts from conformal-time based to physical-time based normalization, which is common usage in some of the literature. Note that different authors define the string density in different ways, often with the same symbol. For instance, a recent study of abelian-Higgs networks[5] [109, 113] uses the symbol ξ to represent the quantity we call L_{sep}.

We will also consider the orientation autocorrelator of the string; defining $\vec{s}$ as the unit tangent vector of the string, this is defined as[6]

$$D(\Delta l) = \frac{\int_{\text{all string}} \vec{s}(l) \cdot \vec{s}(l + \Delta l) \, dl}{\int_{\text{all string}} dl}; \tag{8.1.12}$$

more details will be given in a future publication [110].

Our goal is to understand the scaling behavior of string networks, and how it depends on κ. In practice we will never precisely observe scaling, and in some cases we may be quite far away. Three effects can cause scaling violations at a finite time t;

1. Scaling occurs when the string core has negligible size compared to the inter-string spacing. Therefore it is difficult for the network to show good scaling at early times, before $mt \gg 1$.

2. The string tension does have a residual contribution from the Goldstone field, which increases as the string separation increases with time. Since the mean inter-string spacing is expected to grow linearly with time, we expect $\kappa(t) \simeq \kappa(t_0) + \ln(t/t_0)$.

---

[5]   Our abelian-Higgs simulations are generally in good agreement with this reference, but the reference is much more systematic, and achieves higher statistics and better extrapolation towards the continuum.

[6]   Note that we have used rest-frame string lengths without γ factors in this definition. This can be improved but we have not yet done so.

3. Initial conditions may start the network out as denser or thinner than the scaling form, and it takes time for the network to adjust.

The severity of the first problem should scale as $(mt)^{-1}$ and therefore becomes less severe as we achieve larger lattices which can be run to later times[7] (and if we can use coarser grids, $ma \sim 1$, which is why we use an improved action). But the severity of this problem also depends on how *kinky* the strings are – how many places the string has an abrupt discontinuity or rapid change in its tangent vector (a kink), and how "sharp" these kinks are. After all, such kinks can occur on much smaller scales than the inter-string spacing, and we expect that any kink structure on scales smaller than roughly the string thickness will be lost to heavy-mode radiation, which is unphysical from the viewpoint of the thin-string limit. Kinks should tend to dissipate through Goldstone mode radiation. Parametrically, because radiation involves πf_a^2 while the energy available is set by the tension $\pi \kappa f_a^2$, string features with length scale l should dissipate in time $t \sim l\kappa$. Therefore smaller-κ strings should lose their short-scale structure, and the necessary separation-to-core hierarchy should scale roughly linearly with κ. So larger-κ networks should demand larger lattices and later times before correct scaling sets in. In the abelian-Higgs limit, it is not obvious if *any* lattice spacing is sufficient to capture true scaling.

The second problem is most severe when the κ contribution from our abelian degrees of freedom is small; for larger q-values the abelian contribution overwhelms any small scale-dependence in the Goldstone contribution. Therefor this problem is mostly an issue for purely global simulations, and perhaps for $(q_1, q_2) = (2, 1)$.

The issue of initial conditions requires that, if we want to say with any confidence that we are close to scaling, we need to see a variety of network initial conditions, with different initial string densities, converge to a common string density. As stated above, we take as initial conditions that $A_i = 0$ and $\varphi_1 = v_1 e^{i\theta_1(x)}$, $\varphi_2 = v_2 e^{i\theta_1(x)}$ (same phase as φ_1) at time $t = 0$ – actually at time $t = a$ with a the lattice spacing. This choice leads however to a string network which starts out quite dilute compared to the scaling solution. Therefore we modify the evolution by setting $k = k_{\text{start}}$ until some time t_{start}. A large value of k_{start} represents strongly overdamped evolution, leading to slow string motion and a much denser starting network, without excessive fluctuations. By varying k_{start} and t_{start}, we can vary the early-time density of the string network.

Figure 8.1 shows how the network density varies with the string tension. For each type of network, we have run two groups of simulations, one which starts with a somewhat underdense network ($k_{\text{start}} = 20$ and $t_{\text{start}} = 40$) and one which starts with a somewhat overdense network ($k_{\text{start}} = 50$ and $t_{\text{start}} = 80$ except for the abelian-Higgs case, where we used $k_{\text{start}} = 80$ and $t_{\text{start}} = 100$). In every case the different densities converge towards each other with time. For the pure scalar simulations and the case with the smallest added tension, the curves become approximately flat, indicating good approach to scaling. For higher tensions and for the abelian Higgs case, the network density is still rising at the last time studied. Even in the cases where the network started overdense, the density reaches a minimum and then rises. Therefore we have no evidence that these cases have achieved scaling, and the true scaling network densities are presumably higher than the last value in the plot. However the good scaling for $(q_1, q_2) = (2, 1)$, and the expectation that the required mt value should grow linearly with κ, suggest that the other global strings considered may at least be nearing their scaling regimes.

While many authors consider only the length of "long" strings, neglecting short loops, our results are based on summing over all string lengths. However, in all of our simulations, small loops make up a relatively small fraction of the total string length; for each simulation type, we find that loops satisfying $\int \gamma\, dl < 2\pi L_{\text{sep}}$ make up less than 10% of the total string length. This is expected for global strings, since loops generally start small, frequently self-intersect, and radiate away power on a time scale at most κ larger than the string curvature-radius scale. The same is not true in the abelian Higgs model, where, at least in the small core-thickness limit, non-selfintersecting string loops should be persistent.

---

[7] We stop the evolution at $t = L/2$, L the box length, to ensure that the lattice's periodicity is invisible under causal dynamics.

For the abelian Higgs case, the network density and particularly the low abundance of string loops is consistent with previous field-theoretical findings [109, 113] but is in contrast to expectations from Nambu-Goto simulations [101, 114, 115]. The largest scale Nambu-Goto simulation, counting only long strings, finds[8] $\xi \simeq 11$ [115], about a factor of 2 larger than the value we find for the abelian Higgs model. This simulation also finds a large contribution from string loops. This difference probably arises because the Nambu-Goto simulations are sensitive to very short-scale phenomena which Abelian-Higgs field simulations cannot resolve, even with the largest field theoretical simulations to date [109]. For instance, the largest string loops found to be of relevance in [115] had invariant length $l < t/20$ with t the comoving system age. Since the loops are moving and noncircular, the curvature radius is at least another order of magnitude smaller. But if a string loop ever develops points with curvature radius comparable to the string core thickness, these points will strongly radiate massive modes, leading to loss of string length. Therefore the required scale hierarchy needed to study abelian-Higgs string networks is enormous. On the other hand, we emphasize that the same should not be true of global networks. Small global-string loops should radiate away their energy quickly, and long global strings should lose their short-scale structure, so the required hierarchy is not as severe. It appears that we see the scaling solution for $(q_1, q_2) = (2, 1)$ strings, so if $mt \propto \kappa$ then scaling should be fairly close at hand for the larger $\tilde{\kappa}$ values we study.
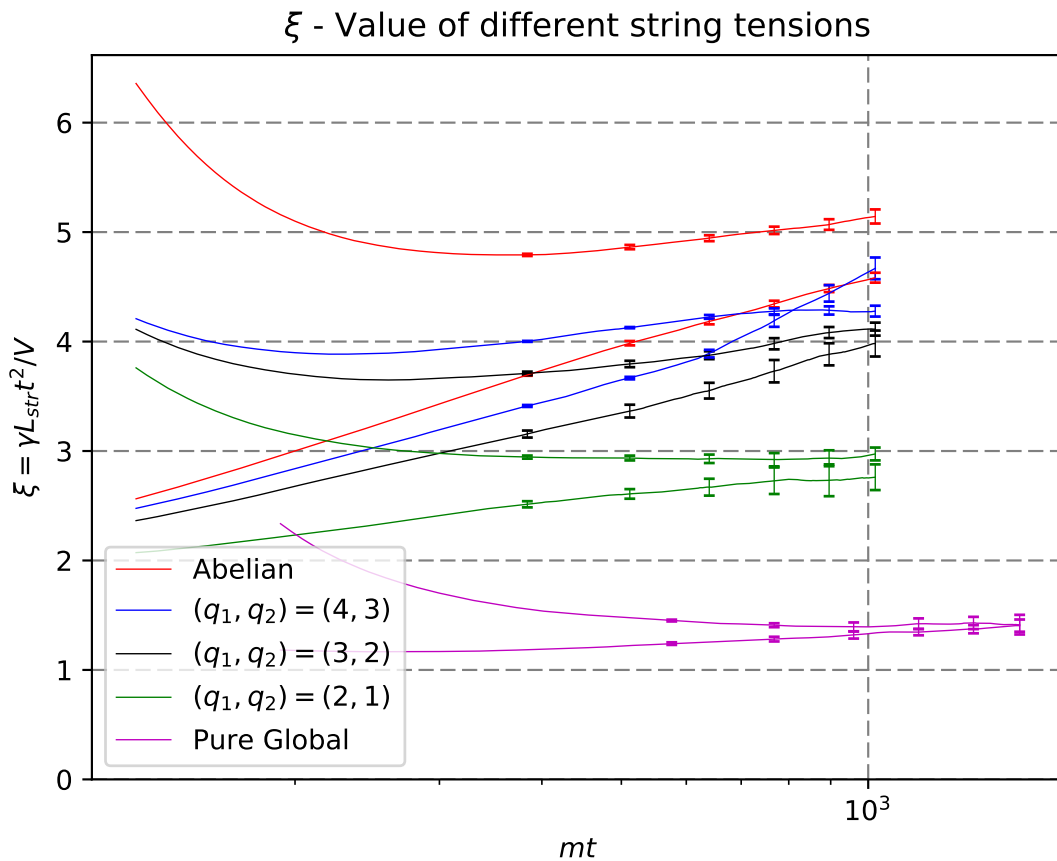

Figure 8.1.: Network density for different string tensions. The falling curves represent the overdense networks, while the rising curves represent the underdense networks.

---

[8] Their γ is our L_{sep}/t, and therefore $\xi = 1/(4\gamma^2)$ relates our and their notations. They find $\gamma = 0.15$ which becomes $\xi = 11$.
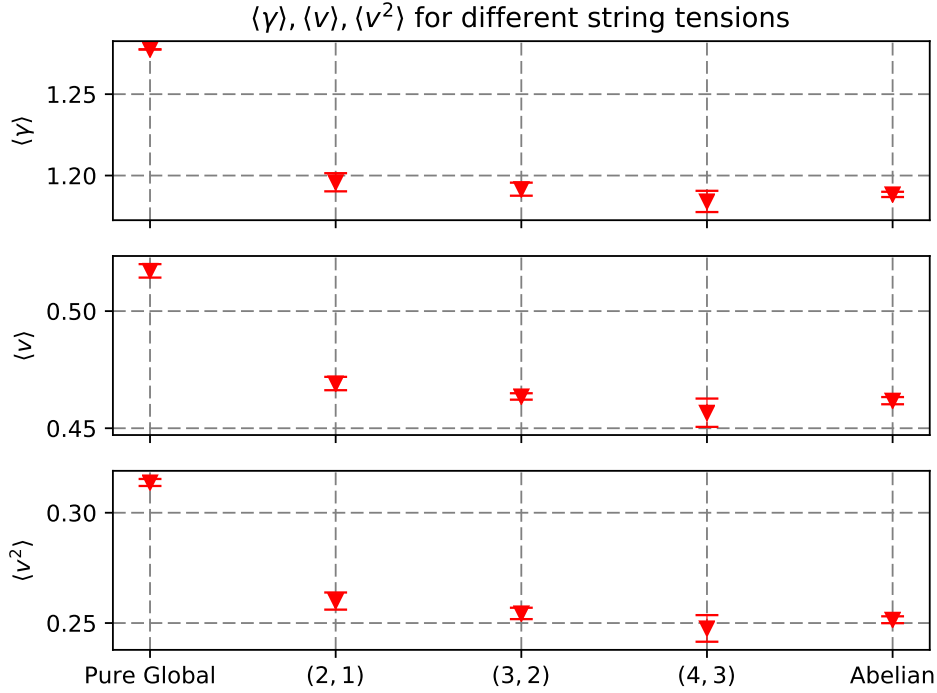
Figure 8.2.: Mean gamma factor , velocity and squared velocity. The upper and lower bar indicates the mean values for the overdense network (upper) and for the underdense network (lower).

Figure 8.2 shows the mean string velocity, squared velocity, and gamma factor, each defined as

$$
\left.\begin{array}{r}
\langle v \rangle \\
\langle v^2 \rangle \\
\langle \gamma \rangle
\end{array}\right\}
\equiv
\frac{\int \gamma \, dl \times \left\{\begin{array}{c} v \\ v^2 \\ \gamma \end{array}\right.}{\int \gamma \, dl} \, .
\tag{8.1.13}
$$

For the overdense network the mean values are always slightly higher than for the underdense network; the difference exceeds the statistical error in either measurement. Therefore, rather than statistical error bars, we have plotted the mean values of the overdense and underdense network for the latest time we achieved, $mt = 1024$. We stress that the velocity measurements are not extrapolated to the continuum (in the sense of small ma); preliminary indications are that all values will rise when we do so. However the qualitative feature, that the scalar-only theory has a higher velocity and that it then comes down rather quickly towards the abelian-Higgs value as the string tension is increased, appears to be robust.

Figure 8.3 shows the string-direction autocorrelator for each string type. The x-axis is a separation distance along a string, normalized by the system age. That is, an x-axis value of $\ell/t = 0.2$ means that we consider all pairs of points (x, y) separated along a string by $\int_x^y dl = 0.2t$. The y-axis is the dot product of their unit tangent vectors. We see that the strings with a larger coupling to Goldstone modes are systematically straighter (larger correlator) than the strings with smaller or no Goldstone coupling. The effect is especially clear at very small separation. A string with everywhere differentiable tangent vector would have vanishing slope at $\ell/t = 0$, while a string with perfectly sharp kinks would have a nonzero slope at $\ell/t = 0$ set by the density and angle of the kinks. This kinky behavior is consistent with the abelian-Higgs curve, but not with the scalar-only curve. Enhanced-tension strings lie in between, though closer to the abelian-Higgs case. We expect that the abelian-Higgs string and the highest-tension 2-field strings are not yet displaying their large-mt asymptotic behavior.
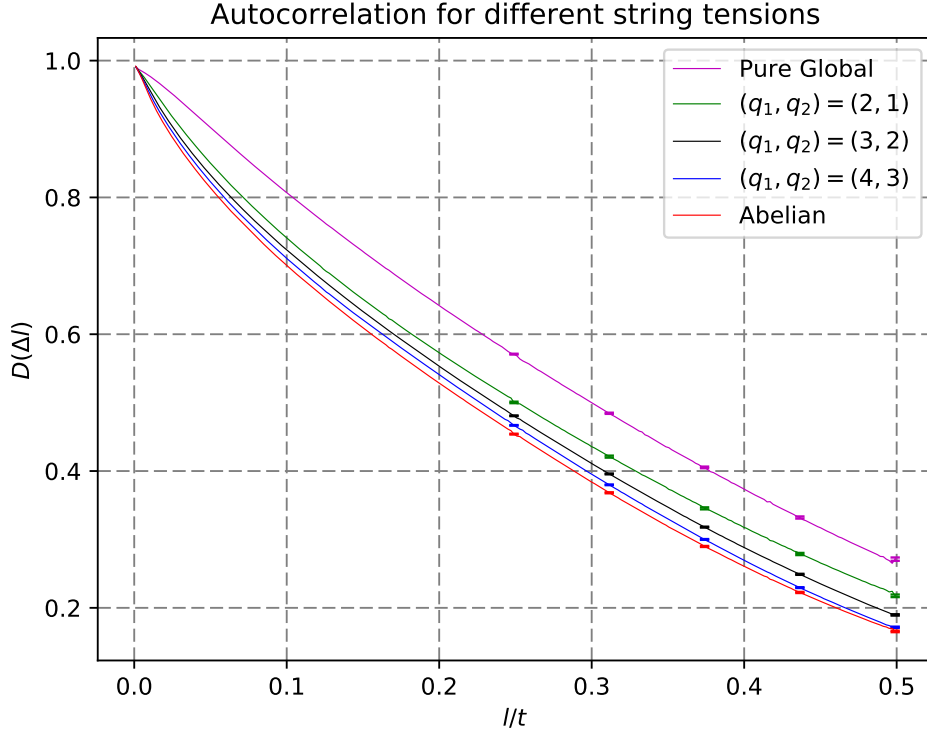
Figure 8.3.: Autocorrelation of the string-direction for different string tensions.

8.2 Axion Production

With the implementation introduced in the previous section, we will analyze in this section the dependencies of the axion mass. Afterwards, we will predict the axion's mass, given the following hypotheses:

1. the axion exists;

2. PQ symmetry is restored either during or at some point after inflation, so that the axion field starts out "random," meaning that its value at points out of post-inflationary causal contact are uncorrelated [116, 117];

3. The cosmological epoch where axions are produced – roughly, temperatures around 1 GeV – follows standard FRW behavior with the expected standard-model matter content;

4. the axion makes up 100% of the dark matter, so its current energy density is set by measurements of $\Omega_{\mathrm{dm}}h^2$; $\rho_{\mathrm{dm}}/s = 0.39$ eV with s the entropy density [118].

Our approach will be as follows. The Lagrangian for the axion field in a radiation dominated FRW universe, in comoving coordinates and conformal time, introduced in chapter 7, is

$$-\sqrt{g}\,\mathcal{L}_{\mathrm{conf}} = t^2\left(-\dot{\varphi}^*\dot{\varphi} + \nabla\varphi^*\cdot\nabla\varphi + t^2\frac{m^2}{8f_a^2}\left(2\varphi^*\varphi - f_a^2\right)^2 + t^2\chi(t)(1-\cos\theta_{\mathrm{a}})\right), \qquad (8.2.1)$$

where the metric is $g_{\mu\nu} = t^2\eta_{\mu\nu}$, the temperature is $T \propto t^{-1}$ and $\chi(T(t))$ is the topological susceptibility. Model calculations [119] and a recent lattice calculation [45] indicate that $\chi(T)$ is approximately power law between 1.5 GeV and 400 MeV, which, we will see, is wider than the relevant temperature range we need. Therefore we will treat $\chi(T)$ as a power law, $\chi(T) \propto T^{-n}$, so $t^2\chi(t) = f_a^2 t^{n+2}/t_*^{n+4}$, with t_* the natural scale where the susceptibility begins to influence the dynamics; $t_* m_{a,\mathrm{conf}}(t_*) = 1$ where

$m_{a,\text{conf}} = \sqrt{t^2\chi(t)}/f_a$ is the conformal-time axion mass. In terms of physical time, t_* is the moment when $m_a H = 1$. In the following we will suppress the subscript and write $m_{a,\text{conf}} = m_a$, except in the discussion. That is, masses and times will always be expressed in conformal units.

To initialize the network, we choose an independent random phase at every lattice site. We then evolve the fields for an initial time under strong damping ($\ddot{\varphi} + 2\dot{\varphi}/t \rightarrow \ddot{\varphi} + k_{\text{max}}\dot{\varphi}/t$ for times $t < t_{\text{start}}$) to prepare a string network relatively close to the scaling network density. The length and strength of damping is chosen such that the string network will roughly match on to the scaling network density; we will also study the dependence on the initial conditions below.

We evolve all fields until this dynamics is complete and there are no strings left. Then we count the axion abundance by extracting θ_a and $d\theta_a/dt$ from the simulation and applying the method of determined in section 3.5 to determine the axion content. This determines the total density of axions from all sources – we make no attempt to distinguish which axions arise from strings, from walls, or from misalignment, as we do not believe such a distinction can be made unambiguously. We express the axion number produced as a ratio to the angle-averaged misalignment value and we determine f_a such that the dark matter abundance is correct.[9]

The scale m for "radial" excitations in the φ field is may be as large as $m \sim f_a \sim 10^{11}$ GeV and must be at least 10^3 GeV (see Subsection 8.2.4), while the relevant length scale is H at the QCD epoch (around 1 GeV temperature), which is of order 10^{-18} GeV.

We handle this huge scale hierarchy with the introduced two-Higgs technique in section 5.3.

The outcome is that the string tension is maintained by some extra, massive degrees of freedom, but the mass scale m for these degrees of freedom must be resolved by the lattice, $ma \lesssim 1$ with a the lattice spacing.

The correct physical limit involves this scale becoming heavy compared to the physics of IR fluctuations in the axion field. Since the correct physical picture arises when m is large, we will hold ma fixed, that is, we keep m fixed in lattice units, throughout a simulation. In our implementation, the extra degrees of freedom introduce one new parameter q_1, which determines the value added to κ; most of our results are labeled $(q_1, q_2) = (4, 3)$, which means that κ has been increased by 50 through the added degrees of freedom [92].

In Appendix A we show that our results are in the large volume limit if we keep $L/t_* \geq 4$. We shall conservatively use 5. We also show that the axion number does not evolve after the string network is gone and can be measured as soon as no string is left, without concern that it will evolve further. Therefore box size and axion number measurement do not contribute to our error budget. Here we will instead focus on those effects which still do.

8.2.1 Lattice Spacing

For axionic strings to evolve correctly, the string core must be resolved by our lattice spacing. We need to check that our lattice is fine enough, in the sense of ma the product of the heavy scale and the lattice spacing is sufficiently small. That said, numerical cost scales as $(ma)^{-4}$ and required RAM scales as $(ma)^{-3}$, so we want the largest value which we can get away with. To test the (ma) dependence, we fix all other parameters in terms of m, and we consider axion production at various ma values in Figure 8.4. Because we have used an improved action, the result should naively converge in the small ma limit with corrections vanishing as $(ma)^4$, motivating the axis choice in the left-hand plot. However, the right-hand plot shows that the data fit better assuming $(ma)^2$ dependence. Indeed the χ^2 for an $(ma)^2$ fit is about 1, while for an $(ma)^4$ fit, $\chi^2 = 15$. Therefore we will assume that the errors are quadratic in spacing, despite our improved action. The fit indicates an upwards correction between $(ma) = 1$ and the continuum limit $(ma) = 0$ of $10 \pm 1\%$. In the rest of this study we will use $ma = 1$ and correct the final results upwards by 10%.

---

[9] We implement the misalignment case in the same code by turning off the scalar gradient terms. We also implemented misalignment in a simple dedicated code as a cross-check.
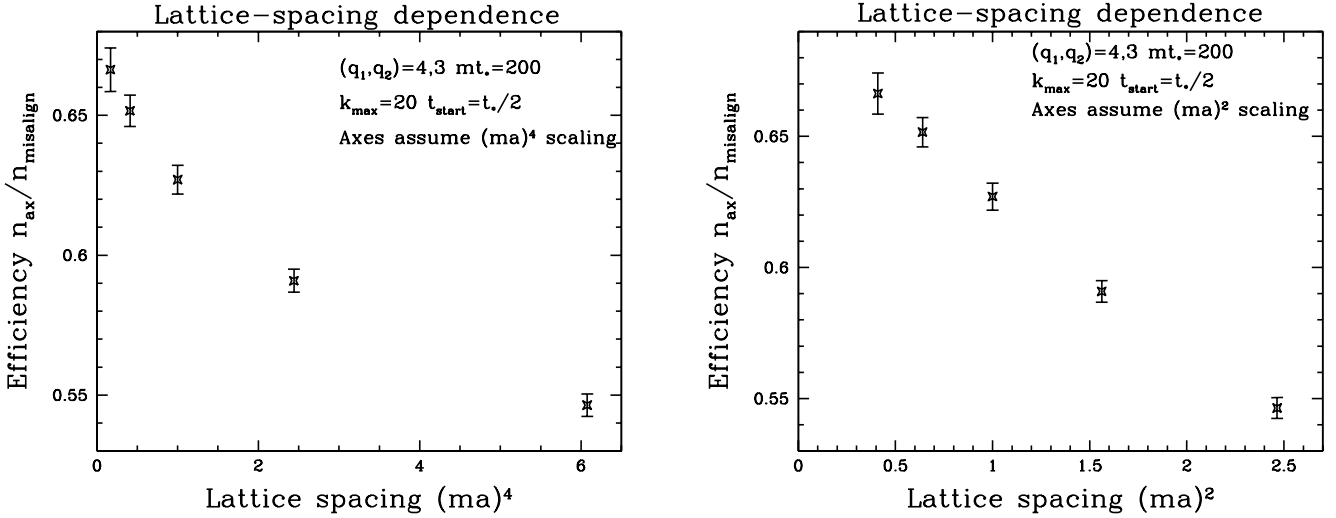
Figure 8.4.: Dependence of the axion production rate on the lattice spacing a, expressed as a function of ma with all else held fixed in units of m.

It remains to explain why the axion production scales with $(ma)^2$ despite our improved action, which should give $(ma)^4$ convergence if fields are smooth. We believe this occurs because a small fraction of string has a velocity close to 1, and therefore a large Lorentz contraction factor. If the (energy-weighted) fraction of string with velocity-squared $v^2 > v_0^2$ only vanishes linearly in the $v_0^2 \to 1$ limit, then the fraction of string with $\gamma^{-2} < \epsilon$ would then scale linearly in ϵ. Such scaling is consistent with our measured string velocity distribution.

It also makes sense from the string equations of motion, which are introduced chapter 6. In flat space, with $\chi = 0$, they read

$$\ddot{x}_i = x_i'' \tag{8.2.2}$$

which is solved by

$$x_i' = \frac{\alpha_i(\sigma+t) + \beta_i(\sigma-t)}{2}, \tag{8.2.3}$$

$$\dot{x}_i = \frac{\alpha_i(\sigma+t) - \beta_i(\sigma-t)}{2}, \tag{8.2.4}$$

$$\alpha_i(r)\alpha_i(r) = 1 = \beta_i(r)\beta_i(r) \quad \forall r. \tag{8.2.5}$$

Here α, β are backwards and forwards propagating waves, which in chapter 6 were introduced as a, b. To avoid confusion with the lattice spacing a we named them differently.

Even in curved space we may satisfy the gauge choice (6.1.7) instantaneously. The relevant question for the distribution of string velocities is the distribution of angles between α and β, since $v^2 = \dot{x}^2 = (1 - \alpha \cdot \beta)/2$. The *measure* of $\alpha \cdot \beta$ values is uniform in $[-1, 1]$ because α, β take values on the unit sphere. While we do not expect the distribution of $\alpha \cdot \beta$ values to be uniform in $[-1, 1]$, neither do we have a reason why it should avoid $\alpha \cdot \beta = -1$, so the probability distribution should not vanish at $\alpha \cdot \beta = -1$, and therefore the fraction of string with $\gamma^{-2} < \epsilon$ should indeed vanish linearly in small ϵ. Consider $\epsilon = (ma)^2$, corresponding to a gamma-factor of $\gamma > 1/ma$ and therefore a Lorentz contracted string thickness[10] of $\gamma^{-1}(1/m) < a$. Our hypothesis for string velocities then states that an $\mathcal{O}((ma)^2)$ fraction of string should be Lorentz contracted to a thickness of less than 1 lattice spacing. Such string is mistreated regardless of how improved our update algorithm is. Therefore, even if typical string is

---

[10] In this parametric argument we are neglecting order-1 factors which make the string somewhat thicker than $1/m$ and mean that, for $ma = 1$, *most* string is actually properly treated.
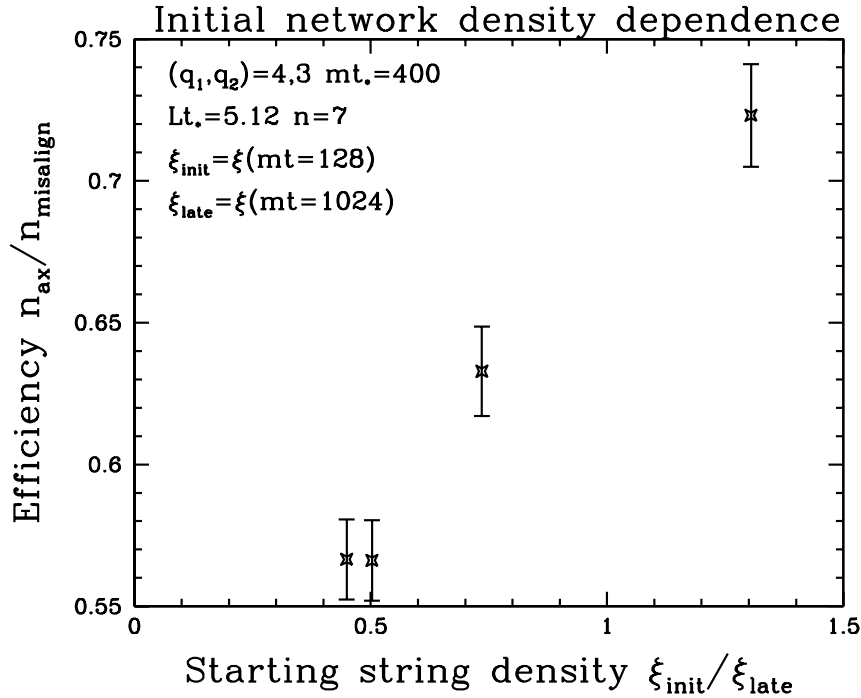
Figure 8.5.: Dependence of the final axion density on the initial string network density. We measure the starting network density as the ratio between the scaled density ξ at time $mt = 128$ ($t/t_* = 0.32$) and the scaled density at time $mt = 1024$, shortly before the walls start to influence the network evolution ($t/t_* = 2.56$).

treated correctly with $\mathcal{O}((ma)^4)$ errors, the fraction which is mistreated is of order $(ma)^2$. This allows $(ma)^2$ scaling corrections, regardless of the level of lattice action improvement.

8.2.2 Initial Network Density

We want the axion production from a string network which is initially in the scaling regime. But this cannot be exactly achieved; initial conditions will typically produce a network which is either denser or less dense than scaling. The network evolves towards scaling, and if mt_* is large enough then initial conditions should have little effect. But it would still be good to check how sensitive the final axion number is to the starting conditions.

We address this in Figure 8.5. We introduce the scaled network density

$$\xi = \frac{t^2 \int_{\text{all string}} \gamma dl}{4 V_{\text{space}}}, \tag{8.2.6}$$

with γ the local gamma-factor of the string so that the integral represents the total invariant length of string (length scaled by a γ factor to account for the energy content), and with V_{space} the volume of the simulation. This combination should approach a fixed "scaling" value as t increases (for $\chi(T) = 0$, that is, in the absence of potential tilt). We measure ξ once early in an evolution and again later in the evolution, just before the walls start to influence the string network evolution. We perform several evolutions with initial conditions with more or less damping, leading to denser or rarer initial networks. The ratio of the starting to final ξ, $\xi_{\text{init}}/\xi_{\text{late}}$, then indicates whether the network started too thin or too dense, and therefore from which side it is approaching the scaling solution. We find a roughly linear correlation between this starting density and axion production, with more axions arising from denser starting networks. However the dependence is quite weak. Based on the figure, we will try to use initial

conditions with this ξ ratio close to 1, and we will assign a 5% systematic error based on incomplete network scaling.

8.2.3 Thin-Core Limit

Next we must consider the effects of finite mt_*, meaning that the strings are of finite thickness. This is clearly an artifact because in the physical case there is a hierarchy of many orders of magnitude between string thickness and axion mass. We have incorporated the logarithmic sensitivity to this hierarchy by implementing auxiliary fields to give rise to the resulting high string tension. But there can still be effects suppressed by powers of $1/(mt_*)$, probably starting at first order. In particular, strings may lose energy via the radiation of unphysical massive modes. We only expect such radiation from short length-scale structures on the strings, which should generally get smoothed out by axion emission so long as $mt_* \gg \kappa$ and $m_a/m \ll 1$. However, because m_a grows as a large power of conformal time, $m_a \propto t^{1+\frac{n}{2}}$, the latter condition may not be maintained, given the persistence of high-tension strings. And if the axion mass m_a comes of order the heavy-mode mass m then one might expect that axion production is lost to heavy-mode production, and the simulation could result in an *under*estimate of axion production.[11]
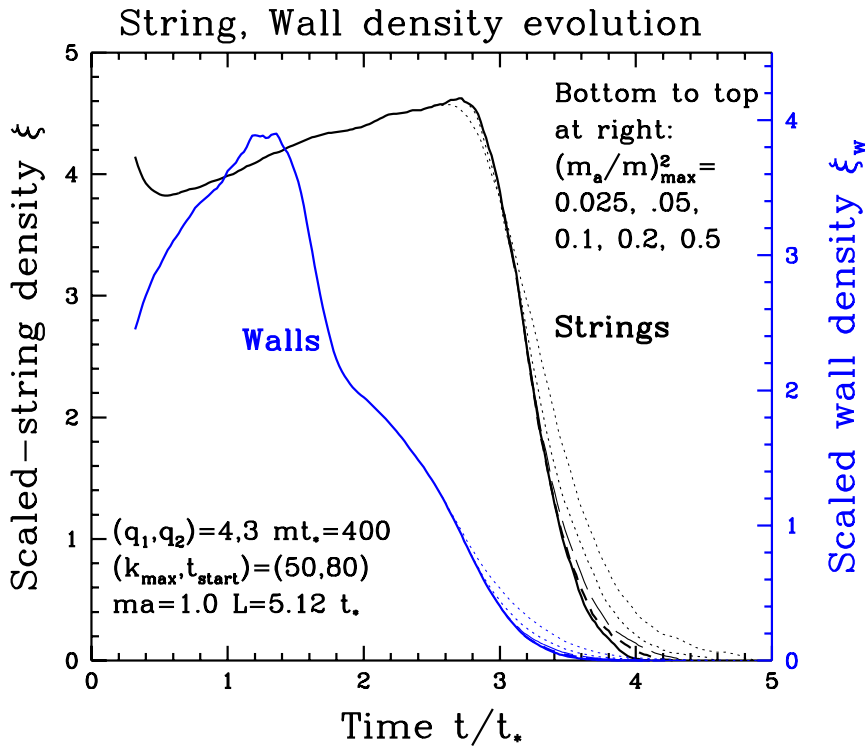

Figure 8.6.: Density of walls and of strings as a function of t/t_* when the axion mass is artificially limited with 5 different limits.

We can "fix" this problem by artificially capping the value of m_a, so that rather than growing with time at all times, $t^2\chi(t)$ grows up to some value and then becomes constant. But this replaces one unphysical behavior with another, and it will introduce new artifacts. The axionic wall tension is proportional to m_a. These walls cause the network to collapse, and limiting their tension artificially extends the life of

---

[11]   In [24] it was shown that, for a theory of a pure scalar field, the axionic domain walls spontaneously decompose as soon as $(m_a/m)^2 > 1/39$. The added degrees of freedom in our string cores prevent this physics from occurring; the domain walls remain strongly metastable up to and past $m_a/m = 1$.

the network. We show this effect in Figure 8.6. The figure shows how the total length of strings, rescaled as in Eq. (8.2.6), and a similar rescaled wall area (without γ factor or the conventional factor of 4),

$$\xi_{\text{wall}} \equiv \frac{t \int_{\text{all wall}} d^2\Sigma}{V_{\text{space}}}, \tag{8.2.7}$$

evolve with time under the influence of various choices for a maximal m_a/m value. We see that the wall area starts to decline as the wall surface tension turns on around $t = 1.6t_*$, and later around $t = 2.8t_*$ the surface tension becomes large enough to influence the string network evolution, drawing together the strings and collapsing the network by $t = 4t_*$. However, artificially limiting the axion mass slows down the collapse of the network; for the smallest value we considered, the last bits of string survive almost to $t = 5t_*$.

We also expect that the network with a maximal m_a/m value will produce more axions than without such a cutoff.[12] The reason is that, as m_a increases, the energy stored in the string network becomes less and less useful for producing axions. While increasing m_a increases the energy in axion fluctuations and in domain walls in proportion to m_a, it does not change the energy in strings. Therefore, as m_a increases, the capacity for strings to make axions is diluted; since making an axion costs energy m_a, an energy E can only produce E/m_a axions. Limiting m_a turns off this dilution, allowing the string energy to produce more axions, and could therefore result in *over*production of axions.
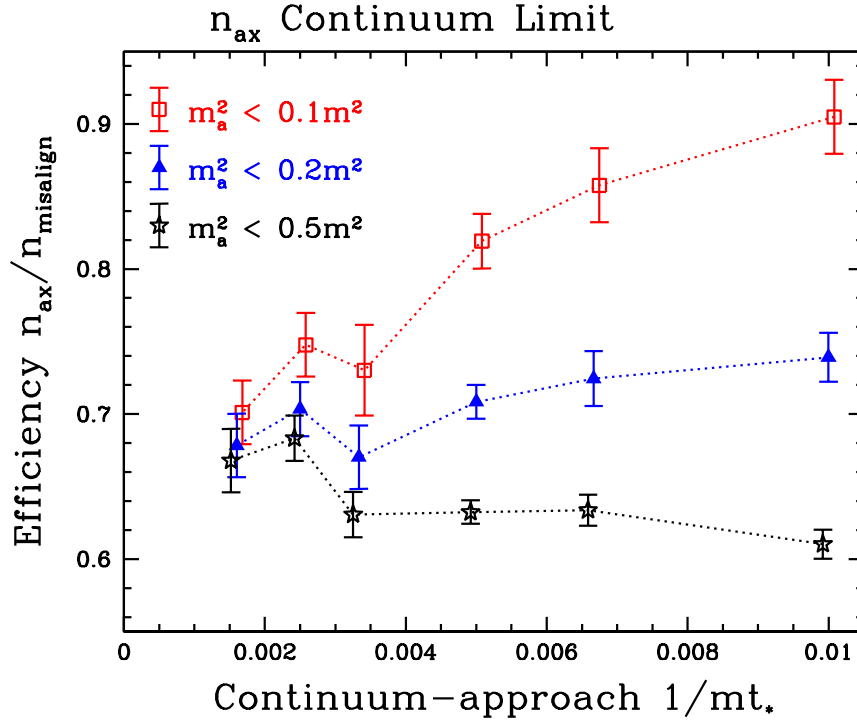

Figure 8.7.: Axion production as a function of the continuum limit $1/mt_* \to 0$ at three values of the artificial limiting value for the axion mass $(m_a/m)_{\text{max}}$.

The issue should disappear if we can reach a large enough value of mt_*. But it is useful to consider different cutoff values for m_a/m and take the large mt_* limit for each. If the continuum limits are the same, then it lends credence to the belief that we have achieved the continuum limit. According to Figure

---

[12] Something special happens if we choose a maximum value for m_a which is very close to $m/2$. In this case, there is a resonant nonlinear mode-coupling process which converts mass $m/2$ axions into mass-m excitations, leading to a reduction in the axion production for values of $(m_a/m)_{\text{max}}$ very close to 0.5. This effect is clearly an artifact, so we avoid this special value.

8.7, The difference between different cutoff choices falls below 10% starting around $mt_* = 300$ (third-from-leftmost points). On the two still-finer lattices, the choices $(m_a/m)^2_{max} = 0.5$ and $(m_a/m)^2_{max} = 0.2$ agree to within 3%. So these values can be close to the continuum limit. Note that the last point in the figure, with $mt_* = 625$, was achieved by loosening ma from $ma = 1.0$ to $ma = 1.25$ and using the result of Figure 8.4 to extrapolate it to the same value as the other points; it is also at a slightly smaller physical volume, $Lt_* = 4.1$ rather than 5.1.

The error bars shown in the figure are statistical only. However the statistical errors for points with the same mt_* value but different $(m_a/m)^2_{max}$ values are strongly correlated, since they are calculated from simulations which are identical up to the point when m_a reaches the smaller upper-bound value. Therefore the determination of the difference between different $(m_a/m)^2_{max}$ choices has smaller errors. In particular this difference is *not* linear in $1/mt_*$, but drops to a small value at a sufficient $m_{a,max}t_*$ value. That complicates the continuum limit. Here we will perform a linear extrapolation of the three smallest $1/mt_*$ data points, each for $(m_a/m)^2_{max} = 0.2$ and 0.5. We find 0.696(46) and 0.729(41) respectively. The fact that these answers are not the same indicates that our lattices are not yet abundantly fine. We assign a 10% error bar for the continuum-extrapolated value, to include these systematic issues, adopting $n_{ax}/n_{misalign} = 0.71(7)$. This is for $n = 7$, $\kappa = 50$ from extra degrees of freedom, and before performing the small ma extrapolation.

8.2.4 String Tension and Temperature-Dependent Susceptibility

Having discussed numerical artifacts, we now turn to actual physical parameters which are relevant but not completely known: the string tension κ and the strength of the temperature dependence n in $\chi(T) \propto T^{-n}$.
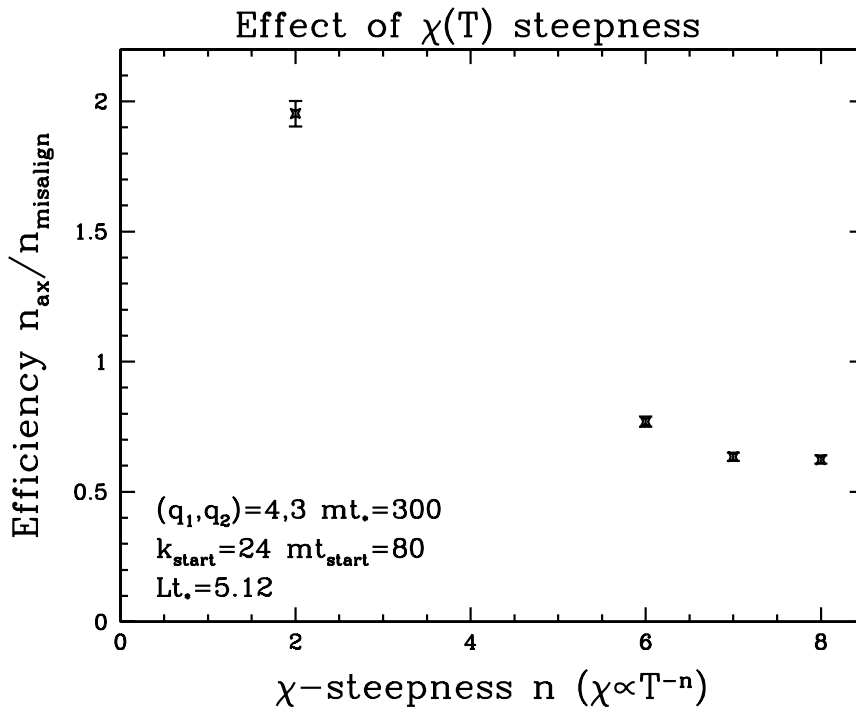

Figure 8.8.: Dependence of the relative axion production efficiency on the parameter n, controlling how quickly m_a rises with t. For small n (gradually rising m_a) the network produces more axions than in misalignment; for large n it produces fewer.

The slope n is calculable in lattice QCD. Recently Borsanyi *et al* have presented [45] results up to and beyond the relevant temperature range. Using their results at 600 and 1200 MeV, we estimate $n = 7.6 \pm 0.5$. Most groups find results which agree with Borsanyi *et al* at lower temperatures [84, 120–124],

although no group has reproduced these higher temperatures and even below 600 MeV there are some results which appear discrepant [125, 126]. Therefore we will explore other n values but consider values near $n = 7.5$ to be likely correct. We also feel that we gain some physical insight by considering different n values, especially much smaller values. We do this in Figure 8.8. The figure shows that small n values lead to more axions than in the misalignment mechanism, while large n values lead to less. But between $n = 7$ and $n = 8$ the dependence is not very strong. Therefore our choice to use $n = 7$ elsewhere, which we made mostly for simplicity, does not appear to be very critical.

We interpret the results of Figure 8.8 as follows. The larger the n-value, the more rapidly the axion mass m_a turns on, and therefore the heavier the axion is when the string network breaks up and loses its energy. That means that for small n, the network can still produce relatively many of the relatively-light axions, but for large n the axions quickly become heavy and the string energy cannot produce a large number of them. This is consistent with what we saw when $(m_a/m)^2_{max}$ was small. Indeed, the results at $n = 2$ had $(m_a/m)^2 = 0.07$ at the time the string network had completely disappeared, so walls broke up and axion production occurred when axions were still relatively light.

Finally we consider the κ value. Above we define κ as $\kappa = \ln(m/H)$. For us $H = 1/t$ the inverse system age. Therefore the contribution from axionic modes to κ is $\ln(mt)$, which we approximate to its value at $t = 3t_*$ since this is when the string network is breaking up. In addition there is a contribution from the extra massive degrees of freedom we have added, so our simulations have

$$\kappa = \ln(3mt_*) + 2(q_1^2 + q_2^2). \tag{8.2.8}$$

We do not know what the physical value of κ should be, because we don't know the model-dependent microscopic origin of the axion field. In the single complex-field case [127, 128] we don't know the radial mass m; if the axion is a composite or arises from more complicated physics [129], we do not know the compositeness scale and whether there is an extra contribution to the string tension from the microscopic physics giving rise to the axion field. We can reasonably guess that $m < f_a \simeq 2 \times 10^{11}$ GeV. Also the requirement that the radial excitations decay by the time the Universe reaches a temperature of 1 GeV, along with an estimate for their decay rate [130], $\Gamma_m \sim \frac{\alpha_s^2}{64\pi^3} \frac{m^3}{f_a^2}$, sets very roughly $m > 10^3$ GeV. These limits correspond to approximately $\kappa \in [48, 67]$. For $mt_* = 300$ and $q_1 = 4$ the κ value in the simulation is $50 + \ln(900) \approx 57$, which is in this range. By considering other values of (q_1, q_2), we achieve κ values larger and smaller than the physically interesting range.
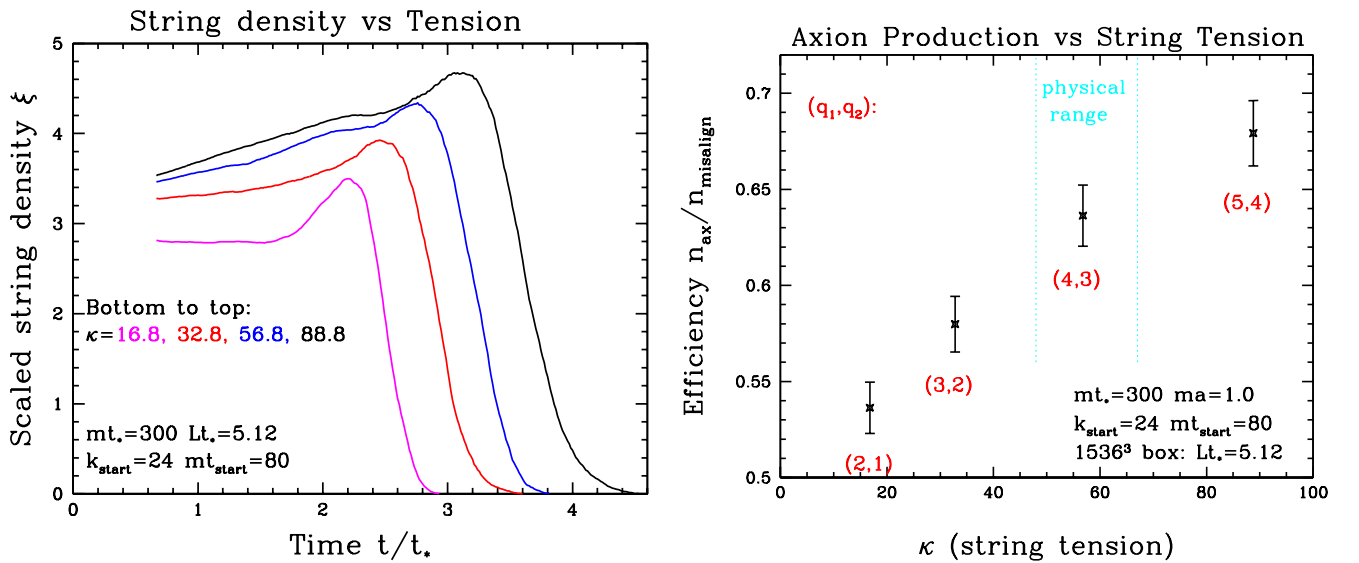

Figure 8.9.: Left: string density as a function of time for different κ values. The higher the string tension, the longer the strings persist. Right: axion production efficiency as a function of κ.

We show results for the axion production as a function of κ in Figure 8.9. The figure shows that higher tension strings give a significantly denser string network, with strings which break up later, but nevertheless produces only mildly more axions (note the false zero for the y-axis in the right plot). Therefore our ignorance of the physical value of m, κ is not very significant in bracketing the physical value of the axion. A simple linear fit to the left frame in Figure 8.9, and the range we quoted above for κ, gives a systematic error of $\pm3\%$ due to the unknown value of κ.

Note that the chosen initial conditions for both our n dependence and our κ dependence studies produced somewhat underdense networks. One can see in the left frame of Figure 8.9 that the underdensity is worse for the highest tensions, so the true κ dependence is somewhat *under*estimated. Also note that the larger κ values are farther from the large mt_* limit, leading to a slight *over*estimate in the produced axions due to $(m_a/m)^2_{\mathrm{max}}$ effects.

If we take the temperature dependence of the topological susceptibility to scale as $\chi(T) \propto T^{-n}$ with $n = 7.6$ in the relevant temperature range [45], and assume that axionic string cores arise at a mass scale $m \sim 10^7$ GeV so the extra string tension is $\kappa = 58 \pm 10$, then our results indicate an axion production efficiency which is 0.78(12) times as efficient as in the angle-averaged misalignment mechanism. The indicated error is dominated by the extrapolation to the large mt_* limit, with the uncertainty due to κ added linearly (not in quadrature).

8.2.5 Resulting Axion Mass

Now we use this result to calculate the axion mass. There has been relatively little entropy production since the Universe was 1 GeV in temperature, so the ratio of axion number-density to entropy density is approximately the same at the end of the axion-production epoch as it is now. We can express our results by saying that the axion number density, determined at $t = 4t_*$ or $T = T_*/4$ and then back-extrapolated to the temperature T_* where $m(T_*)H(T_*) = 1$, was

$$\text{back-extrapolated} \quad n_{\mathrm{ax}}(T = T_*) \simeq KH(T_*)f_a^2, \tag{8.2.9}$$

where a numerical evaluation finds that the angle-averaged misalignment value for K is $K = 16.61$, and our result is $K = 13.0 \pm 2.0$. By dividing this by the entropy density at that temperature, $s = 2g_*\pi^2 T_*^3/45$, we get the modern axion-number to entropy ratio, which can be multiplied by the vacuum axion mass $m_a = \sqrt{\chi(T = 0)}/f_a$ to give the modern dark matter density to entropy density ratio. We combine this with the Planck result [118],

$$\frac{n_b}{s} \simeq 8.59 \times 10^{-11},$$

$$\frac{\rho_{\mathrm{dm}}}{s} = \frac{\Omega_{\mathrm{dm}}h^2}{\Omega_b h^2}\frac{m_p n_b}{s} \simeq \frac{0.1194}{0.0221}(938\,\mathrm{MeV})(8.59 \times 10^{-11}) \simeq 0.39\,\mathrm{eV}, \tag{8.2.10}$$

thermal QCD results for the entropy density s and energy density ε of the thermal plasma from Borsanyi *et al* [45],

$$\varepsilon(T) = \frac{\pi^2 T^4 g_*}{30}, \quad s(T) = \frac{2\pi^2 T^3 g_*}{45}, \quad g_*(1\,\mathrm{GeV}) \simeq 73, \tag{8.2.11}$$

$$\chi(T) \simeq \left(\frac{1\,\mathrm{GeV}}{T}\right)^{7.6}(1.02(35) \times 10^{-11}\,\mathrm{GeV}^4), \tag{8.2.12}$$

Hubble's law $H^2 = 8\pi\varepsilon/(3m_{\rm pl}^2)$ with $m_{\rm pl} \simeq 1.22 \times 10^{19}$ GeV, the thermal value for the axion mass $m_a^2(T) = \chi(T)/f_a^2$, and vacuum value $\chi(T=0) = (0.076\,{\rm GeV})^4$ [58], to obtain

$$f_a = (2.21 \pm 0.29) \times 10^{11}\,{\rm GeV}, \tag{8.2.13}$$

$$m_a = 26.2 \pm 3.4\,\mu{\rm eV}, \tag{8.2.14}$$

$$T_* = 1.54 \pm 0.05\,{\rm GeV}. \tag{8.2.15}$$

Where in chapter 3.5 a more detailed derivation for the parameters f_a and T_* are shown. Taking the errors quoted in [45] at face value, the dominant error in f_a and hence in m_a is from our determination of K, while the error in T_* arises equally from the errors in K and in $\chi(T)$. Eq. (8.2.13), Eq. (8.2.14), and Eq. (8.2.15) constitute the main results of our study.

A more recent simulation with a different approach but also breaking PQ symmetry, after inflation, finds a similar result [131].

Our most striking result is that the axion production from random initial conditions, with the resulting dense and high-tension axionic string network, is actually *smaller* than the angle-averaged misalignment value. The deficit gets larger at large n, where the $\theta_{\rm a}$ potential tilts more abruptly; if it tilts more gradually then the axion production exceeds the misalignment value. Furthermore, although axion production is larger from high-tension strings than from strings with a lower tension, the dependence is quite weak; a factor of 10 increase in string tension between our results and the results of [24], along with the resulting factor of 3 increase in the string network density, has led to less than a 30% increase in axion production.

This clearly requires some explanation. The conventional wisdom has been (see for instance [43]) that axions are produced by misalignment in the space between walls, by walls, and by strings. Therefore the production is the sum of three terms, and must be larger than the misalignment contribution. We argue that this picture involves assumptions and commits double counting. It does not make sense to consider misalignment axions to be independent from walls. Within the misalignment mechanism, half of all axions emerge from the range of angles $|\theta_{\rm a}(t=0)| \in [2.76, \pi]$. But it is precisely the regions with $\theta_{\rm a} \sim \pi$ which become the domain walls. Much or most of the "misalignment" axion field energy becomes the domain walls; it is double counting to speak of both domain-wall axions and misalignment axions as independent contributions. Of course, since the axion field is initially very inhomogeneous, it is also not obvious that there are *any* spacetime regions where homogeneous misalignment is a useful description. Consider also what happens to the energy in domain walls. After the potential tilts and the domain walls become relatively thin and distinct, the wall surface tension induces forces on the strings. The walls lose their energy to accelerating the strings, which consumes the wall area (see Figure 8.6). Also in this epoch, it is not simple for walls or strings to emit axions. The axion frequency m_a increases with time, and any process involving time scales longer than m_a^{-1} has a frequency-mismatch problem to produce massive axions. That is, long wavelength fluctuations of walls or strings are incapable of producing axions because they drive the axion field at frequencies below m_a. This was seen very clearly in the previous study of 2+1D axion production with massive strings [25].

What about the energy of the string network? The high string tension means that the network stores much more energy. But after the time scale t_*, the energy in domain walls and in axionic fluctuations increases with the axion mass as $E \propto m_a \propto t^{1+\frac{n}{2}}$, while the string energy does not increase as m_a increases. Therefore the string network's ability to produce axions dilutes with time. The network only annihilates when the walls are able to influence string dynamics, which occurs when the wall energy is comparable to the string energy. That is, the strings only fragment when their energy is comparable to the energy that was present in the wall network which caused them to fragment. And there is still the question of how efficiently the resulting small loops turn their energy into axions.

To improve this analysis, we see a few directions which need to be pursued. First, we need simulations with more RAM, so that larger boxes, and therefore larger mt_* values, can be studied. We need to be more systematic in setting the initial network density and understanding the approach to network

scaling. It should be straightforward to reduce statistical and extrapolation errors to the few percent level, with the dedication of more computer power.

Also, we would like to investigate some of the late network evolution in more microscopic detail. The string network breaks up into loops which then annihilate in a way which somehow does not produce many axions. It should be possible to cut such loops out of a simulation and resolve them with a much finer lattice, which can then properly separate the m_a and m mass scales and follow the loop dynamics down to short scales. This could help explain why so few axions are produced (or determine whether our limited lattice spacing is causing a systematic neglect of some relevant but shorter-distance physics).

In the next chapter, we present two methods, which are capable to increase the string length-to-thickness ratio and therefore, we will investigate strings in more microscopic detail. These solutions are implemented for local strings, since it is not clear yet how to treat the fields outside the string core, for global or two-Higgs strings.

The first method is capable to cut a small loop out of a simulation, and resolve it with a much finer lattice, whereas the second solution uses the Nambu-Goto action to construct a string from the loop solution. We will explain both methods in the next chapter in greater detail.

Chapter 9

Local String Simulations

In this chapter we want to understand cosmic strings on a more fundamental level. However, understanding string dynamics is quite challenging, since it is hard to construct an initial string on a lattice. This is even more complex for global or the newly introduced two-Higgs strings, hence the strings have long range interactions which local strings do not have. However, it was shown, that global and local strings should behave quite similar [29]. Therefore our methods presented in this chapter are all developed for local U(1) strings.

The string dynamics gets investigated in this chapter by two different developed methods. The main goal is to have a single local $U(1)$ string which then can be evolved in a lattice. The first method which provides a solution for this problem cuts out a string from a running simulation and reevolves the string after refining the lattice. The second method gets more specific. Here we construct the string from the Nambu-Goto string solution, which allows us to directly compare the predicted equation of motion with the evolved motion of the string on the lattice.

In this section almost all results are done by lattice simulations. The radial and the Higgs mass are, to be in the Bogomol'nyi limit, $am_A = am_H$ and we also write am_A simply as m_A. Therefore, the string thickness, for example, directly scales with the lattice spacing.

9.1 Cut Single Strings

To study strings in microscopic detail, we first present a method, which extracts strings from a lattice at late times. After a string is cut, the periodic boundaries of the new lattice do not match anymore. Therefore we have to adjust the field values, that they are continues again. This is done with a relaxation algorithm. To increase the lattice we perform a so called lattice mesh refinement, which includes new lattice points but has the same string length-to-thickness ratio. Therefore we change the mass, which is equivalent of changing the thickness of the string. This is easier for local string systems since local strings have no remaining phase difference and therefore no string-string interaction.

9.1.1 Extract String from Box

In order to investigate string behavior in networks we need to pick a string in our simulation which can be reevolved. To find such a string, we have to construct constraints which the strings have to fulfill.

1. Length of the string l is within the range $l \in [l_{\min}, l_{\max}]$.

2. Shortest distance $d_{s1,s2}$ to the next string is $d_{s1,s2} \geq d_{\min}$.

3. The cube c_i which contains the string has no matching parts with other string cubes
   $c_i \cap c_j = \emptyset \qquad \forall j \neq i$.

4. The string crosses the boundary surface with an even number $n_{sc} \bmod 2 = 0$.

The minimum and maximum lengths are input parameters we have to choose at the beginning of the simulation. We are interested in strings which are small enough to collapse within a moderate time and are not too short, which would make them collapse almost immediately. In figure 9.1 the second and
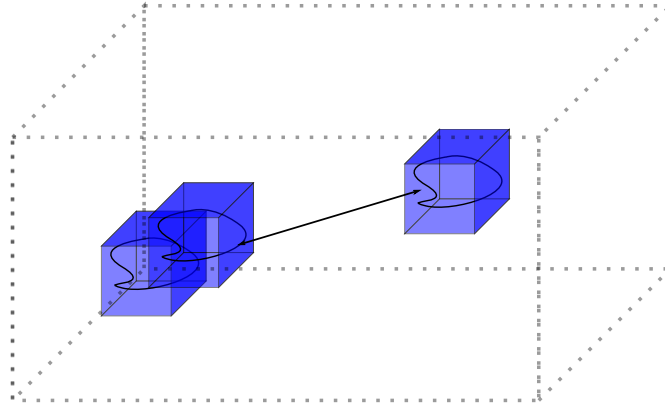
Figure 9.1.: Three strings on a lattice. The blue surface indicates the bounding box which incorporates the string. The shortest distance $d_{s1,s2}$ is symbolized by the arrow between the strings.

third point are schematically depicted. The distance between two strings is minimized to avoid false positive matches. Therefore we have to calculate all possible distances between two strings and take the shortest one. Note that we have continuous boundary conditions and therefore the distance between strings can be shorter across the boundary. The boxes placed in the pictures can be labeled as c_{s1}, c_{s2} and c_{s3}, where c_{s1} and c_{s2} are overlapping in their boundaries while the third one is a possible candidate for cutting. The boxes are created by taking the minimum and maximum values of the position of the string and extending them to a cube, which is also known as the bounding box. Cutting a string extends the minimum and maximum values by $\sqrt{3}l_{min}/2$, the square root of three is because of the three dimensional lattice and we only want to have half of the space between two strings cut. This ensures that the surface of the new box contains only non relevant physics.

| (a) | (b) |
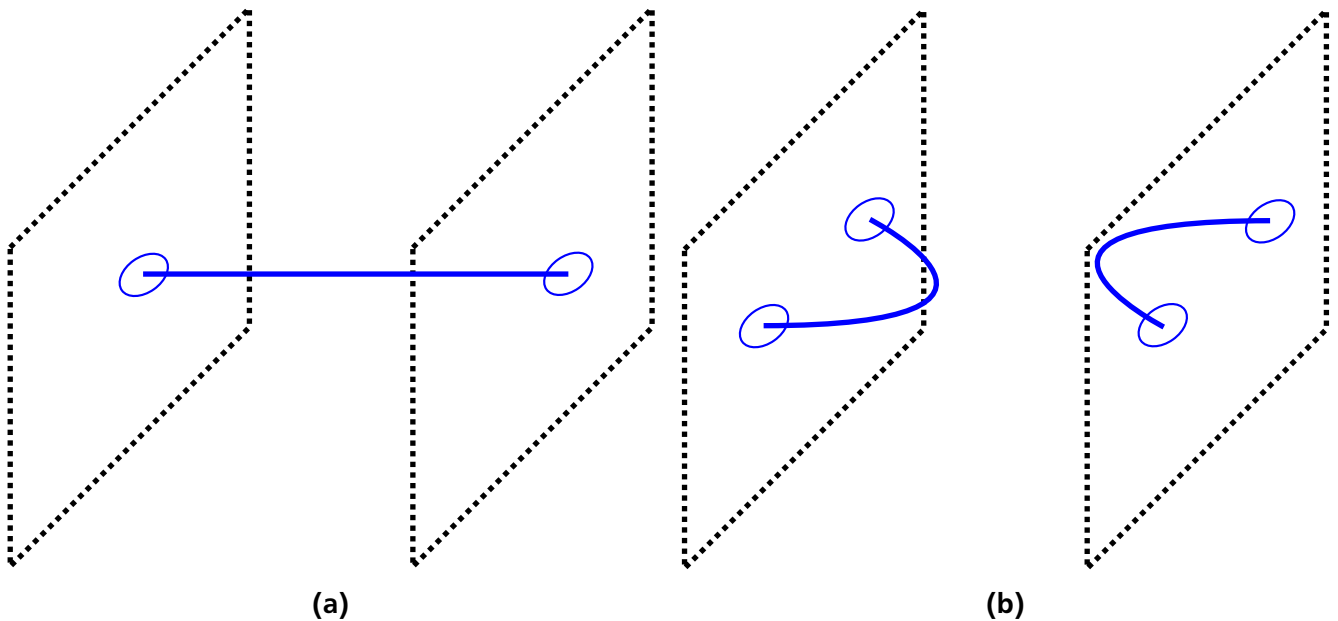
Figure 9.2.: **(a)**: A string which pierces each surface of the boundary once, therefore $n_{sc} \bmod 2 = 1$ for each surface. **(b)**: A string which pierces each surface of the boundary twice, therefore $n_{sc} \bmod 2 = 0$ for each surface.

Figure 9.2a and 9.2b explain the fourth constraint point in detail. The left depicts the case $n_{sc} \bmod 2 = 1$, while the right shows $n_{sc} \bmod 2 = 0$, because the amount of crossings n_{sc} is defined on each surface separately, therefore we have $n_{sc,left} = 1$ and $n_{sc,right} = 1$ for the left picture. If we took a string that does

not fulfill this condition we would have a string which would persist forever, since it cannot collapse. After we have found a string which fulfills all constraints, we have to fix the mismatch of the fields at the new boundaries of the box.

9.1.2 Relax Boundaries

Cutting a single string out of a running simulation leads to mismatches at the new boundary of the resulting string, consequently we have to fix the mismatch of the fields by relaxing the boundaries. To relax field configurations we desire to minimize the energy of fields in a specific region, this technique will be used in section 9.2 as well. The region where we have to fix our field values because of the discontinuity after cutting the box are the surfaces of the box. Accordingly, we only want to evolve the boundary of the box and the core, where the string is, should be frozen. For that reason, we turn off the time evolution in the whole box except one field point away from the boundary. Before the evolution starts we copy the E and $\dot{\phi}$ fields and set their values to 0. The A and ϕ fields will change and after evolution we will save the changes of these fields and take the copies of the E and $\dot{\phi}$ fields. There are two things we have to consider in evolving the fields.

First we also have to correct fields to impose with Gauss's law, which is violated after the string is cut. Gauss's law can be expressed by

$$\Phi = \int E d\mathrm{S} \propto Q \,, \tag{9.1.1}$$

$$Q = \int j^0 d^3x \,, \tag{9.1.2}$$

where Φ is the flux of the electric field E, Q the charge and j^0 the conserved current which is

$$j_A^0 = \partial_\mu F^{\mu\nu} = \nabla \mathrm{E} \,, \tag{9.1.3}$$
$$j_\phi^0 = \left(\dot{\phi}^* \phi - \dot{\phi} \phi^* \right) \,. \tag{9.1.4}$$

A Hamiltonian which preserves Gauss's law is

$$H_G = \int d^3x (j_A^0 - j_\phi^0)^2 = \int d^3x \left[\underbrace{\nabla \mathrm{E} - \left(\dot{\phi}^* \phi - \dot{\phi} \phi^* \right)}_{\Delta Q} \right]^2 = 0 \,, \tag{9.1.5}$$

where we have defined a new quantity $\Delta Q = \dot{\phi}^* \phi - \dot{\phi} \phi^*$. The equations of motion for the Hamiltonian are

$$\frac{\partial \dot{\phi}}{\partial \tau_F} = -\frac{\partial H_G}{\partial \dot{\phi}} \,, \tag{9.1.6}$$

$$\frac{\partial \dot{\phi}^*}{\partial \tau_F} = -\frac{\partial H_G}{\partial \dot{\phi}^*} \,, \tag{9.1.7}$$

$$\frac{\partial \nabla E}{\partial \tau_F} = -\frac{\partial H_G}{\partial \nabla E} \,, \tag{9.1.8}$$

where F denotes the The charge modifies the fields by

$$\dot{\phi}_r = \dot{\phi}_r(1 - \Delta Q \Delta t), \tag{9.1.9}$$
$$\dot{\phi}_i = \dot{\phi}_i(1 + \Delta Q \Delta t), \tag{9.1.10}$$
$$E_x = (Q_{i+\Delta x} - \Delta Q_i)\Delta t, \tag{9.1.11}$$
$$E_y = (Q_{i+\Delta y} - \Delta Q_i)\Delta t, \tag{9.1.12}$$
$$E_z = (Q_{i+\Delta z} - \Delta Q_i)\Delta t. \tag{9.1.13}$$

These equations are applied before the algorithm updates to the next time step, where we repeat this step until $H_G < 10^{-4}$. This will not change any physics for the string dynamics, since the equation of motion is invariant under these transformations.

Second, we damp the fields E and $\dot{\phi}$ at the boundary region to increase the speed of relaxation. The damping rules are

$$E \propto (1 - 0.05\Delta t)E, \tag{9.1.14}$$
$$\dot{\phi} \propto (1 - 0.05\Delta t)\dot{\phi}. \tag{9.1.15}$$

In figure 9.3 the relaxation energy over the log of the conformal time is plotted, the relaxation energy is defined as

$$E_{\text{relax}} = E_E^2 + |\dot{\phi}|^2. \tag{9.1.16}$$

The process stops when $E_{\text{relax,end}}/E_{\text{relax,init}} < 0.001$ and prints out the lattice configuration, we then evolve or refine the lattice. The refining approach is explained in the next section.
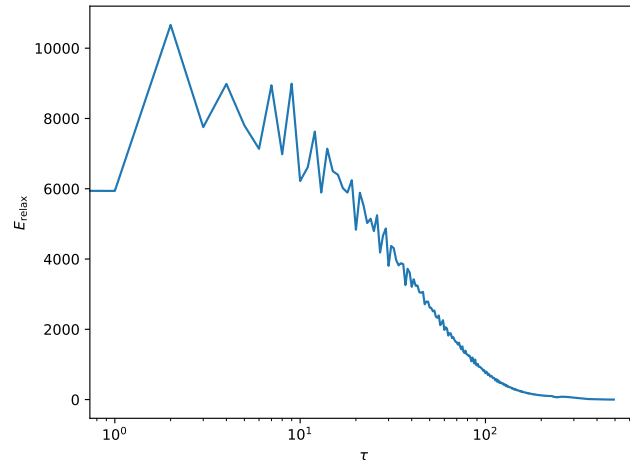
Figure 9.3.: The figure shows the relaxation energy dependency over conformal time during the relaxation process.

9.1.3 Refine the Lattice

We know that physical strings should have cores which are very much thinner than the string loop's length. And to eliminate all lattice spacing effects, the string core should also be many lattice spacings across. It is impossible to achieve both of these things without making our lattice spacing smaller. But once a small box has been cut out of a larger simulation, we actually have the computer memory

resources to do this. All we need to do is to develop a way to interpolate the field between the lattice points which we already have, a process called lattice mesh refinement. Therefore, we now discuss how to carry out such mesh refinement within the abelian Higgs model on the lattice.

The lattice refining procedure set new points and links next to the old one and therefore the new lattice has $(2n_x, 2n_y, 2n_z)$ points.
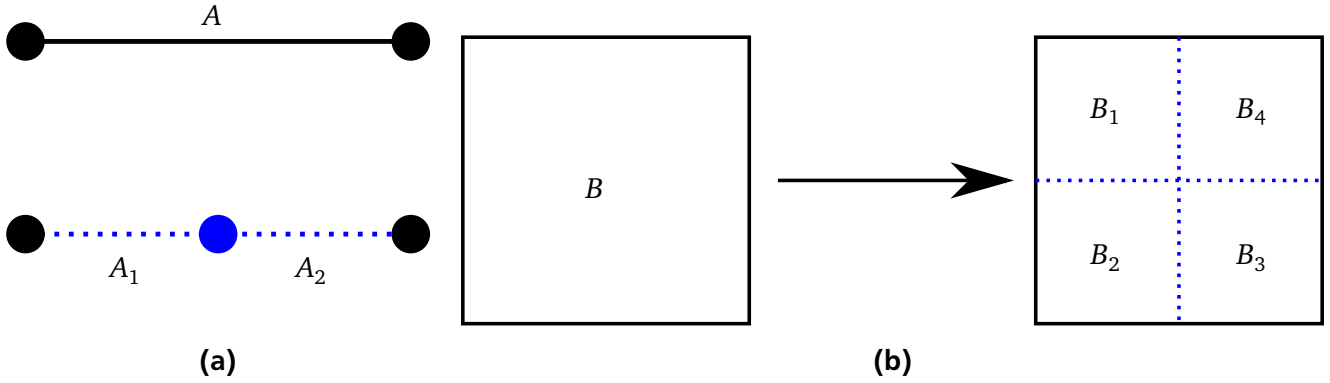

Figure 9.4.: (a): The link the gauge field is living on, is split into two new links. **(b)**: The magnetic field of the plaquette is equal to the sum of the magnetic fields for the new plaquettes after splitting the links.

In figure 9.4a the link is split up into two gauge fields which obey

$$A = A_1 + A_2,\tag{9.1.17}$$

or

$$U = U_1 U_2,\tag{9.1.18}$$

where $U = e^{iA}$. After refining the magnetic field of a plaquette, as shown in figure 9.4b, remains the same

$$B = B_1 + B_2 + B_3 + B_4.\tag{9.1.19}$$

For simplicity, we choose $U_1 = U_2 = \sqrt{U}$. The gauge fields are

$$\frac{A}{2} = A_1 = A_2.\tag{9.1.20}$$

The field at the new point can be obtained by parallel transporting the fields from both directions

$$\phi_2 = \frac{U(A_1)_{1\rightarrow 2}\phi_1 + \phi_3 U(A_2)_{3\rightarrow 2}}{2}.\tag{9.1.21}$$

Since we chose $A_1 = A_2$, we can express the equation by using only U. Inserting the complex field $\phi = \frac{\varphi_r + i\varphi_i}{\sqrt{2}}$, the total parallel transport is:

$$\varphi_{r,2} = \frac{U_r\left(\varphi_{r,1} + \varphi_{r,3}\right) + U_i\left(\varphi_{i,1} - \varphi_{i,3}\right)}{2}, \qquad (9.1.22)$$

$$\varphi_{i,2} = \frac{U_r\left(\varphi_{i,1} + \varphi_{i,3}\right) + U_i\left(-\varphi_{r,1} + \varphi_{r,3}\right)}{2}, \qquad (9.1.23)$$

where $U_r = \cos(A)$ and $U_i = \sin(A)$. The same rules apply to E and $\dot{\phi}$ fields as well, but these fields also pick up an additional factor of $1/2$ from the time contribution. The same run will take, after refining conclusively, twice the update steps to obtain the same results. The mass scales by $m_A = m_A/2$ and $m_H = m_H/2$.
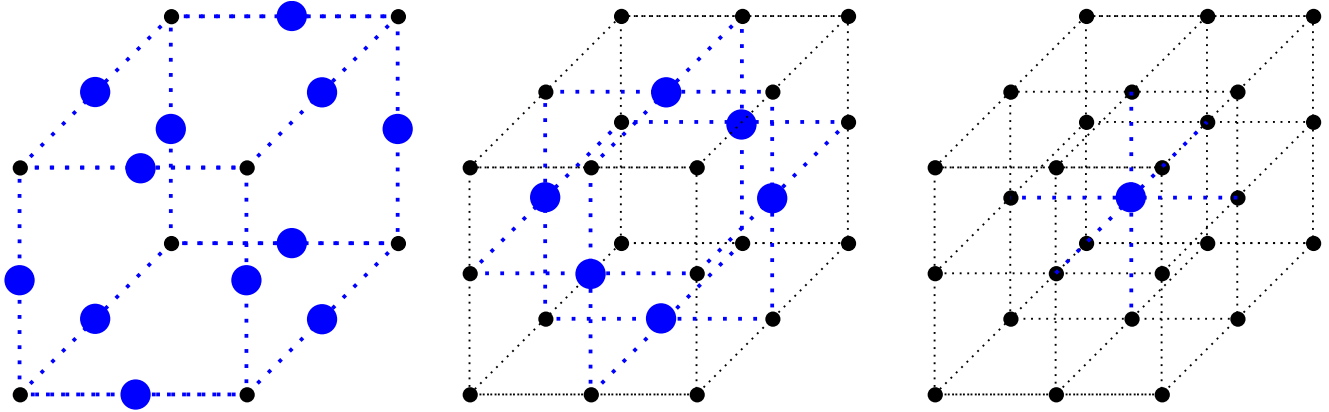
Figure 9.5.: The blue dashed line indicates the contribution of the fields (black) to the new fields (blue).

In an original box with 8 points, see on figure 9.5 the black points, we obtain after refining 19 additional points, which is exactly the statement above $2^3 \rightarrow (2+1)^3$. Before we start calculating the field points we first have to address all gauge fields. A New gauge field which, is parallel to a known old gauge field just take the half of the old value, see Eq. (9.1.20). For a new gauge field which do not lie in a known direction, we have to average over the next known gauge fields. Note that we do not need to respect order here. All fields getting generated have their origin from the same original fields. For generating the scalar fields we restrict to the order shown in the figures. For the fields on the surface we calculate the field from two directions and average over them. Applying these steps to the whole configuration, creates the configuration we finally want to investigate.

9.1.4 String Energy

Refining the lattice also affects the energy of the system. In section 5.2 we already introduced the string energy, where the energy-momentum tensor for equal masses was given by

$$T^{00} = \frac{E^2 + B^2}{2} + \dot{\phi}^2 + |\nabla\phi|^2 + V(\phi). \qquad (9.1.24)$$

The energy can be expressed as

$$\int T^{00} dx^3 = E_B + E_E + E_{\dot{\phi}} + E_{\nabla} + E_V, \qquad (9.1.25)$$

where E_B is the magnetic-, E_E the electric-, $E_{\dot{\phi}}$ the kinetic-, E_{∇} the gradient and E_V the potential energy. If the string is at rest, the energy reduces to

$$\int T^{00} d^3 x = E_B + E_{\nabla} + E_V . \tag{9.1.26}$$

Boosting this equation yields to

$$\int \Lambda_0^{\ \mu} T_{\mu\nu} \Lambda_0^{\ \nu} \frac{dx^3}{\gamma} = E_B' + E_E' + E_V' + E_{\nabla}' + E_{\text{kin}}' . \tag{9.1.27}$$

The dependence of the energies are

$$E_B' = \gamma E_B , \tag{9.1.28}$$
$$E_E' = \gamma v^2 E_B , \tag{9.1.29}$$
$$E_V' = \frac{1}{\gamma} E_V = \gamma \left(1 - v^2\right) E_V , \tag{9.1.30}$$
$$E_{\nabla}' = \gamma E_{\nabla} , \tag{9.1.31}$$
$$E_{\text{kin}}' = -\gamma v^2 E_{\nabla} , \tag{9.1.32}$$
$$E_{\text{tot}}' = \gamma E_{\text{tot}} . \tag{9.1.33}$$

Measuring the energy on the lattice gives us also a contribution outside the string core. We implemented a threshold, where only $|\phi|^2 < 0.81$ contribute to the string energy, since the field in the center of a string is $|\phi| = 0$ and outside the string $|\phi| = 1$. Numerically we can test these quantities by performing a time evolution with very high damping, which leads to $\gamma \approx 1$. The contribution of the energy at rest is

$$E_B \approx 0.2 E_{\text{tot}} , \tag{9.1.34}$$
$$E_V \approx 0.2 E_{\text{tot}} , \tag{9.1.35}$$
$$E_{\nabla} \approx 0.6 E_{\text{tot}} . \tag{9.1.36}$$

After refining, the total energy is

$$E_{\text{tot},n} \approx 2^n E_{\text{tot},0} , \tag{9.1.37}$$

where n is the number of refining steps.

9.1.5 Change of the Mass Adiabatically

After refining the string, the physical behavior is almost the same as for the unrefined case. Therefore the string thickness in the refined lattice also increases by a factor of two which can be seen from the string core size

$$\delta_{n+1} = \frac{1}{m_{n+1}} = \frac{2}{m_n} , \tag{9.1.38}$$

where n is the refining parameter. The mass we consider to change stays m_H and m_A as we are in the Bogomol'nyi limit with $\beta = 1$, therefore we just write m instead of m_H and m_A. Our goal is to change the mass after refining to the original value we had before refining. Changing the mass during evolution
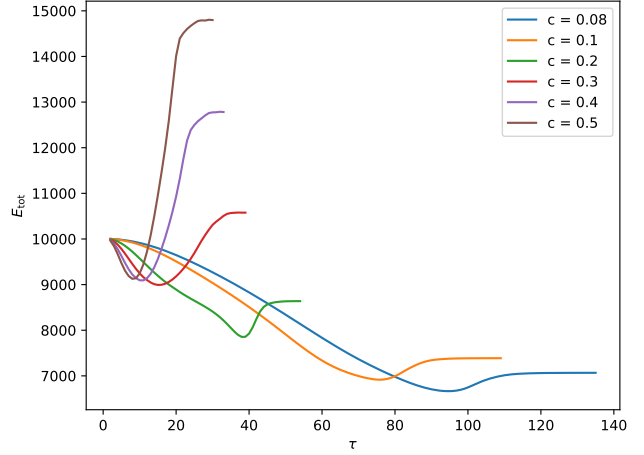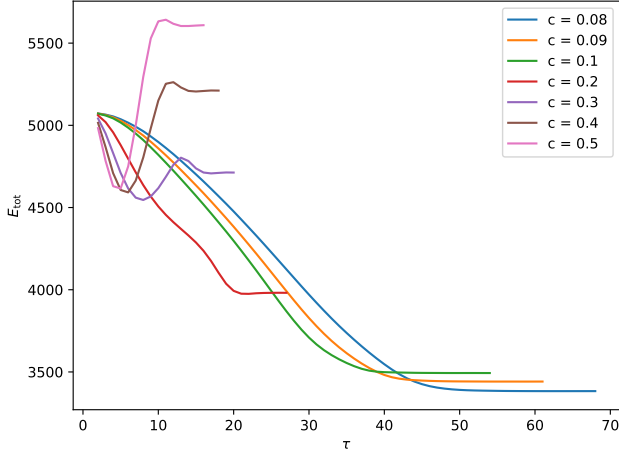
(a) Mass change from $m = 0.25$ to $m = 1$ by varying different c

(b) Mass change from $m = 0.125$ to $m = 1$ by varying different c

Figure 9.6.: For both figures the energy E_{tot} is over conformal time τ displayed.

can lead to drastic misbehavior, for this reason the change of the mass has to be adiabatic and we have to fulfill the condition

$$\frac{\mathrm{d}m}{\mathrm{d}t} \ll m^2 \,, \tag{9.1.39}$$

with the current mass m. Discretized on a lattice we get

$$\Delta m \ll m_t^2 \Delta t \,, \tag{9.1.40}$$
$$\Delta m = c \cdot m_t^2 \Delta t \,. \tag{9.1.41}$$

where $c \ll 1$.

In figure 9.6 we tested different parameters for c at different initial values m_{t_0}. We see for $c = 0.1$ the energy only changes a little and it seems that the energy starts reaching a minimum there. Therefore we will set $c = 0.1$ since it still changes the mass as fast as possible. We also see that the energy falls below the initial value, which is caused by the field fluctuations outside the string core, which are not equally sensitive to the mass change. The update of the mass during a time step is

$$m_{t+1} = m_t + h(m_t), h(m_t) = c \cdot m_t^2 \Delta t \,. \tag{9.1.42}$$

This expression gives us the maximum change of the mass during a time step. Since this function does not provide a gradual change from m_0 to m_{t*}, we have to construct a function which satisfies

$$f(m_t) \le h(m_t) \qquad m_t \in [m_0, m_{t*}] \,, \tag{9.1.43}$$
$$f(m_0) = f(m_{t*}) = 0 \,. \tag{9.1.44}$$

Such a function is

$$f(m_t) = -a \sin\left[\left(\left(\frac{m_t - m_0}{m_{t*} - m_0}\right)^m + 1\right)\pi\right]\Delta t - b \sin\left[\left(\left(\frac{m_t - m_0}{m_{t*} - m_0}\right)^n + 1\right)\pi\right]\Delta t \,, \tag{9.1.45}$$
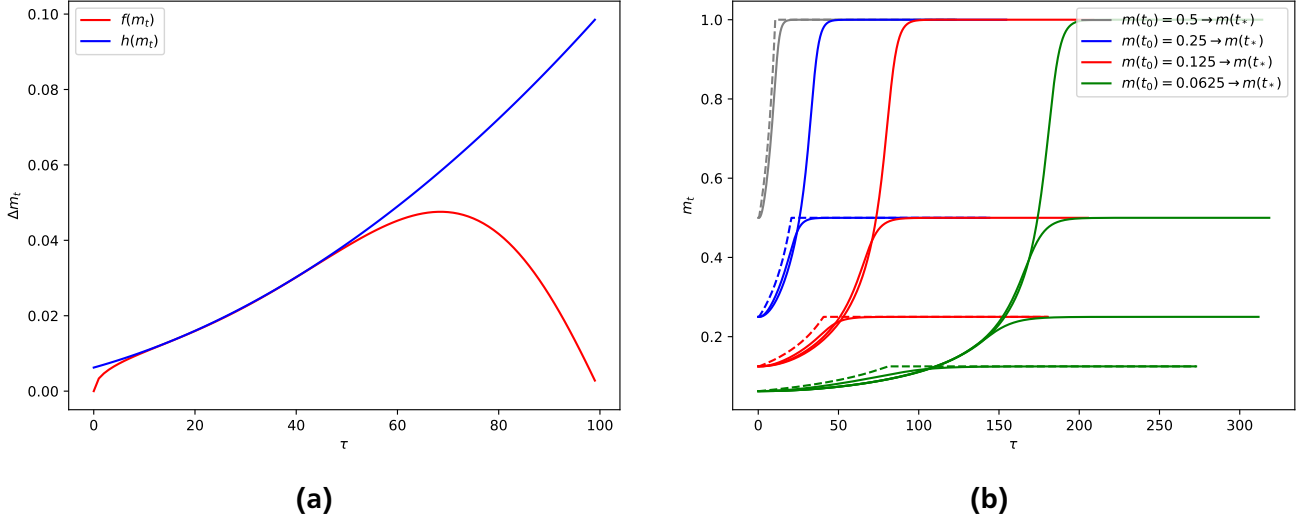
Figure 9.7.: In figure 9.7a, the comparison between $f(m_t)$ and $h(m_t)$ is shown, where $m_0 = 0.125$. The different mass changes by initial conditions taken from table 9.1 are depicted in the right figure 9.7b. The dashed lines indicates the mass change with $h(m_t)$, while the solid lines represent the gradual mass change with $f(m_t)$.

where a and b are parameters which need to too be adapted for different m_0 and m_{t*}, we fix $m = 2$ and $n = \frac{1}{2}$, which turned out to be a good choice. To get the ideal parameters we require

$$f(m_t) \leq \frac{h(m_{t*}) - h(m_0)}{3}, \tag{9.1.46}$$

$$\min \int_{m_0}^{m_{t*}} [f(m_t) - h(m_t)] \, dm_t = 0. \tag{9.1.47}$$

The best fit parameters can be seen in Table 9.1, where we constrained the parameters to be $a > 0$ and $b > 0$. For our first step we need an initial change, since $m_{t+1} = m_t + f(m_t) = m_t$. To have a gradual

Table 9.1.: Ideal parameter for a and b at specific initial conditions.

m_0	m_{t*}	a	b
0.0625	0.125	5×10^{-4}	5×10^{-4}
	0.25	2.7×10^{-3}	6×10^{-4}
	0.5	9.9×10^{-3}	9×10^{-4}
	1	3.72×10^{-2}	1.3×10^{-3}
0.125	0.25	2.7×10^{-3}	1.9×10^{-3}
	05	1.05×10^{-2}	2.7×10^{-3}
	1	3.96×10^{-2}	3.8×10^{-3}
0.25	0.5	1.0×10^{-2}	7.8×10^{-3}
	1	4.22×10^{-2}	1.08×10^{-2}
0.5	1	4.03×10^{-2}	3.12×10^{-2}

change, we use

$$2f(m_0 + c) - \xi \leq f(m_0 + f(m_0 + c)), \tag{9.1.48}$$

where $\xi = 0.001 \cdot h(m_0)$. This ensures a gradual increasing change of mass. If $m_t \geq m_{t*}$ we keep m_{t*} fixed and turn off the mass change. For small m_0 the function $h(m_t)$ rises slowly, which is why we need the additional factor in $f(m_t)$. This ensure, that at $m_t \approx m_0$ the function rises fast to its maximal value. In figure 9.7b, different changes of the mass are shown. We compare all possible changes in the same physical limit, therefore the system which is refined once with mass m_1 should behave the same as the system which is refined twice with a mass adaption from $m_2 \to m_1$.

9.1.6 Results of Cut Strings

We now investigate the microscopic behavior of strings, using the methods of mesh refinement and of mass and string core-size modification which we have just developed. Our goal is to see whether the expected large lifetime for string loops emerges when we make the string loops thin and achieve a fine lattice spacing. To cut strings from the lattice it is a bit challenging. However, we have cut 36 local cosmic strings from 100 different cubic lattices with length $n_x = n_y = n_z = 512$ and $m_A = m_H = 1$. We will treat the mass always the same why we only mention m_A in the following, but m_H is treated equally in this discussion. The length of the strings are in $l \in [50, 400]$, where the minimal distance between two strings is $d_{\min} \geq 20$ and the distance to a different string-box is $d_c \geq 10$. The 36 strings get refined by a power of two $a \to 2^{-n}a$, so $n = 0$ represents the original (unrefined) spacing and $n = 3$ makes the lattice a factor of 8 finer. The lattice spacing and the mass are, as discussed in chapter 7, implemented as am_H, we only mention the mass itself which includes the lattice spacing. For the first string set, we have $n \in [0, 3]$, which leads to corresponding masses $m_{A,n} = m_{A,0}/2^n$. This set is evolved without mass changing and with mass changing. For the case of mass changing, we also change only to intermediate values, which is $m_{A,n} \to m_{A,n-i}$, where $i \in [1, n]$. For the case of $n = 2$ we cut the string again out of the box after changing the mass to $m_{A,0}$ with the same parameters as described above. This procedure is repeated twice to investigate the increase of the lifetime of the loop. After every refining step, the conformal time also changes by the factor $\tau_n = \tau_0/2^n$, which needs to be respected when comparing the results. In table 9.2 the refining steps and mass changing steps are schematically displayed.

Table 9.2.: Three string cuttings separated by the vertical line and up to three refining steps. The mass change for $m_{A,n}$ is done for all intermediate steps from bottom to top.

n	0	1	2	3	2	4	4	6
$m_{A,n}$	1	1	1	1	1	1	1	1
		0.5	0.5	0.5				
			0.25	0.25		0.25		0.25
				0.125				

The lattice refinement slightly shifts the energy, as we see in figure 9.8. For $\Delta E_1/E_0 = -0.16 \pm 0.03$, $\Delta E_2/E_0 = -0.20 \pm 0.04$ and $\Delta E_3/E_0 = -0.21 \pm 0.05$. The total energy is conserved during the evolution, which is equal to a flat spacetime. The gap between the different refined and unrefined energies can be explained by the magnetic energy which is due to the relation we introduced in the previous section $B_0^2 \geq B_n^2$. This effect has a decreasing contribution after every refining step, which we can see quite well in the plots. In figure 9.9 we see the same evaluation with mass changing. We see the expected decreasing of energy at the beginning of the evolution, where it gets constant after reaching the final mass $m_{A,\text{final}}$. In figure 9.9 we compare $n = 1$ with $m_A = 0.5 \to 1$ by $n = 2$ with $m_A = 0.25 \to 05$. The same with $n = 2$ to $n = 3$ and the last data point is $n = 2$ with $m_A = 0.25 \to 1$ and $n = 3$ with $m_A = 0.125 \to 0.5$. The reduction of the energy is much less as in the previous plot since we compare these results with already refined lattices.

If we consider the string length compared to the conformal time, we expect that the string behaves roughly equal if we only refine the string without mass changing. In figure 9.10a we see an example string, which is refined three times. It is quite well seen, that the length increases at the beginning
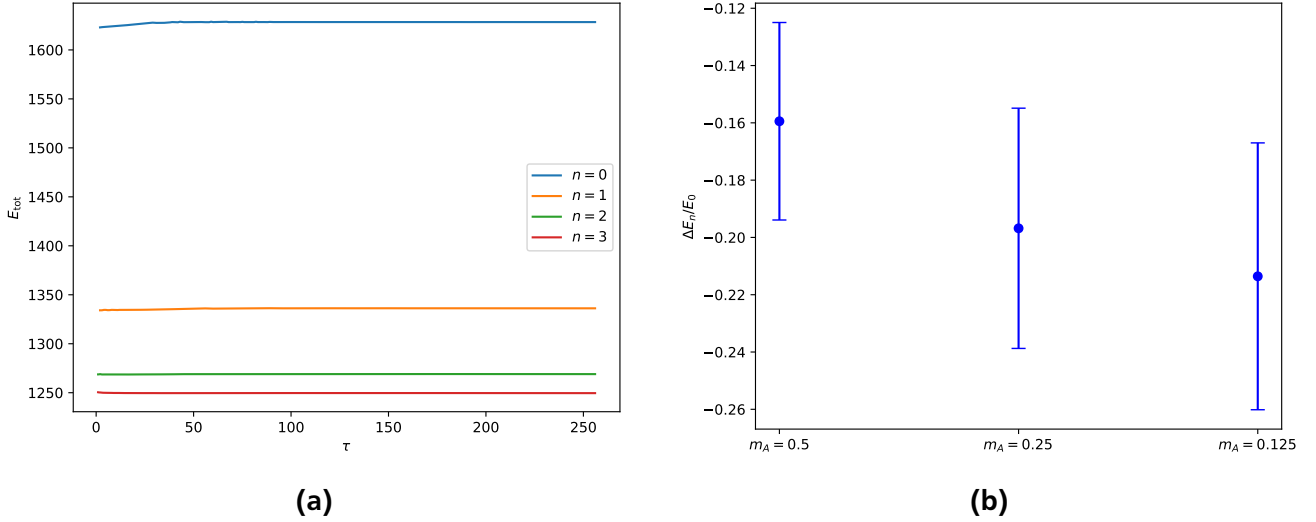
Figure 9.8.: (a): A string's total lattice energy contribution E_{tot} after refining without mass changing. (b): the relative difference of the energy averaged over all 36 strings.
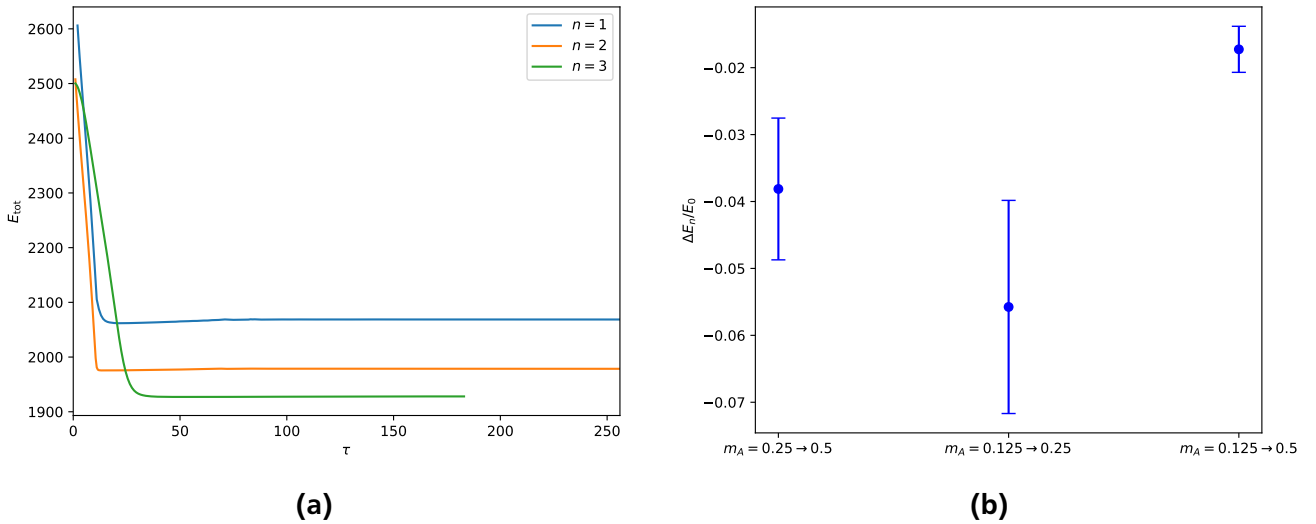

Figure 9.9.: In 9.9a is a schematic picture for a string with its total lattice energy contribution E_{tot} after refining with mass changing. In 9.9b is the relative difference of the energy for all 36 strings shown.

after refining, but the lifetime seems to be the same. Also the behavior of the string seems to stay the same, since it has the same length dynamics as the original string. The length difference of the original string and the refined string results from the lattice spacing which scales with m_{A}. For strings which are refined and got mass changed, see figure 9.10b, we encounter a drop of the string length, which then recover and the string has a longer lifetime as the original string. If we have a loop with an infinitely thin core, the string should persist forever. Our approach to refine the string, tighten the core by changing its mass and cut the string again if becomes small again can be seen schematically in figure 9.11a. The strings which were cut, starts at time τ_c. Evaluating all strings, we see in figure 9.11b that the time increases with cutting and mass changing. Accordingly we have for $\Delta\tau_{\text{r}} = 1.8, \pm 4.9, \Delta\tau_{\text{m}} = 3.8, \pm 5.4$ and $\Delta\tau_{\text{c}} = 11.2 \pm 8.8$, where r stands for refined without mass changing, m for refined with mass changing and c for refined with mass changing and cut. All in all, we see a slight change of the lifetime of the string. However, we do not know how the strings we cut should behave; therefore, we do not
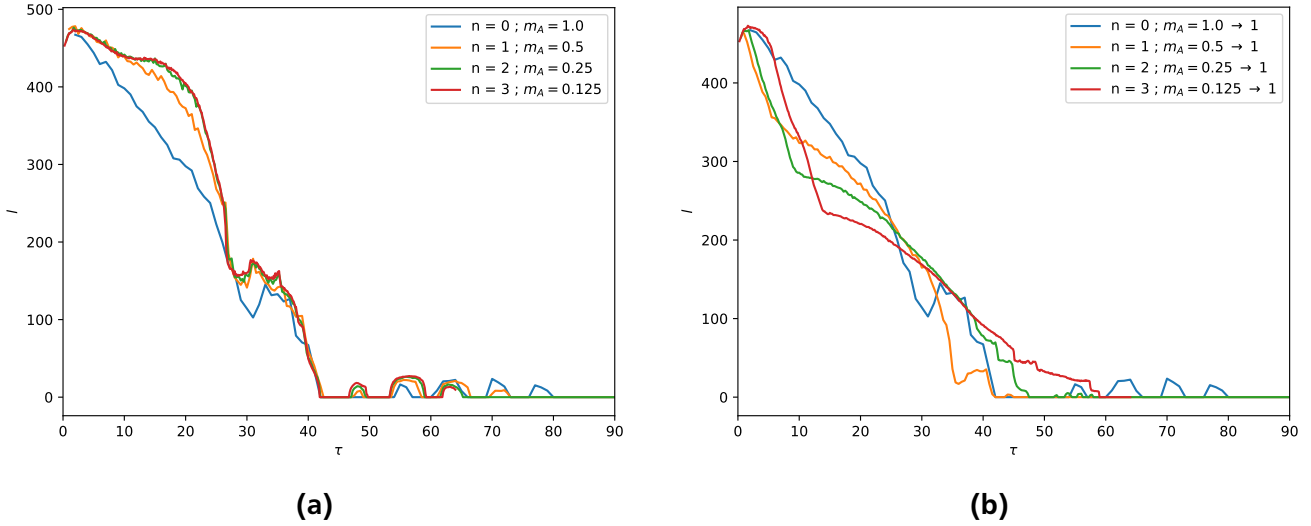
(a)

(b)

Figure 9.10.: Both pictures show an expample string, which is on the left refined but not mass changed and on the right mass changed to $m_A = 1$.
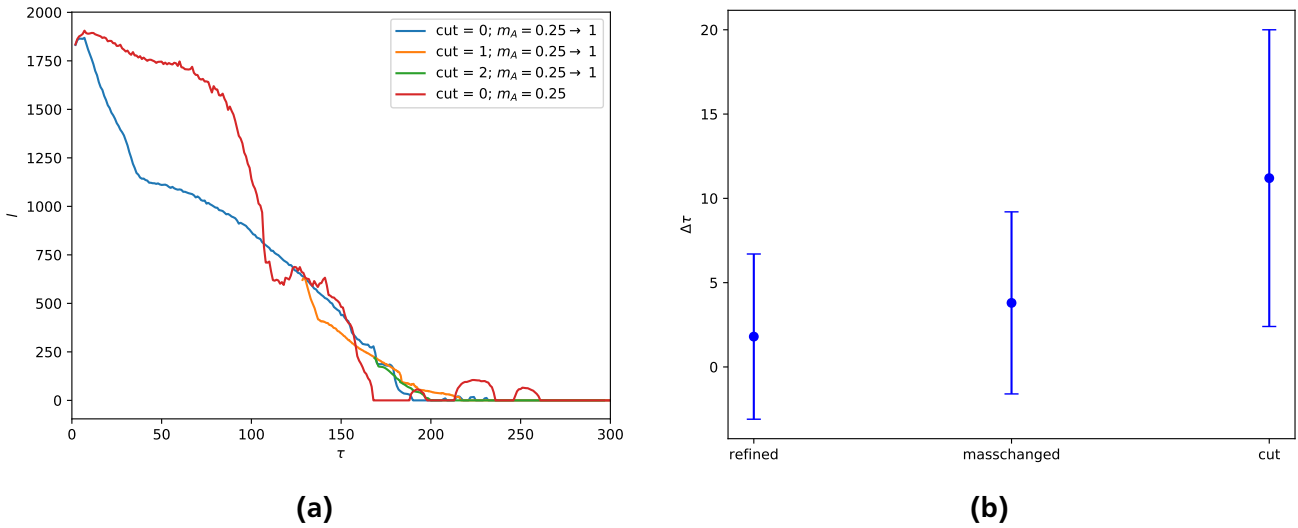

(a)

(b)

Figure 9.11.: (a): The evolution of a string after refining, cutting, and mass changing. **(b)**: The change of the lifetime of strings, where the left data point is a refined but not mass changed string. In the middle it is mass changed but not cut, and at the right it is refined, mass changed, and twice cut.

know when strings start to behave odd. To be more precise in the behavior of string dynamics and the lifetime of a string, we need a string whose dynamics is theoretically known and can be compared. In the next section we present a novel method where we construct a string out of the Nambu-Goto solution and evolve it by field dynamics.

9.2 Local Strings Constructed by Nambu-Goto Strings

The evolutionary limit of global string networks in which they have very thin string cores compared to their size, should behave just like local strings [29]. The effective action of local strings is the Nambu-Goto action which describes the string core. But how evolution exactly looks like and what limits to lattice calculation exists is not well understood yet. However, it is very important to understand the string evolution on the microscopic scale to get a better general picture of string evolution in lattice theory. In this section we will show how to implement initial conditions on the lattice from a solution of the effective Nambu-Goto action.

9.2.1 Nambu-Goto String

As we concluded from section 6.1.1, the string dynamics for thin cores is determined by the equation of motion

$$\ddot{x}^{\mu} - x^{\mu''} = 0. \tag{9.2.1}$$

The general solution for this differential equation is

$$x(\sigma, t) = \frac{1}{2}[a(\sigma + t) - b(\sigma - t)], \tag{9.2.2}$$

where $\sigma \in [0, L]$ and L is the length of the string. The constraints for the right and left moving string parts are

$$|a'|^2 = |b'|^2 = 1. \tag{9.2.3}$$

The spatial derivatives, $a'(\sigma, t)$ and $b'(\sigma, t)$, can be mapped on the Kibble-Turok sphere, with a time-independent structure of the curve at the sphere. Using this representation one can directly see if the string will have cusps or kinks. As we have seen in chapter 6, cusps leads to string velocities of $\dot{x}(\sigma_0, t_0) = 1$ and kinks to sharp edges on a string. The assumption of constructing a string which fits the constraints for the general solution is large, but the more specific the dynamics of the string gets the harder it is to construct a well defined solution. The Kibble-Turok sphere does not tell if a string is non-self-intersecting. Since this type of string is of particular interest for us, it has to be checked if the string fulfills

$$\int_{\sigma}^{\sigma+l} a'(\tilde{\sigma} - t)d\tilde{\sigma} - \int_{\sigma}^{\sigma+l} b'(\tilde{\sigma} + t)d\tilde{\sigma} \neq 0 \qquad \forall \sigma, l, t \in [0, 2\pi]. \tag{9.2.4}$$

It is convenient to rewrite a set of solutions in a' and b'. We claim that the following new solution is free of cusps, kinks and self-intersections:

$$a' = \begin{bmatrix} \cos(\sigma + t)\sqrt{1 - a_z^2} \\ \sin(\sigma + t)\sqrt{1 - a_z^2} \\ \frac{3}{4}\cos(2(\sigma + t)) \end{bmatrix}, \tag{9.2.5}$$

$$b' = \begin{bmatrix} \sqrt{\frac{8}{9}}\sin(2(\sigma - t))\sqrt{1 + 8\cos^6(2(\sigma - t))} \\ 0 \\ -(\frac{2}{3}\cos(4(\sigma - t)) + \frac{1}{3}\cos(8(\sigma - t))) \end{bmatrix}. \tag{9.2.6}$$

We will use this solution for our following investigations and constructions of a field theoretical string. It is important to have a non self-intersecting string because a string always intercommute when it self-interacts. The possibility that it recombines twice and therefore passes through is very low [102, 132]. For other solutions which also have kinks, cusps or self-intersections see Appendix E as we will not discuss these solutions in this thesis. To obtain $x(\sigma, t)$ we have to integrate numerically the left- and right-moving parts of Eq. (9.2.5) and Eq. (9.2.6), which is analytically not known. The expression of the tangential vector and the velocity of the string is:
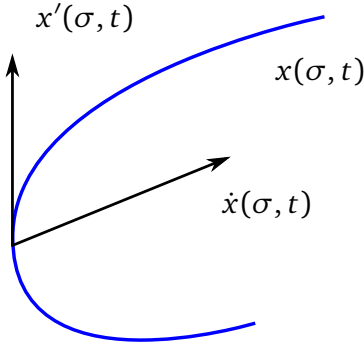
$$x'(\sigma, t) = \frac{1}{2}\left(a' - b'\right), \qquad (9.2.7)$$

$$\dot{x}(\sigma, t) = \frac{1}{2}\left(a' + b'\right). \qquad (9.2.8)$$

Figure 9.12.: Schematic picture of the string $x(\sigma, t)$ shown as the blue line, their velocity $\dot{x}(\sigma, t)$ and tangential vector $x'(\sigma, t)$

These three components are very important for a later discussion of the string construction.

9.2.2 Map Nambu-Goto Solution to Fields

We now have a solution which describes the equation of motion of one specific string. Now we want to use this solution to generate initial conditions for lattice calculations, that is we want to find the fields $\phi(\vec{r})$ and $A_i(\vec{r})$ which correspond to this Nambu-Goto string. Since we evolve fields on the lattice, we need to transform the solution of the equation of motion to a field theoretical description. Let us start with the solution for gauge fields and scalar fields in cylindrical coordinates for a straight non moving string as already mentioned in chapter 5,

$$A_\phi = \frac{g(r)}{r}, \qquad (9.2.9)$$

$$\phi_\rho = \frac{f(r)}{\sqrt{2}}e^{i\varphi}e^{i\theta_0}, \qquad (9.2.10)$$

where θ_0 is an additional overall phase. The solution of our equation of motion we obtained from the Nambu-Goto string, is not a straight line. Also the *Ansatz* is chosen in cylindrical coordinates, we therefore have to transform them back to Cartesian coordinates in order to have an equivalent description for the lattice which also handles Cartesian coordinates. The transformation from cylindrical to Cartesian coordinates are

$$\mathrm{R} = \begin{bmatrix} \cos(\varphi) & -\sin(\varphi) & 0 \\ \sin(\varphi) & \cos(\varphi) & 0 \\ 0 & 0 & 1 \end{bmatrix}, \qquad (9.2.11)$$

$$\mathrm{R}\vec{A} = \begin{bmatrix} \cos(\varphi) & -\sin(\varphi) & 0 \\ \sin(\varphi) & \cos(\varphi) & 0 \\ 0 & 0 & 1 \end{bmatrix}, \begin{bmatrix} 0 \\ A_\varphi \\ 0 \end{bmatrix} = \begin{bmatrix} -\sin(\varphi)A_\varphi \\ \cos(\varphi)A_\varphi \\ 0 \end{bmatrix} = \begin{bmatrix} \frac{-y}{r^2}g(r) \\ \frac{x}{r^2}g(r) \\ 0 \end{bmatrix}, \qquad (9.2.12)$$

with $x = r\cos(\phi)$ and $y = r\sin(\phi)$. With these expressions we can derive the magnetic field

$$\begin{bmatrix} B_x \\ B_y \\ B_z \end{bmatrix} = \begin{bmatrix} \partial_y A_z - \partial_z A_y \\ \partial_z A_x - \partial_x A_z \\ \partial_x A_y - \partial_y A_x \end{bmatrix} = \begin{bmatrix} 0 \\ 0 \\ \frac{2}{r^2}g(r) + \frac{x^2+y^2}{r^4}(rg'(r) - 2g(r)) \end{bmatrix} = \begin{bmatrix} 0 \\ 0 \\ \frac{g'(r)}{r} \end{bmatrix}. \tag{9.2.13}$$

For the fields we use Euler's formula which leads to:

$$\phi_\rho(r, \varphi) = f(r)e^{i\varphi} = (\cos(\varphi) + i\sin(\varphi))f(r) = \frac{(x + iy)}{r}f(r)e^{i\theta_0}. \tag{9.2.14}$$

As mentioned before, the solution of the Nambu-Goto string is not a straight line as our *Ansatz* proposes. This means that for each straight segment of string, the map between the Cartesian coordinates where the string lies on the z-axis and the global lattice system of coordinates will be different. We will choose local coordinates so $\dot{x}(\sigma, t)$ lies in the x-direction. But the parameter θ_0 will need to vary along the string and we have to determine how. The initial value can be arbitrary chosen and is $\theta_{\text{start}} = 0$. With this additional phase we get to the introduced form

$$\phi_\rho(r, x, y, \theta) = \phi_\rho(r, x, y)e^{i\theta} = \frac{(x + iy)}{r}f(r)e^{i\theta_0}. \tag{9.2.15}$$
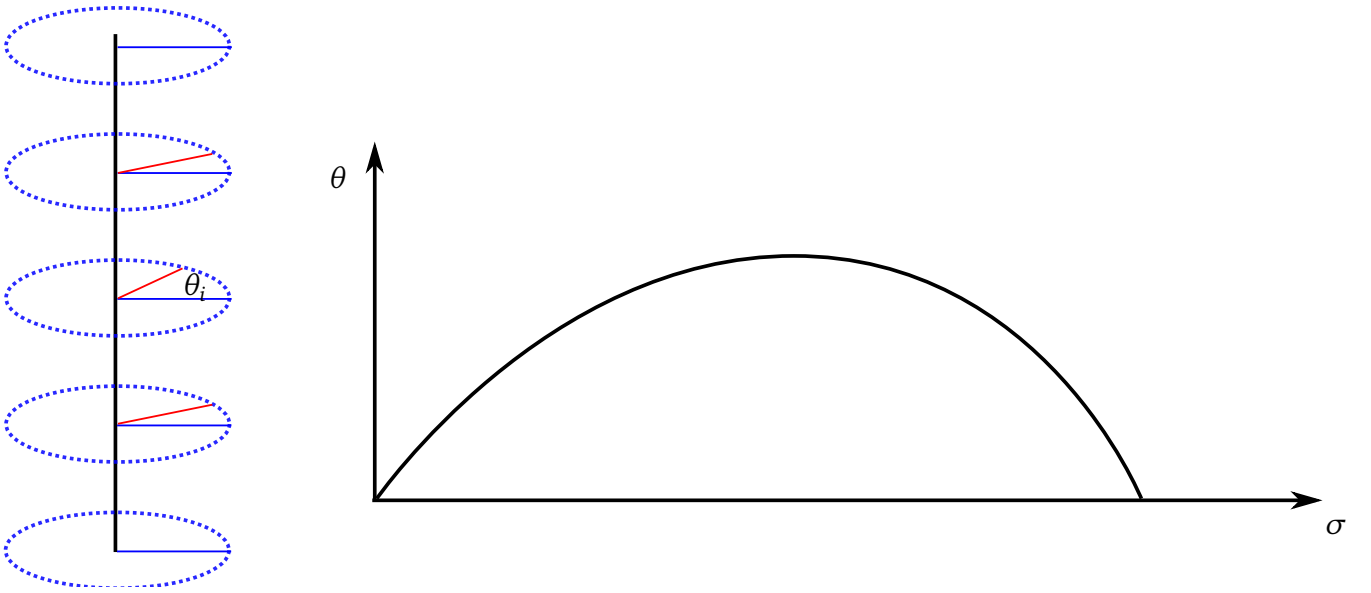

Figure 9.13.: The black line indicates a straight string, where the blue dashed circles have the radius of the velocity. The red line is the velocity at a different point and θ_i the shift between them. A schematic function of θ is at the right side.

Clearer, we see in figure 9.13 on the left a straight string with rotating velocity. The phase starts at $\theta_{\text{start}} = 0$, which again can be arbitrarily chosen. The rotation of the velocity is continuous and is shown schematically at the right of the figure. Since we are only considering closed strings, the parameter always has to fulfill $\theta_{\text{start}} = \theta_{\text{end}} + 2n\pi$ where $n \in \mathbb{Z}$. After we identified the θ parameter we rotate the velocity back to the origin of θ_{start}. This will be explained in greater detail in section 9.2.4. Since the solution is also non moving, we have to boost the system which will be explained in the next section.

9.2.3   Boosted String System

The considered solution for the local string is unboosted, since the Nambu-Goto string solution has a velocity, we have to perform a Lorentz boost Λ_x for non moving strings. This is known as

$$
\Lambda_x = \begin{bmatrix} \gamma & -\gamma v & 0 & 0 \\ -\gamma v & \gamma & 0 & 0 \\ 0 & 0 & 1 & 0 \\ 0 & 0 & 0 & 1 \end{bmatrix},
\tag{9.2.16}
$$

$$
\begin{bmatrix} \tilde{t} \\ \tilde{x} \\ \tilde{y} \\ \tilde{z} \end{bmatrix} = \begin{bmatrix} \gamma(t - vx) \\ \gamma(x - vt) \\ y \\ z \end{bmatrix}.
\tag{9.2.17}
$$

This leads for the gauge fields after setting $A_z = 0$ to

$$
\begin{bmatrix} \tilde{A}_0 \\ \tilde{A}_x \\ \tilde{A}_y \\ \tilde{A}_z \end{bmatrix} = \begin{bmatrix} \gamma A_0 - \gamma v A_x \\ -\gamma v A_0 + \gamma A_x \\ A_y \\ A_z \end{bmatrix} = \begin{bmatrix} -\gamma v A_x(\tilde{y}, \tilde{r}) \\ \gamma A_x(\tilde{y}, \tilde{r}) \\ A_y(\tilde{x}, g(\tilde{r})) \\ 0 \end{bmatrix},
\tag{9.2.18}
$$

and for the field strength tensor $\tilde{F}^{\mu\nu} = \Lambda_x F^{\mu\nu} \Lambda_x^{-1}$ after setting all fields to zero except for B_z to

$$
F^{\mu\nu} = \begin{bmatrix} 0 & -E_x & -E_y & -E_z \\ E_x & 0 & -B_z & By \\ E_y & B_z & 0 & -B_x \\ E_z & -B_y & B_x & 0 \end{bmatrix} = \begin{bmatrix} 0 & 0 & 0 & 0 \\ 0 & 0 & -B_z & 0 \\ 0 & B_z & 0 & 0 \\ 0 & 0 & 0 & 0 \end{bmatrix},
\tag{9.2.19}
$$

$$
\tilde{F}^{\mu\nu} = \begin{bmatrix} 0 & 0 & -\gamma v B_z(\tilde{x}, \tilde{y}, \tilde{r}) & 0 \\ 0 & 0 & -\gamma B_z(\tilde{x}, \tilde{y}, \tilde{r}) & 0 \\ \gamma v B_z(\tilde{x}, \tilde{y}, \tilde{r}) & \gamma B_z(\tilde{x}, \tilde{y}, \tilde{r}) & 0 & 0 \\ 0 & 0 & 0 & 0 \end{bmatrix}.
\tag{9.2.20}
$$

Finally we end up with an expression for the electric field $\tilde{E}_y$ and for A_t by boosting the system. Note, that we have to insert the transformed coordinates into the fields. For the fields we can express

$$
\tilde{\phi}(x, y, t) = \frac{(\gamma(-vt + x) + iy)}{\tilde{r}} f(\tilde{r}) e^{i\theta},
\tag{9.2.21}
$$

$$
\overset{\tilde{t} \to 0}{=} \frac{(\gamma x + iy)}{\tilde{r}} f(\tilde{r}) e^{i\theta},
\tag{9.2.22}
$$

$$
r(\tilde{x}, \tilde{y}, \tilde{t}) = \tilde{r}(x, y, t) = \sqrt{\gamma^2(-vt + x)^2 + y^2}.
\tag{9.2.23}
$$

We have to take the covariant derivative $D_\mu = \partial_\mu + ie\tilde{A}_\mu$ of the field to obtain

$$
D_t \tilde{\phi}(x, y, r, t, \theta) = \partial_t \tilde{\phi}(x, y, r, t, \theta) + ie\tilde{A}_t(y, r)\tilde{\phi}(x, y, r, t, \theta),
\tag{9.2.24}
$$

$$
= \left(\frac{iy\gamma v(1 - g(r))}{r^2} - \frac{\gamma^2 vxf'(r)}{f(r)} \right) \tilde{\phi} e^{i\theta}.
\tag{9.2.25}
$$

All relevant expressions are

$$
\begin{aligned}
r &= \sqrt{(\gamma x)^2 + y^2} \\
\phi &= \tfrac{(\gamma x + iy)}{r} f(r) e^{i\theta} \\
D_t \phi &= \left(\tfrac{iy\gamma v(1-g(r))}{r^2} - \tfrac{\gamma^2 v x f'(r)}{f(r)} \right) \phi e^{i\theta} \\
A_x &= \gamma \tfrac{-y}{r^2} g(r) \\
A_y &= \tfrac{\gamma x}{r^2} g(r) \\
E_y &= -\gamma v \tfrac{g'(r)}{r}
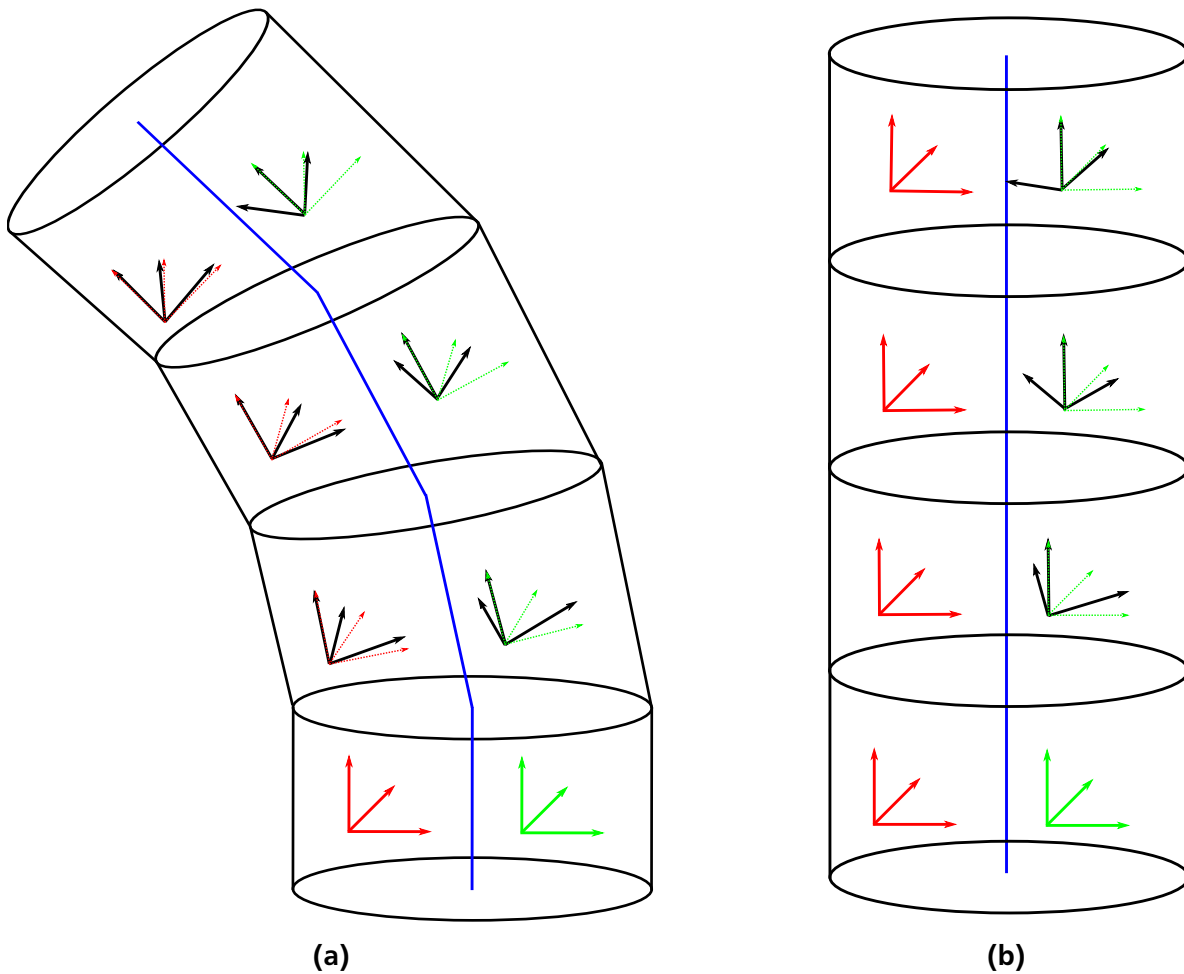\end{aligned}
$$

9.2.4 Constraints to the Z-Axis

Figure 9.14.: Schematic picture of two string segments, where the left figure 9.14b depicts a curved string segment while the right figure 9.14a, depicts the transformed straightened string segment. The coordinate systems in the left of the string part shown in red describe the curvature and the torsion of the string, while in green on the right of the string segment, it describes the Nambu-Goto solution. Straighten the string aligns the curvature and torsion of the string which makes it accessible to calculate the phase θ

The solution of the field equation is derived in cylindrical coordinates, i.e. a straight string is assumed and described. To be able to apply the solutions to curved strings or closed strings, the factor $\theta(\sigma, t)$ was introduced in 9.2.2. Our goal is to find a suitable parameterization for the string that provides a unique solution for $\theta(\sigma, t)$ to then adjust the fields to describe the correct physics for closed strings. That is, if

we cut the closed string at one point and drag it straight, all $e_x(\sigma)$ and all $e_z(\sigma)$ must point in the same direction. Another way to see it is shown in figure 9.16, where the direction of all $e_x(\sigma)$ is parallel to the minimized surface enclosed by the string. In order to understand the problem, we started with a naive approach, which does not lead to the correct solution in the end, but was useful for the process of finding a solution. The unique solution for $\theta(\sigma, t)$ developed by us will be presented afterwards. Since $t = t_{\text{init}}$, we will write $\theta(\sigma, t) = \theta(\sigma)$. In figure 9.14, the blue solid line represents a string segment $x(\sigma)$. The red coordinate system represents the torsion free continuation along the string line, where the green coordinate system represents the propagated velocity $\dot{x}(\sigma_0)$, with σ_0 the initial starting point of the string segment. The normalized vectors are described as $e_z(\sigma) = x'/|x'|$ and $e_x(\sigma) = \dot{x}/|\dot{x}|$, where $e_y(\sigma) = e_z \times e_x$. These three vectors form an orthonormal base. At each point the contribution for x' and $\dot{x}$ changes, so that a rotation of the coordinate system occurs. For the initial σ we choose $\sigma_0 = 0$. On the right picture in figure 9.14, we have the same string segment, which is already transformed to a straight line. We see that the red coordinate system is now equal at every segment and for the green coordinate system only the rotation by $\theta(\sigma, t)$ occurs. We will now present a method to apply these rotations. To correctly describe the fields ϕ and $\dot{\phi}$ we have to transport the system from $e_x(\sigma_i)$, $e_y(\sigma_i)$, $e_z(\sigma_i)$ to the system $e_x(\sigma_0)$, $e_y(\sigma_0)$, $e_z(\sigma_0)$. A base transformation is not possible for the scalar fields, because it automatically yields $\theta = 0$. Effectively, we want a transformation which gives us $e_z(0) = Re_z(\sigma_i)$ but not necessarily $e_x(0) = Re_x(\sigma_i)$, where R is the general rotation matrix

$$R(\vec{v}_{\text{rot}}, \alpha) = \begin{bmatrix} c + v_1^2(1-c) & v_1 v_2(1-c) - v_3 s & v_1 v_3(1-c) + v_2 s \\ v_2 v_1(1-c) + v_3 s & c + v_2^2(1-c) & v_2 v_3(1-c) - v_1 s \\ v_3 v_1(1-c) - v_2 s & v_3 v_2(1-c) + v_1 s & c + v_3^2(1-c) \end{bmatrix}, \tag{9.2.26}$$

with $c = \cos(\alpha)$, $s = \sin(\alpha)$ and $\vec{v}_{\text{rot}}$ the rotation vector. The desired angle can then be determined to $\theta = \sphericalangle(e_x(0), Re_x(\sigma_i))$ at the string point $x(\sigma_i)$. A naive approach for the rotation matrix R is to determine the rotation vector v_{rot} by $v_{\text{rot}} = e_z(0) \times e_z(\sigma_i)$. The resulting rotation matrix for the angle $\sphericalangle(e_z(0), e_z(\sigma_i))$ then satisfies the condition $e_z(0) = Re_z(\sigma_i)$. However, this approach does not lead to a unique solution since at points with $e_z(0) \approx -e_z(\sigma_i)$ the angle for $\sphericalangle(e_x(0), Re_x(\sigma_i))$ is degenerate.
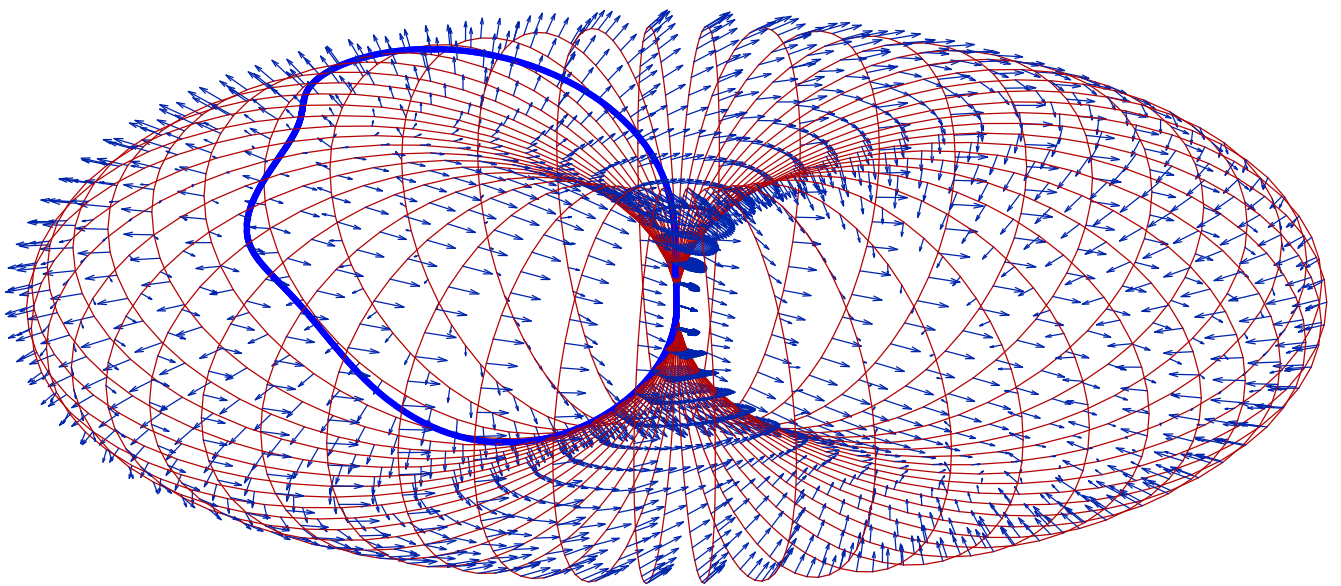

Figure 9.15.: The Torus surface indicates all possible velocity directions the system could take. The blue line is a specific path of an explicit string.

We separate the working developed solution of the problem into multiple steps. First we explain a tool that can describe all possible paths a closed string can go through. This construction is a torus on whose surface all possible rotation combinations of e_x and e_z are shown. In figure 9.15 the surface is depicted with an example string trajectory on it. The torus is constructed by using toroidal coordinates

$$\vec{x} = \begin{bmatrix} (R + r \cos \xi) \cos \phi \\ (R + r \cos \xi) \sin \phi \\ r \sin \xi \end{bmatrix}, \tag{9.2.27}$$

where $R = r$, ϕ is the azimuthal angle of the torus and ξ the polar angle. This ensures that we arrive at the origin again at the end of the closed string, since we have to make sure that $\theta(0) = \theta(2\pi)$. At the origin is $\xi = 0$ and $\phi = 0$ and we define the vectors $e_{T,x}(\xi = 0, \phi = 0) = e_x(\sigma = 0)$ and $e_{T,z}(\xi = 0, \phi = 0) = e_z(\sigma = 0)$, where T stands for torus, it follows that $\theta(0) = 0$. The surface, with all rotation possibilities that apply to closed strings, is set as follows: The vector $e_{T,x}(0,0)$ will be rotated around the vector $e_{T,z}(0,0)$ and the angle $\phi \in [0, 2\pi]$. The rotation vector is therefore

$$v_{\text{rot}}(\phi) = e_{T,z}(0,0) \times (R(e_{T,z}(0,0), \phi)e_{T,x}(0,0)). \tag{9.2.28}$$

The following rotation with the rotation matrix $R(v_{\text{rot}}(\phi), \xi)$ around the angle $\xi \in [0, 2\pi]$ results in

$$e_{T,x}(\xi, \phi) = R(v_{\text{rot}}(\phi), \xi)e_{T,x}(0,0), \tag{9.2.29}$$

$$e_{T,z}(\xi, \phi) = R(v_{\text{rot}}(\phi), \xi)e_{T,z}(0,0). \tag{9.2.30}$$

A rotation of ξ is equivalent to a closed path on the torus, where the position of the vectors on the surface is described by the torus Eq. (9.2.27). This representation illustrates the change of the curvature κ by the torsion τ of the string. Now, we have to project the string onto the surface. To do this, we look at the origin of $e_x(0)$ and $e_z(0)$ again as well as $e_x(\sigma_i)$ and $e_z(\sigma_i)$ and

$$t_s(\sigma_i) = \int_{\sigma = \sigma_0}^{\sigma_i} e_z(\sigma)d\sigma, \tag{9.2.31}$$

where $t_s(\sigma_i)$ represents the integrated distance from the tangential components. The vector t_s represents the relative position of the string with respect to the origin. From the vector t_s we define the angle $\xi/2 = \sphericalangle(t_s, e_{T,z}(0,0))$, and from the projection $p_{s,xy}$ of the vector $t_s(\sigma_i)$ on the $e_{T,x}(0,0)), e_{T,y}(0,0)$ plane we obtain the angle $\phi = \sphericalangle(p_{s,xy}, e_{T,x}(0,0))$. The factor of 1/2 results from the fact that $e_{T,z}(0, \phi) \parallel t_s(\sigma_i)$ at $\pi/2$. By inserting ξ and ϕ into the torus coordinates the trajectory of the string can be determined. Since the vectors $t_s(\sigma_i)$ and $e_{T,z}(\xi(\sigma_i), \phi(\sigma_i))$ are only parallel if the string has no torsion, another rotation is required to project our system onto the origin system. The rotation vector is given by $v_{\text{rot}} = e_{T,z}(\xi(\sigma_i), \phi(\sigma_i)) \times e_z(\sigma_i)$ and is rotated by the angle of the two vectors to obtain

$$\alpha = \sphericalangle[e_{T,z}(\xi(\sigma_i), \phi(\sigma_i)), e_z(\sigma_i)], \tag{9.2.32}$$

$$e_{x,mix} = R(v_{\text{rot}}, \alpha)e_{T,x}(\xi(\sigma_i), \phi(\sigma_i)), \tag{9.2.33}$$

at the plane of $e_x(\sigma_i)$ and $e_y(\sigma_i)$. The angle $\theta(\sigma_i) = \sphericalangle(e_x(\sigma_i), e_{x,mix})$ to be calculated now is the desired rotation angle for the fields ϕ and $\dot{\phi}$. The result of the ideal path can be interpreted as the minimum
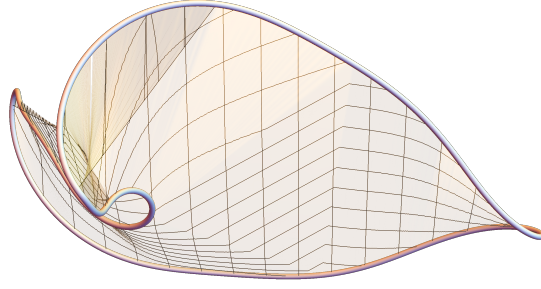
Figure 9.16.: Schematic depiction of a string with an indicated minimum surface between.

surface between the closed string in whose direction the constructed vectors point, figure 9.16 shows an example of such a surface. To rotate the gauge fields we need to perform a basis transformation by

$$T_{B'}^{B} = \begin{bmatrix} e_{x1} & e_{x2} & e_{x3} \\ e_{y1} & e_{y2} & e_{y3} \\ e_{z1} & e_{z2} & e_{z3} \end{bmatrix}, \tag{9.2.34}$$

where e_x describes again the velocity vector, e_z the tangential vector and $e_y = e_z \times e_x$. For the back transformation we have

$$T_{B}^{B'} = (T_{B'}^{B})^{\top}, \tag{9.2.35}$$

where B describes the set of tangential and velocity vector and B' the Cartesian coordinates. With that we are now able to generate the fields inside a tube, which we will explain in the next section.

9.2.5 Generating a Tube of Field Points

The solution for a straight string aligned in z- and boosted in x-direction of the gauge and scalar fields can be seen in section 9.2.3. For the functions $f(r)$ and $g(r)$ is no analytic solution known, a simple *Ansatz* is

$$f(r) = \begin{cases} 2\frac{r}{R} - \left(\frac{r}{R}\right)^2 & r < R \\ 1 & r \geq R \end{cases}, \qquad g(r) = \begin{cases} 3\left(\frac{r}{R}\right)^2 - 2\left(\frac{r}{R}\right)^3 & r < R \\ 1 & r \geq R \end{cases}, \tag{9.2.36}$$

$$f'(r) = \begin{cases} 2\left(\frac{1}{R} - \frac{r}{R^2}\right) & r < R \\ 0 & r \geq R \end{cases}, \qquad g'(r) = \begin{cases} 6\left(\frac{r}{R^2} - \frac{r^2}{R^3}\right) & r < R \\ 0 & r \geq R \end{cases}, \tag{9.2.37}$$

$$r = \sqrt{x^2 + y^2}, \tag{9.2.38}$$

where $R = 3.58/m$ minimizes the energy within this *Ansatz* returning energy about 5% higher then the exact solution. The analytic expression ensures that $\lim_{r \to R} f(r) = 1$ and $\lim_{r \to R} g(r) = 1$. Note that this only holds in the Bogomol'nyi limit $m_{\mathrm{H}} = m_{\mathrm{A}}$. Outside the string tube, we will initialize vacuum initial conditions. First, we label all points on the corner of a plaquette which is pierced by a string with $n = 1$. Plaquettes are the closest path one can achieve by circling string points on the lattice.

First of all, we need to find the nearest string points to the analytic string position. Afterwards, we label all points on the corner of a plaquette which is pierced by a string with $n = 1$, see Figure 9.17a. We then
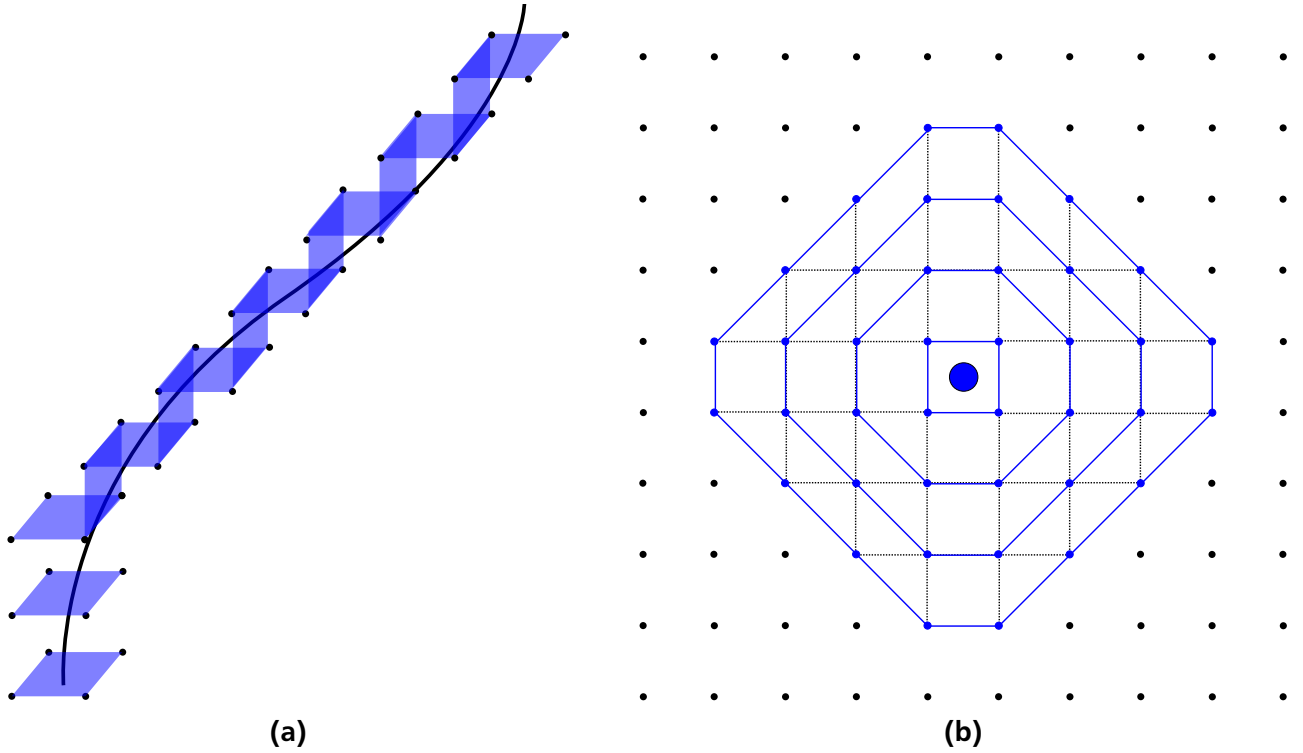
(a)   **(b)**

Figure 9.17.: (a): In black the constructed ideal string. The string crosses the blue plaquettes where the fields according to the plaquettes are marked as the fields nearest to the string. **(b)**: A two dimensional schematic picture of the string on lattice. The inner square is the closest marked with points $n_0 = 1$, where each further layer mark $n_i = n_0 + i$.

label each other point by its "Manhattan metric distance" to a depth of N. The depth of N dependents on the minimum radius of the osculating sphere. We reduce to the curvature radius as

$$r_{\min} = \frac{1}{\kappa} \leq \sqrt{\frac{1}{\kappa^2} + \frac{\kappa'^2}{\kappa \tau}}, \qquad (9.2.39)$$

where κ is the curvature and τ describes the torsion of the Frenet–Serret formula. For more details see Appendix D. If we knew the depth, we could create the tube by starting from the first points where $n = 1$ to the next unknown point and mark these points as $n+ = 1$ which can be seen in figure 9.17b. The dashed lines indicate the way from the inner to the outer points until we reach $n = N$, where

$$N = \sqrt{3} r_{\min}. \qquad (9.2.40)$$

With this expression we ensure that the radius of the outer points to the string is $r_{\text{point}} \geq R$.

As a next step we find the shortest vector connecting each point to the string. The vector from the lattice point to the string has to be orthogonal to the tangent vector, see figure 9.18b. By finding the shortest distance to the analytic string, we make sure we always have the vector on the e'_x and e'_y plane. In figure 9.18a we have a sketch of a two dimensional string on a lattice where the vectors are perpendicular to the analytic string. Since we are on a 3D lattice we actually have three directions, but generating the fields requires just two components. Consequently, we have to rotate the surface to the xy-plane to get the correct values for x and y at point (n_x, n_y). For the gauge field we also have to integrate to the next points $(n_x + 1, n_y)$ and $(n_x, n_y + 1)$ because the gauge fields live on links between these points. In figure 9.18b the red points illustrate the propagation on the rotated surface. The transformation of gauge fields
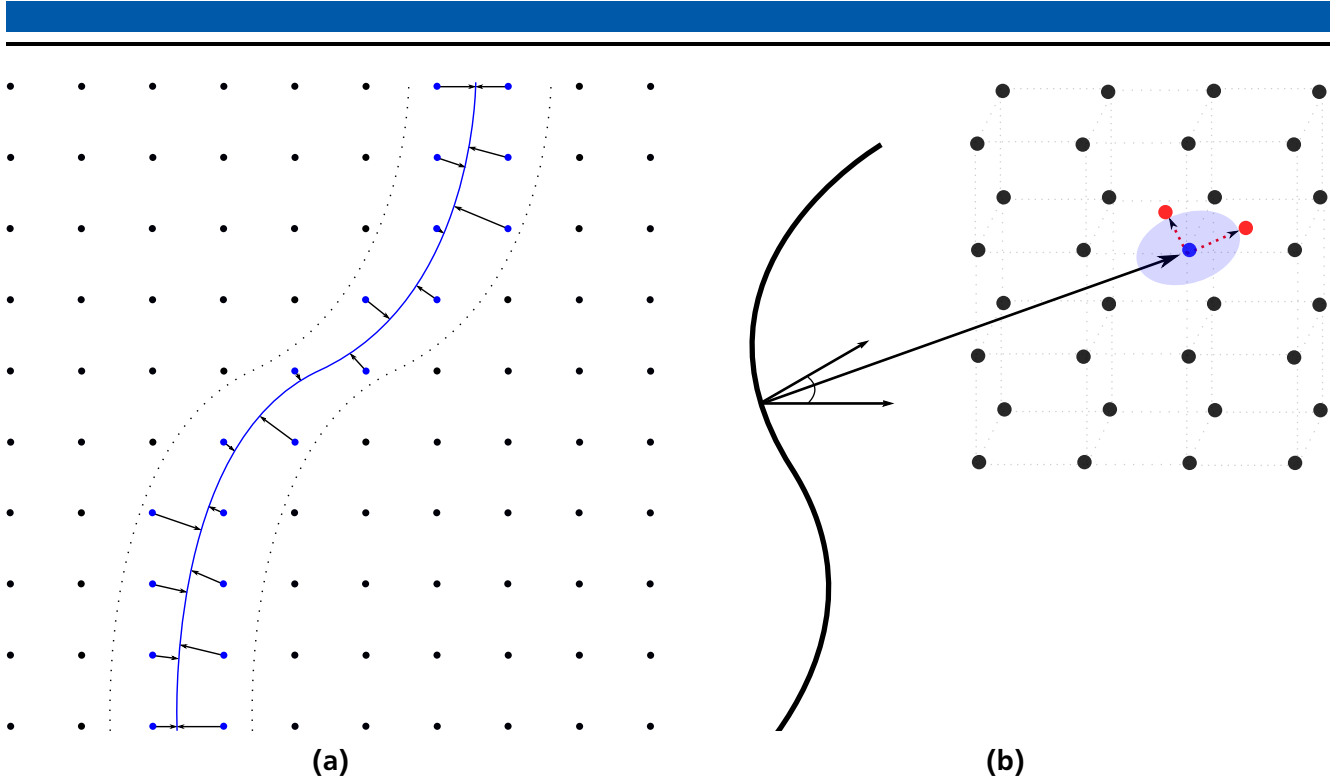
Figure 9.18.: (a): Finding the minimum distance of lattice points to the analytic string. The vectors indicates the shortest distance which does not need to be aligned. **(b)**: A specific example of the analytic string with the direction of the velocity at string position and the shortest vector to a lattice point. The lattice point lies on the plane of the analytic constructed e_x and e_y.

lead to the expression for the links on the lattice. We chose only the ϕ field to be set but not the gauge field A for the outer surface of the string tube.

9.2.6 Generating Field Points Outside the Tube

Outside the tube we have to set all field values to be in vacuum. We have two constraints which have to be fulfilled to be in vacuum

$$\phi_1 U(A) = \phi_2, \qquad (9.2.41)$$

where $U(A) = e^{iA}$, ϕ_n describes the field at a lattice site and

$$\nabla \times A = 0, \qquad (9.2.42)$$

being the magnetic field B. For the magnetic field we have to sum over the links of a plaquette; this summation depends on the direction of the link, for detailed information see Appendix B.

Imagine we propagate the fields from the outer surface of the tube in one direction. Figure 9.19 shows a point field propagating meets around the periodic boundary of the box. The gauge field for each propagation step is $A = 0$, since $\phi_1 = \phi_2$, except for the link where both field points meet, which is marked as the blue circle. In this sketched configuration the position of the fields at the complex plane are at the direct opposite, which leads to an $A = \pi$. This can lead to plaquettes where the magnetic field
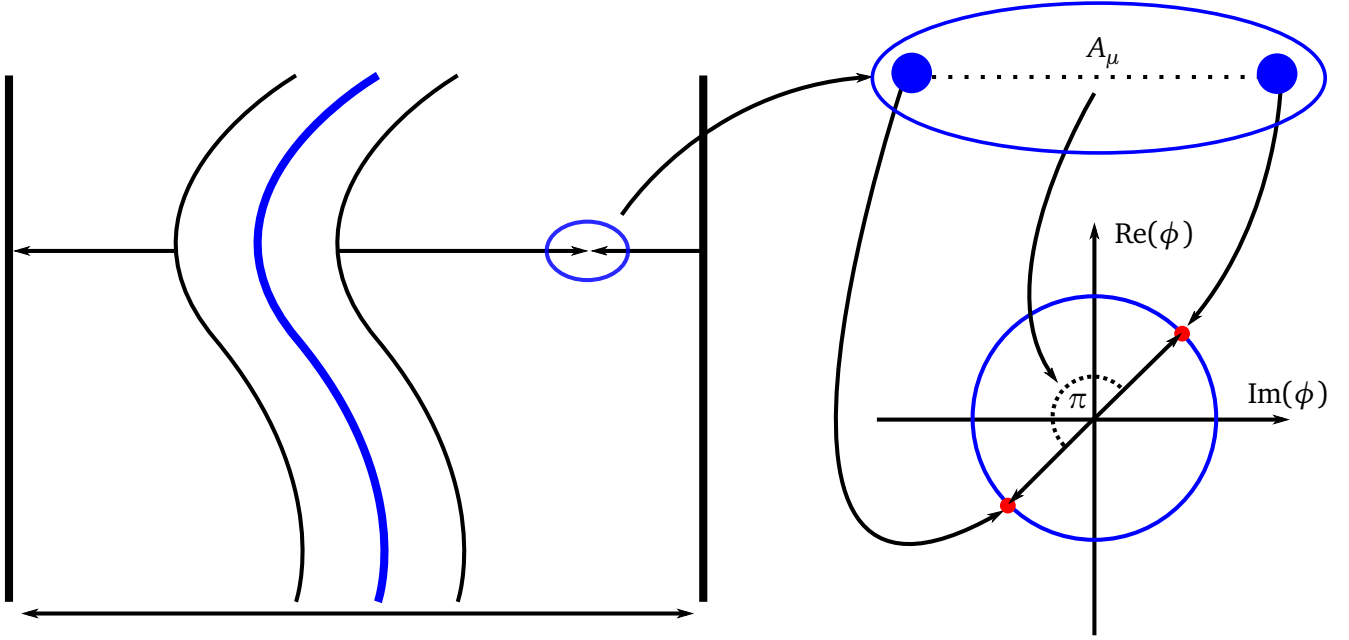
Figure 9.19.: The thick blue line is a string where the black lines around indicate the tube. The straight arrow shows the propagation of a field. At the point where both arrows meet, we zoom in. On the right side are two points which are already set one with the field propagated to the first point from the left and to the second point from the right. The complex plane is shown below where the dashed half circle is the shift the A field has to compensate.

$B \neq 0$, hence we have to minimize the A field by writing up the link and plaquette energy. For the link energy we have an imaginary and a real part which can be summed up to

$$E_{\mathrm{L}} = E_{\mathrm{L,Im}} + E_{\mathrm{L,Re}} . \tag{9.2.43}$$

The plaquette energy equals the magnetic energy E_B, the total energy is therefore

$$E_{\mathrm{tot}} = E_{\mathrm{L}} + E_B . \tag{9.2.44}$$

The parallel transport can be expressed as

$$\left[U(A)^{\dagger} \phi_{i+1} - \phi_i \right] = \left[(\cos(A) - i \sin(A))\left(\phi_{2,r} + i\phi_{2,i} \right) - \left(\phi_{1,r} + \phi_{1,i} \right) \right] , \tag{9.2.45}$$

where $\phi_{n,r}$ and $\phi_{n,i}$ express the real and imaginary part of the scalar field. We can rewrite this in a complex and a real part

$$\left[U(A)^{\dagger} \phi_{i+1} - \phi_i \right] = \left(\cos(A)\phi_{2,r} - \sin(A)\phi_{2,i} - \phi_{1,r} \right) + i \left(\cos(A)\phi_{2,i} + \sin(A)\phi_{1,r} - \phi_{1,i} \right) . \tag{9.2.46}$$

The link energy is

$$E_{\mathrm{L}} = \underbrace{\left(\cos(A)\phi_{2,r} - \sin(A)\phi_{2,i} - \phi_{1,r} \right)^2}_{E_{\mathrm{L,Re}}} + \underbrace{\left(\cos(A)\phi_{2,i} + \sin(A)\phi_{2,r} - \phi_{1,i} \right)^2}_{E_{\mathrm{L,Im}}} \tag{9.2.47}$$

$$= \phi_{2,r}^2 + \phi_{2,i}^2 + \phi_{1,r}^2 + \phi_{1,i}^2 - 2\phi_{1,r}\left(\cos(A)\phi_{2,r} - \sin(A)\phi_{2,i} \right)$$

$$- 2\phi_{1,i}\left(\cos(A)\phi_{2,i} - \sin(A)\phi_2, r \right) ,$$

while the magnetic energy is

$$E_B = \frac{1}{2e^2}\left(A + A_1 - A_2 - A_3\right)^2 , \tag{9.2.48}$$

where A_i are the known gauge fields and A is the desired one. At total there can be four plaquettes which contributes to the magnetic energy of the desired link by

$$E_{B\,\text{link}} = \frac{1}{2e^2}\sum_{i=0}^{3}\left(B_i(A)\right)^2 , \tag{9.2.49}$$

where $B_i(A) = A + A_{1,i} - A_{2,i} - A_{3,i}$ are the plaquette contributions. Therefore the total energy is

$$E = \left(\cos(A)\phi_{2,\text{r}} - \sin(A)\phi_{2,\text{i}} - \phi_{1,\text{r}}\right)^2 + \left(\cos(A)\phi_{2,\text{i}} + \sin(A)\phi_{1,\text{r}} - \phi_{1,\text{i}}\right)^2 + \frac{1}{2e^2}\sum_{i=0}^{3}\left(B_i(A)\right)^2 . \tag{9.2.50}$$

To find the minimum we have to impose $E'_{\text{tot}} = 0$. The derivative of the energy is

$$E'_{\text{tot}} = 2\Big[\left(-\sin(A)\phi_{r,i+1} + \cos(A)\phi_{i,i+1}\right)\left(\sin(A)\phi_{i,i+1} + \cos(A)\phi_{r,i+1} - \phi_{r,i}\right) \tag{9.2.51}$$

$$+ \left(-\sin(A)\phi_{i,i+1} - \cos(A)\phi_{r,i+1}\right)\left(-\sin(A)\phi_{r,i+1} + \cos(A)\phi_{i,i+1} - \phi_{i,i}\right)\Big] \tag{9.2.52}$$

$$+ \frac{1}{e^2}\sum_{i=0}^{3}B_i(A) . \tag{9.2.53}$$

There are five equations possible to evaluate but only two different scenarios, which are shown in figure 9.20. If we cannot calculate the plaquette due to a lack of information, the derivative does not have a unique expression. For this case we choose the minimum which is closest to $A = 0$, which is shown in figure 9.20b. For the case of a plaquette contribution, we always have a unique expression, which is shown in figure 9.20a.
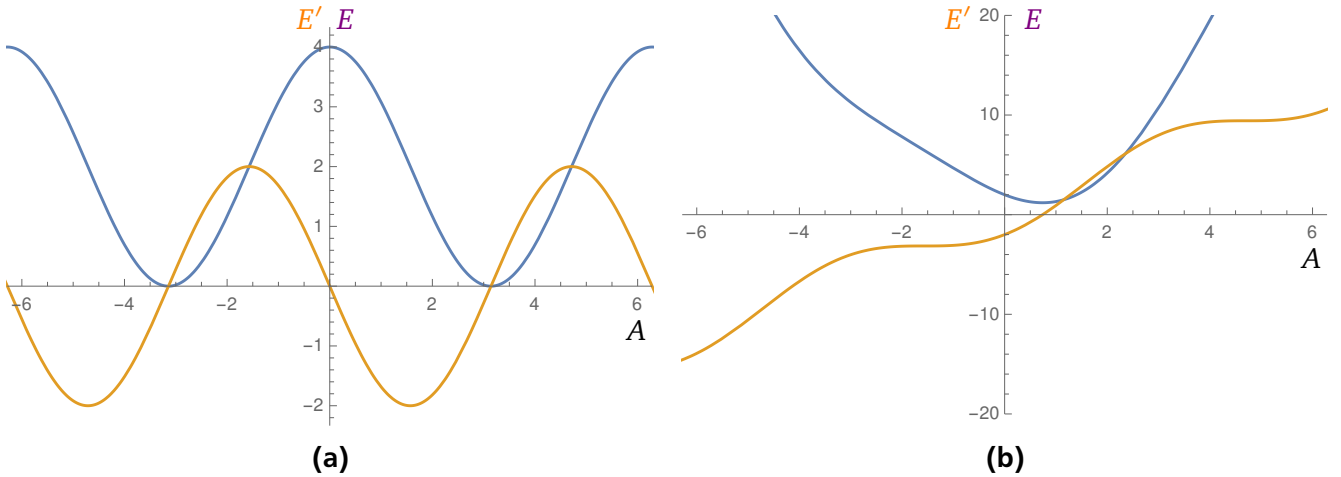

(a)   **(b)**

Figure 9.20.: (a): In blue the energy without magnetic field contribution E_L, where in orange the derivative E'_L is shown and has no link contributions. **(b)**: The same as for **(a)** but with more then one link contribution.

In figure 9.20a and 9.20b the energies and the derivatives are shown for the case without and with gauge field contributions.

There is another factor which also increases the precision to be close to the vacuum, which is the way how to propagate the fields. In figure 9.21a we see the basic idea of the propagation of the field. We already discussed the idea of propagating the tube points from the inner core to the outer surface. With the same algorithm we expand the tube surface layer by layer outside the tube to get smoothly distributed fields. If we had set the points not layer by layer we would have got artifacts which our relaxation method can't handle and therefore would persist forever. The layers are labeled by numbers, the current point takes the value of the field which is labeled with the smallest number see figure 9.21b for a demonstration in 3d.

(a)   **(b)**
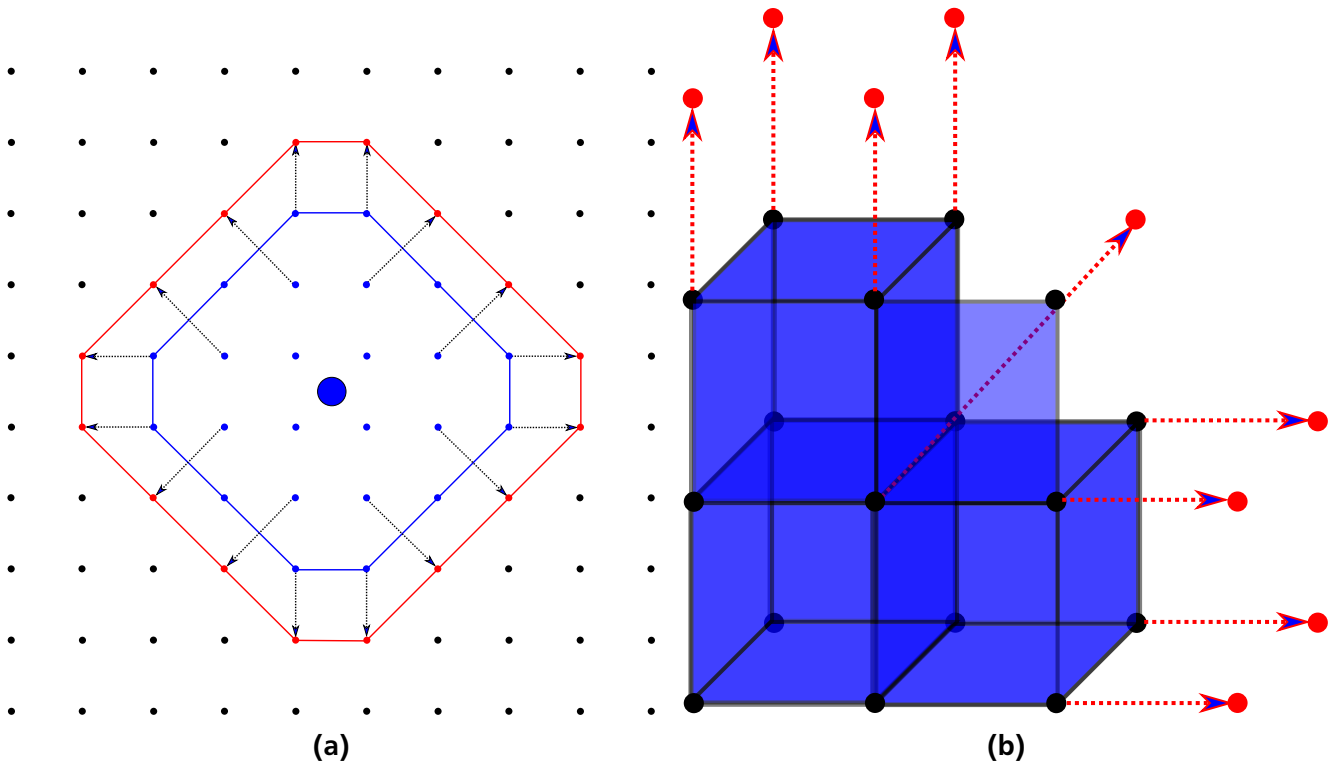
Figure 9.21.: (a): Propagation of tube fields on a 2d sheet. The fields get propagated from the closest field to the string core which is within a plaquette. **(b)**:Propagation of tube fields on a 3d sheet. The fields get propagated from the closest field to the string core which is within a cube.

After all scalar and gauge fields are set this way, we have to perform an evolution of the fields outside the tube, since outside the tube there are topological defects, which are unwanted artifacts. With this algorithm, the amount of defects is quite small and therefore after evolving the vacuum we will have vacuum outside the tube.

9.2.7 Relax Fields

After setting up the scalar and gauge fields we have to relax fields according to 9.1.2. The main difference of the method presented in the previous chapter is the handling of boundaries since the boundary is now the string tube surface. We therefore print a file which contains all tube points marked as one if the point is inside the tube and as zero if the point is outside the tube. This file is used to mask all fields and only performs the evolution on fields which are zero. After the energy of the system drops below the threshold and the number of string points is constant, the lattice configuration will be written in a binary file, with which we then start the physical evolution of the string system.

9.2.8 Results of NG Field Strings

Since it is claimed that non-intersecting Nambu-Goto string loops live forever, but it is never seen that such a string in a local network does, we want to investigate the behavior of such a string by fine tuning the thickness of the created string. With the previous presented method we can investigate strings in a novel way, since we can directly compare the solution with the Nambu-Goto solution; therefore, we would like to use the new method to study the repetition rate of a designed string. Creating a string requires that we set up some parameters we already have discussed. Since the approximated functions $f(r)$ and $g(r)$ are only valid for

$$m_H = m_A \equiv m, \tag{9.2.54}$$

we will always handle strings with equal masses. The description of a string $x(\sigma, t)$ has the parameters σ and t, where by construction $\sigma \in [0, 2\pi)$ takes every value and $t \in [0, 2\pi)$ is a constant we can choose based on the velocity and the curvature radius. Finding a string configuration with a low velocity at a specific time is important to have a more accurately constructed string. The curvature radius of the string has to be maximized, due to the dependency of the lattice spacing a and the string thickness m^{-1}. For the analytic string configuration we found a good value to be

$$t_1 = \frac{28}{25}\pi \qquad \text{or} \qquad t_2 = \frac{3}{25}\pi, \tag{9.2.55}$$

which gives in case of a string loop the same configuration because of

$$x(\sigma + t_1, t_1) = x(\sigma + t_1 + L/2, t_1 + L/2) = x(\sigma + t_2, t_2). \tag{9.2.56}$$

The different values we test are first the lattice size, where we only investigate cubic lattices and therefore

$$n_x = n_y = n_z, \tag{9.2.57}$$

second the lattice spacing a in the sense of am_A and third the string length-to-thickness ratio $L/2R$. The way we implemented the string length L is directly dependent of the lattice size, where the string thickness $2R$ is dependent of the lattice spacing as defined in section 9.2.5.

In figure 9.22, the three different cases we computed are shown. First in figure 9.22a we have a constant lattice spacing with a varying lattice size, which increases the string length-to-thickness ratio. Second, the string length-to-thickness ratio is constant but the lattice spacing gets finer; as shown in figure 9.22b. Finally the lattice spacing gets finer but also the string length-to-thickness ratio gets smaller which, is shown in figure 9.22c. We would like to achieve the continuum limit $a \to 0$ and increase the string
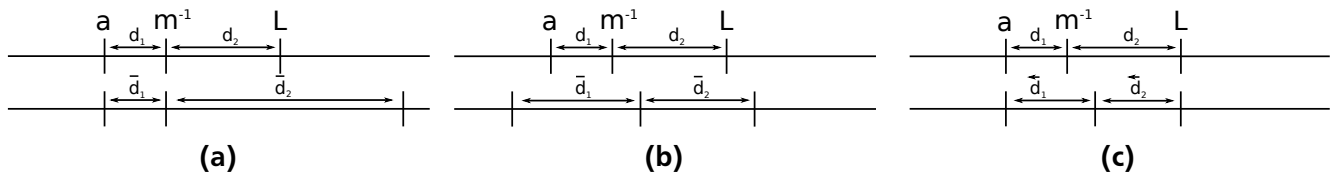

Figure 9.22.: (a): $d_1 = \bar{d}_1$ and $d_2 < \bar{d}_2$, which is the lattice spacing a and the thickness m^{-1} are fixed with growing lattice sizes n_x. **(b):** $d_1 < \bar{d}_1$ and $d_2 = \bar{d}_2$, therefore the string length-to-thickness ratio is constant while the spacing gets finer.**(c):** $d_1 + d_2 = \bar{d}_1 + \bar{d}_2$, describe a constant lattice size to spacing ratio.

length-to-thickness ratio, which is the case shown schematically in figure 9.22a.

Table 9.3.: Different lattice sizes by specific masses, equal colors indicates the same string length-to-thickness ratio.

n_x	256	320	512	640	1024
	1		1		
		0.8	0.8		0.8
m_A			0.5	0.5	0.5
				0.4	0.4
					0.25

In table 9.3 we have listed all investigated string configurations. The color indicates the same string length-to-thickness ratio across different configurations. We vary the box size and the lattice spacing, where we keep the time step size fixed to the ratio $\Delta\tau = 1/10$, which is a very conservative value [24]. To compare the Nambu-Goto solution with the actual evolved string, we define the ratio

$$\frac{\Delta t}{t_{2\pi}} = \frac{\tau_i - \tau_0}{L}, \tag{9.2.58}$$

where τ_0 is the time the simulation starts and τ_i the current time of the simulation. $t_{2\pi}$ is the time a Nambu-Goto string loop repeats itself. The initial length of the string is also the time a string needs to repeat on the lattice due to

$$x(\sigma, t) = x(\sigma, t + L). \tag{9.2.59}$$

With equation Eq. (9.2.58), we have an expression to compare the simulated string with the Nambu-Goto string. We scale the plot variables which vary with the lattice size by the invariant string length

$$L_{\text{init}} = \int \gamma \, dl, \tag{9.2.60}$$

which is the string length at time τ_0.

We will now compare the results we have found for the different simulations shown in table 9.3. First we take a look at the theoretical string energy $E_{\text{analytic,S}} = \pi L$, where L is the string length, with the measured lattice energy $E_{\text{latt,S}}$. Figure 9.23a shows the theoretical and measured string energy, where the constant yellow line is the total energy. Due to the constraints where to measure the string field energy with $|\phi| < 0.9$ (see section 9.1.4), we do not expect that the measured string energy exactly matches with the theoretical string energy.

Comparing equal string length-to-thickness ratios as mentioned in table 9.3, we see the green contribution of the table in figure 9.23b, where we plot the scaled energy over the conformal time. One clearly sees, that the string energy behaves more and more similarly with finer lattice spacing; based on this result we set the threshold to $m_A \leq 0.5$ for the remaining studies.

The constructed string we use has at each time an averaged velocity of $\langle v^2 \rangle = 0.5$. The velocity contribution for the initial time can be seen in figure 9.24a. This configuration has points which achieve a velocity which is higher than $v > 0.95$, which may be problematic due to the Lorentz contraction of the string when we implement it. The string will always have points with a velocity higher $v > 0.95$ for every $t \in [0, 2\pi)$. We therefore cannot discuss these effects in much detail, unless we are able to construct a string which has a more uniform velocity distribution.
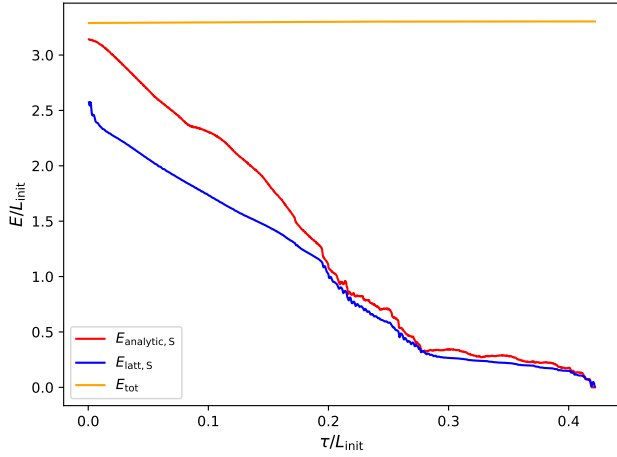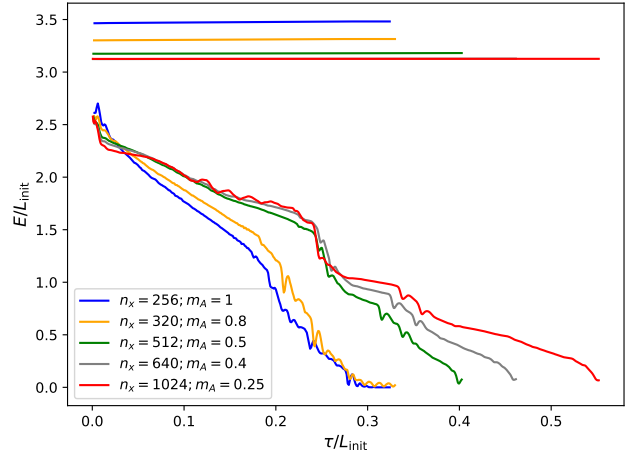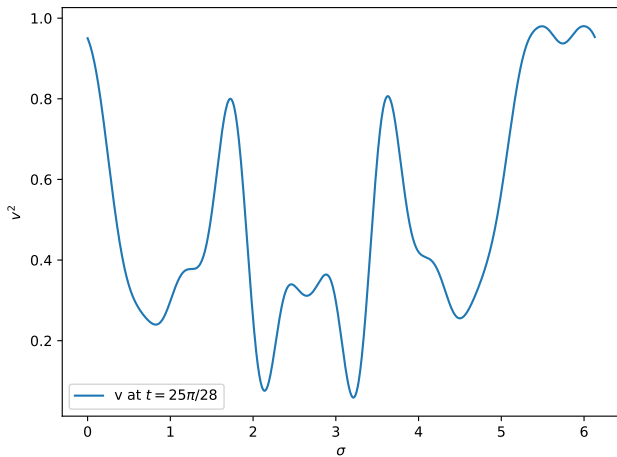
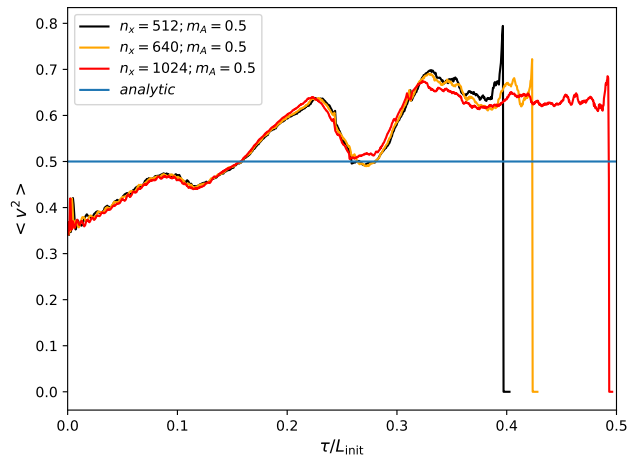**Figure 9.23.: (a)**: The theoretical string energy (red line) is compared with the string energy measured on the lattice. The orange line is the total Energy, the lattice size is $n_x = 1024$ with $m_A = 0.8$. **(b)**: All string energies for lattice systems with the same string length-to-thickness, showing how the continuum limit $a \rightarrow 0$ is approached.

Figure 9.24.: (a): The velocity squared profile is shown which the string initially has. **(b)**: The average velocity squared for $n_x = 1024$ strings with the same string length-to-thickness ratio is shown.

Figure 9.24b shows $\langle v^2 \rangle$ for all simulations with $m_A = 0.5$ and different lattice sizes. This represents the same case as depicted in figure 9.22a. The behavior of the velocities is almost the same until the string is gone.

The lifetime of the string can be measured in two ways; comparing the overall lifetime of the string until the string completely dissipates, and comparing the time it takes before the string stops following the theoretical string motion.

For the overall lifetime we see in figure 9.25a the string length over time with different string length-to-thickness ratios, where up to $\tau/L_{\text{init}} \approx 0.2$ the string lengths are almost the same. The total lifetime of the string does increase, but much less than we would expect. Due to this result, the string does not tend to behave more Nambu-Goto like with larger length-to-thickness ratio, as we would have expected.
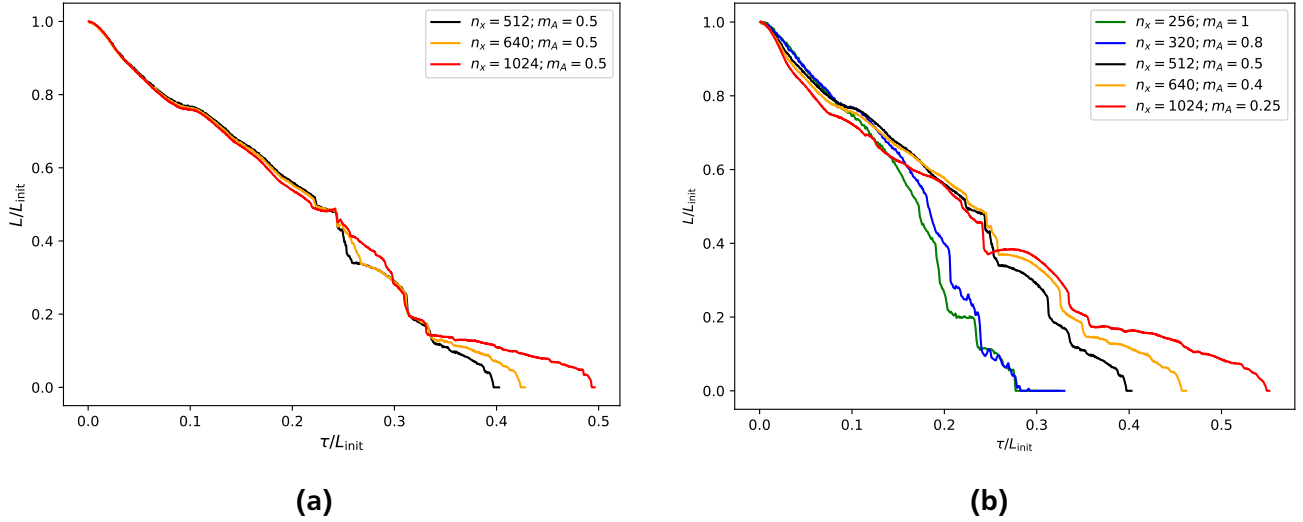
Figure 9.25.: (a): The string length over time with different string length-to-thickness ratios for $n_x = 1024$ is shown. **(b)**: All string lengths for lattice systems with the same string length-to-thickness ratio.

Comparing again different simulations, with the same length-to-thickness ratio, we see more clearly that the lifetime of the string growths with bigger lattice sizes and smaller lattice spacing, which can be seen in 9.25b. This increase of the lifetime is probably the same as we see in the results of section 9.1.6.

Measuring the time it takes before the string stops following the Nambu-Goto string motion is complicated to determine, because the string starts shrinking right from the beginning.

In figure 9.26 and 9.27 we show two decaying strings compared with the Nambu-Goto string. The strings are plotted from left to right on the xy, xz, and yz-plane. In the first row the time at $\tau = 0$ is shown and increases in $\Delta\tau = 167$ steps. The corresponding time steps for the Nambu-Goto string is $\Delta t = 1/10$ and therefore the final time is $t_{\text{final}} = 4\pi/5$,where $t \in [0, 2\pi)$. We see, that the strings *follow* the theoretical description for a short time but shrinks immediately after the simulation starts. However, the strings do not live much longer and it seems we are far away from the Nambu-Goto limit.
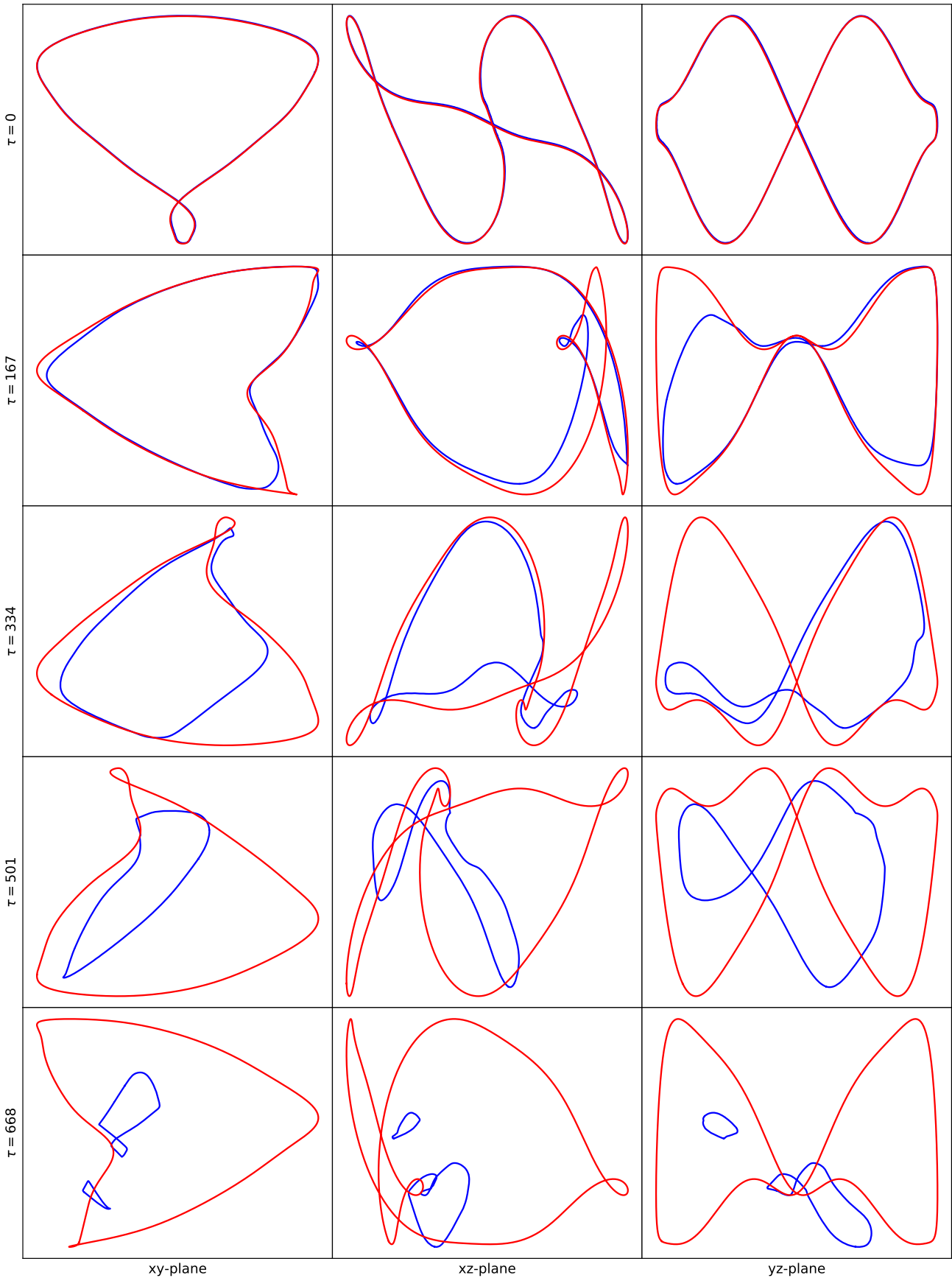
Figure 9.26.: A comparison between a three dimensional evolved string in blue with $m_A = 0.8$ and $n_x = 1024$ and the Nambu-Goto string in red for different times. We show from left to right, the xy, xz, and yz-plane. Starting from the top at time $\tau = 0$ in steps of 167 to $\tau = 668$.
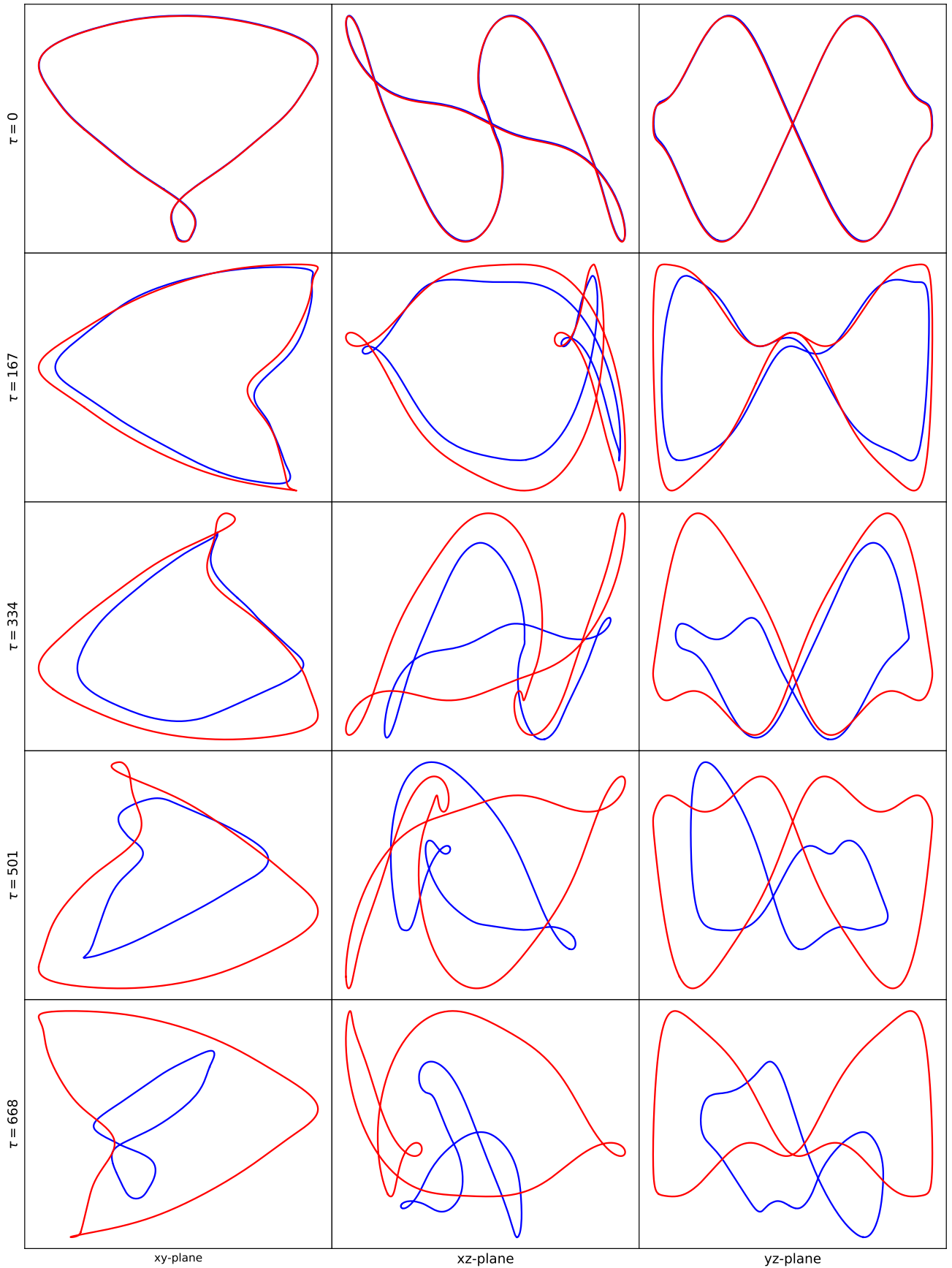
Figure 9.27.: A comparison between a three dimensional evolved string in blue with $m_A = 0.4$ and $n_x = 1024$ and the Nambu-Goto string in red for different times. We show from left to right, the xy, xz, and yz-plane. Starting from the top at time $\tau = 0$ in steps of 167 to $\tau = 668$.

Chapter 10

Conclusion and Outlook

The axion is a very well motivated dark matter candidate, which was originally postulated to solve the strong CP problem. Numerically determining the axion mass, by considering topological defects, is a major challenge due to the string tension problem. In this thesis, we predicted the axion mass, by performing numerical simulations, which overcomes the string tension problem. Additionally, we investigated microscopic string behavior and invented a novel method to construct Nambu-Goto strings on the lattice and compared the evolution with the expected solution for the first time.

In order to overcome the string tension problem, we developed the two-Higgs method, which introduces two scalar fields and one gauge field, where scalar fields have different charges $q_1 \neq q_2$. The remaining phase difference, which is invariant under gauge transformation, represents a global Goldstone-boson mode, which can be identified as the axion.
By adjusting the charges, the desired value for the string tension can be reached. With this new approach, it was possible to determine the axion mass for the first time at the correct string tension assuming that the entire dark matter consists of axions. The determined mass is $m_a = 26.2(34)\mu$eV and was achieved by using a lattice volume $V = 2048 \times 2016 \times 2000$. A recent publication finds a similar result for the axion mass for the same cosmological scenario but with a different approach. Experimental setups are planned to search in this mass range in the near future, to hopefully confirm the existence of the axion. Since most of the designed experimental setups for direct axion detection, which are capable to reach this mass range, rely on resonators. A sufficiently precise prediction, as it was given in the present work, is needed, as resonators can reach the desired sensibility on a narrow frequency band only.
In our simulation, strings break up into loops and then annihilate. This happens in a way, which does not produce as many axions as expected. However, these expectations treat all three production contributions, which are strings, domain walls and the misalignment mechanism, separately, which then leads to double counting. Nevertheless, to better understand this behavior, a deeper investigation of microscopic strings was necessary. To this end, we simulated string dynamics on a lattice, where a single string was needed and the string length-to-thickness ratio was enhanced.
This was done by applying two different, new methods. The first one takes a single string out of a running simulation and refines the mesh to increase the number of lattice points. The string thickness is then changed adiabatically to increase the length-to-thickness ratio. The second method constructs a single string by using the Nambu-Goto solution for flat space. The string length-to-thickness ratio is, in this case, a choice of parameters, which are entered at the beginning of the construction.
The desired global or two-Higgs strings have long range interactions, and it is not known how to apply these methods. However, global and local strings should behave, in the large scale limit, quite similar. Therefore we have applied these methods to local strings. The goal is to investigate the lifetime of the microscopic string, to see whether the numerical simulations are in the large scale limit.
Using local strings has the advantage that, for the constructed string, the trajectory can be compared with the well known Nambu-Goto loop solution. It is assumed that a string with a very large string length-to-thickness ratio has a long lifetime. These strings should then be in the Nambu-Goto limit. To achieve this, we used lattices up to volumes $V = 1600^3$ for the first method. For the second method, we went up to $V = 1024^3$.
Repeating the first method multiple times on the same string shows an increasing lifetime but not as

much as it is expected, if we are in the Nambu-Goto limit. For the second method, we constructed a string which has no self-intersections, cusps or kinks. Such a string constructed in that way should live forever. For different string length-to-thickness ratios the strings follows the theoretical description for a short time, but their lifetimes do not improve much. These strings are far away from the theoretically predicted Nambu-Goto limit.

Overall, there are some remaining open questions to be solved.

First of all, the two-Higgs method requires simulations with larger boxes to study larger mt_* values, and therefore more RAM is needed. A more rigorous way of setting the initial network density and a deeper understanding of the approach to network scaling would be desirable. Also, it is still not clear how efficiently the resulting small loops turn their energy into axions.

The studied microscopic strings do not seem to increase their lifetime by much if the string length-to-thickness ratio is increased. This is clearly in contrast to the expected behavior of the Nambu-Goto limit. The open question is, whether we are just far away from the expected Nambu-Goto limit and need *only* larger lattices, to improve our results, or are there other unknown effects, which influence the string networks and are preventing the strings to reach the Nambu-Goto limit? However, these methods can be applied to global and two-Higgs strings if one finds a way to treat the fields correctly outside the string core. Having done that would enable us to infer more of the axion production from small string loops.

Chapter A

Large Volume Limit

Here we detail some tests which have little bearing on the extrapolation to a final result, and which we have therefore not put in the main development.

In the main text we spend some effort considering when to stop the growth of $\chi(T)$. But we do not discuss when to measure the axion number, arguing only that it is sufficient to measure after the string network is gone and only small fluctuations remain. Here we justify this claim. Figure A.1 shows what happens when we measure the axion number before the string network has finished collapsing. The figure shows the density of strings in blue, and the density of axions, as measured at the indicated time, in black. This measurement is somewhat ambiguous because it involves identifying the axion angle $\theta_a \in [-\pi, \pi]$ which is discontinuous across domain walls. Such a discontinuity leads to "ringing" in the Fourier spectrum and formally gives a logarithmically UV divergent particle number (cut off by lattice effects). We "fix" this problem by truncating the largest θ_a values, reflecting $\theta_a \in [\pi/2, \pi]$ to $\theta_a \to \pi - \theta_a$, and similarly for $\theta_a \in [-\pi, -\pi/2]$. Despite this "cap" on the maximum size of $|\theta_a| < \pi/2$, we nevertheless find a very large axion density if we measure axions before the network has decayed. However, we see that after the strings are gone, the axion number becomes completely independent of further time evolution. Our "cap" on large θ_a values has no effect on this final plateau, because $|\theta_a| > \pi/2$ virtually never happens and represents a tiny fraction of the axion number. In light of this result, we generally measure n_{ax} as soon as no strings remain, but when we evolve for longer and remeasure later, we get an answer which agrees at the 1% level. If we repeat this analysis for the misalignment scenario, we find that instead of becoming virtually t-independent at $t = 4t_*$, the axion number becomes virtually t-independent already by $t = 2t_*$. This difference reflects the absence of topological structures in the misalignment scenario.

The other test which proves to play almost no role in the final axion density is the box volume. Theoretically, we know that in a simulation which runs for a conformal time t, information can propagate at most a distance t, so a box $L \geq 2t$ on a side will have vanishing volume systematics (in the sense that the ensemble average of axion production efficiency in such boxes will have vanishing L-dependence as L is made larger than this value; of course one specific box will have statistical fluctuations about this average). In fact we expect that the situation is better. It has been shown [133] that local string evolution only propagates information at about half this speed. And although the axion also propagates between strings, it becomes massive fairly early in the simulation history, and should also propagate information substantially slower than light speed. Therefore a box with $L \geq t$ should be sufficient. Since we find the string network is gone and axion number can be measured at $t \simeq 4t_*$, this requires $L \geq 4t_*$.

It seems safest to test this argument, and to see how the finite volume effects begin to manifest themselves as L is made smaller. For numerical efficiency, we have done so using the rather small value of $mt_* = 200$. Keeping everything else besides the volume unchanged, we find in Figure A.2 that the volume has less than a $< 2\%$ effect on the axion abundance down to a box length of $Lt_* = 2$.

The smallest volume shown, $L = 1.28t_*$, shows a larger generated axion number, with larger statistical fluctuations (we used more simulations for smaller volumes so the total volume sampled is about the same for each data point). The reason is that, in a small fraction of small-L simulations, after all strings annihilate, there remains a domain wall stretching across the whole box. This domain wall is metastable and lasts indefinitely, until it dominates the axion number. This is purely a small volume artifact; nothing of the sort ever occurs for the larger volumes.
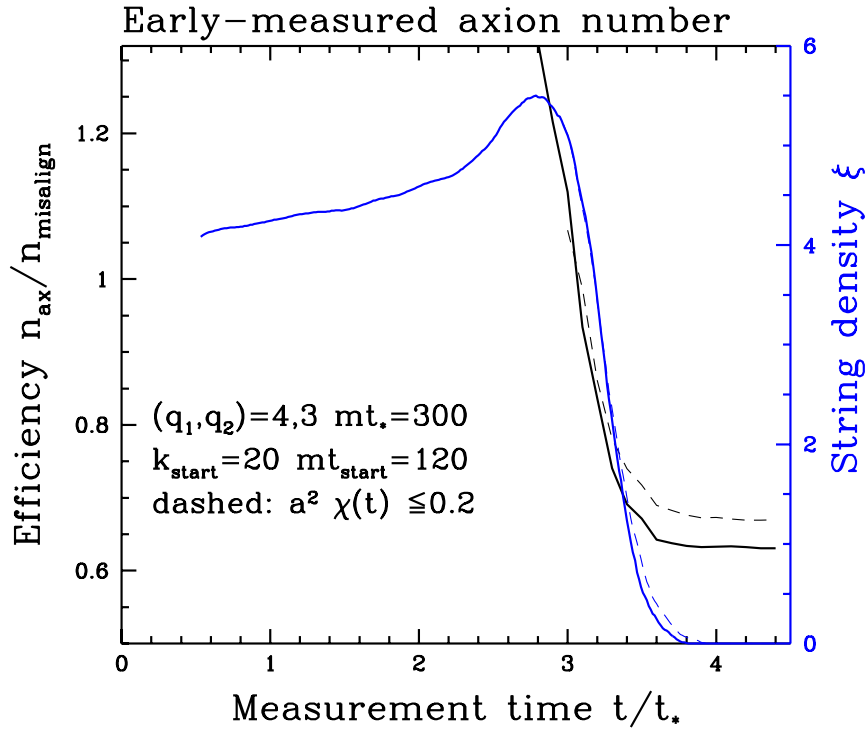
Figure A.1.: Blue: scaled string density ξ as a function of time. Black: instantaneously measured axion number at the same time. Dashed lines are for an evolution with an upper cutoff on $\chi(T)$ at $\chi(T) < m^2/5$.
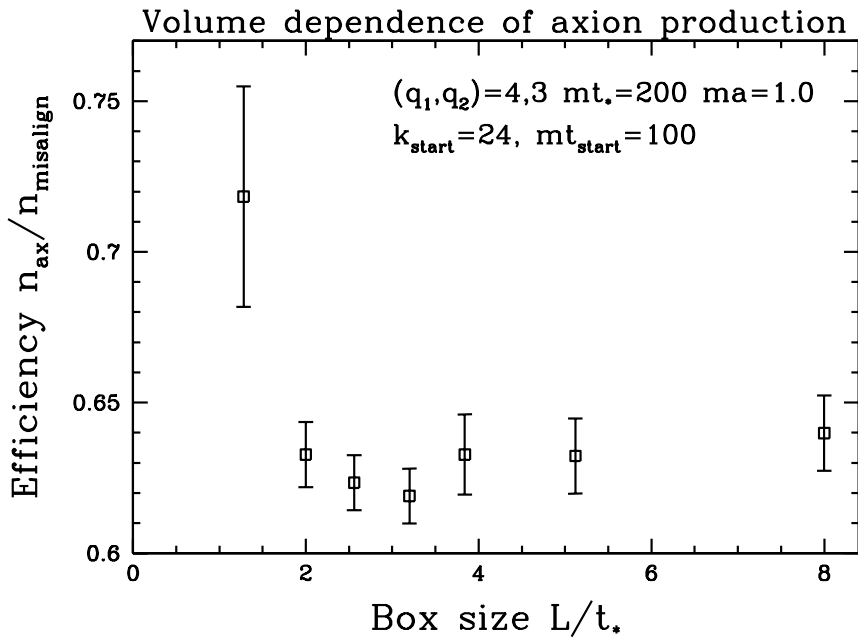

Figure A.2.: Study of box volume dependence of the axion production rate. Except for the smallest volume, it appears the result shows extremely weak volume dependence.

Because the volume dependence is so mild, it should be possible to study the axion production in boxes down to $Lt_* = 2$ or 3. However, to be conservative, we have generally tried to keep $Lt_* \geq 5$.

Chapter B

Plaquette Handling

Initializing the vacuum for the Nambu-Goto field string method needs a consistent handling of the plaquettes gauge fields. A link is connected to four plaquettes, therefore it is important to respect the order of summing up the gauge fields. Otherwise we will not find a true minimum and will always have artifacts in our vacuum. The reference point is (0,0,0), where x,y,z denotes the direction of the link. Note that the link is living in between of two field points but is labeled as it would live on the field point, therefore $(0,0,0)_x$ is the link between the points $(0,0,0)$ and $(1,0,0)$. The following pictures show the link we would like to minimize using the magnetic fields.
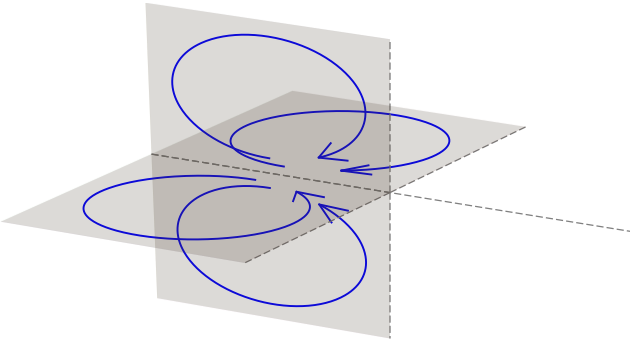
- $A_{(0,0,0),x}$
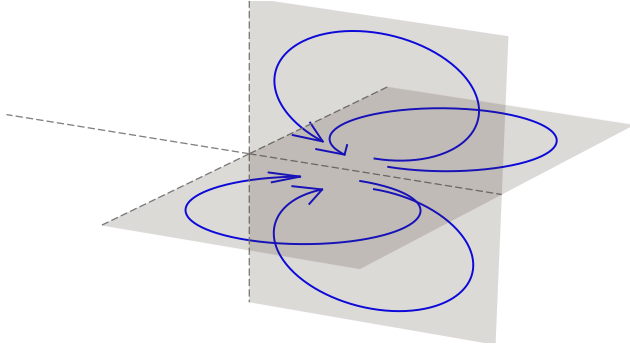
$$B_y = A_{(0,0,0),x} + A_{(1,0,0),z} - A_{(0,0,1),x} - A_{(0,0,0),z}$$
$$B_y = A_{(0,0,0),x} + A_{(1,0,-1),z} - A_{(0,0,-1),x} - A_{(0,0,-1),z}$$
$$B_z = A_{(0,0,0),x} + A_{(1,0,0),y} - A_{(0,1,0),x} - A_{(0,0,0),y}$$
$$B_z = A_{(0,0,0),x} + A_{(1,-1,0),y} - A_{(0,-1,0),x} - A_{(0,-1,0),y}$$
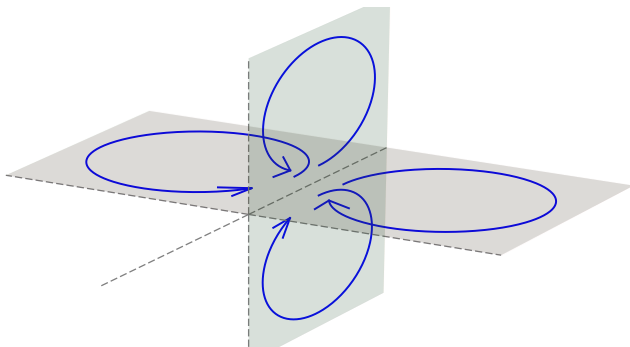
- $A_{(-1,0,0),x}$

$$B_y = A_{(-1,0,0),x} + A_{(-1,0,0),z} - A_{(-1,0,1),x} - A_{(0,0,0),z}$$
$$B_y = A_{(-1,0,0),x} + A_{(-1,0,-1),z} - A_{(-0,0,-1),x} - A_{(0,0,-1),z}$$
$$B_z = A_{(-1,0,0),x} + A_{(-1,0,0),y} - A_{(-1,1,0),x} - A_{(0,0,0),y}$$
$$B_z = A_{(-1,0,0),x} + A_{(-1,-1,0),y} - A_{(-1,-1,0),x} - A_{(0,-1,0),y}$$
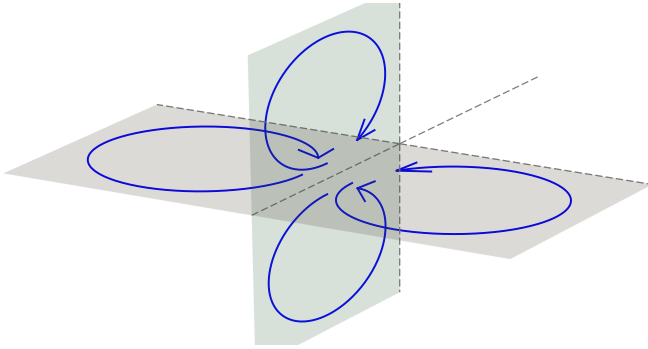
- $A_{(0,0,0),y}$

$$B_x = A_{(0,0,0),y} + A_{(0,1,0),z} - A_{(0,0,1),y} - A_{(0,0,0),z}$$
$$B_x = A_{(0,0,0),y} + A_{(0,1,-1),z} - A_{(0,0,-1),y} - A_{(0,0,-1),z}$$
$$B_z = A_{(0,0,0),y} + A_{(0,1,0),x} - A_{(0,1,0),y} - A_{(0,0,0),x}$$
$$B_z = A_{(0,0,0),y} + A_{(-1,1,0),x} - A_{(-1,0,0),y} - A_{(-1,0,0),x}$$
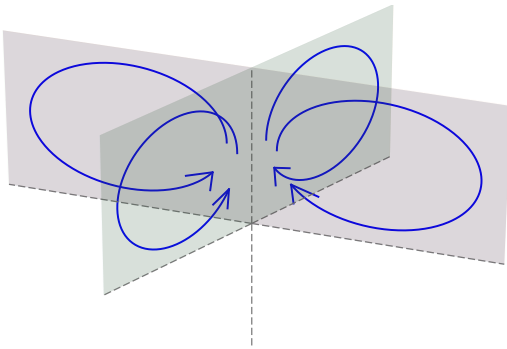
- $A_{(0,-1,0),y}$

$$B_x = A_{(0,-1,0),y} + A_{(0,-1,0),z} - A_{(0,-1,1),y} - A_{(0,0,0),z}$$
$$B_x = A_{(0,-1,0),y} + A_{(0,-1,-1),z} - A_{(0,-1,-1),y} - A_{(0,0,-1),z}$$
$$B_z = A_{(0,-1,0),y} + A_{(0,-1,0),x} - A_{(1,-1,0),y} - A_{(0,0,0),x}$$
$$B_z = A_{(0,-1,0),y} + A_{(-1,-1,0),x} - A_{(-1,-1,0),y} - A_{(-1,0,0),x}$$

- $A_{(0,0,0),z}$

$$B_y = A_{(0,0,0),z} + A_{(0,0,1),x} - A_{(1,0,0),z} - A_{(0,0,0),x}$$
$$B_y = A_{(0,0,0),z} + A_{(-1,0,1),x} - A_{(-1,0,0),z} - A_{(-1,0,0),x}$$
$$B_x = A_{(0,0,0),z} + A_{(0,0,1),y} - A_{(0,1,0),z} - A_{(0,0,0),y}$$
$$B_x = A_{(0,0,0),z} + A_{(0,-1,1),y} - A_{(0,-1,0),z} - A_{(0,-1,0),y}$$
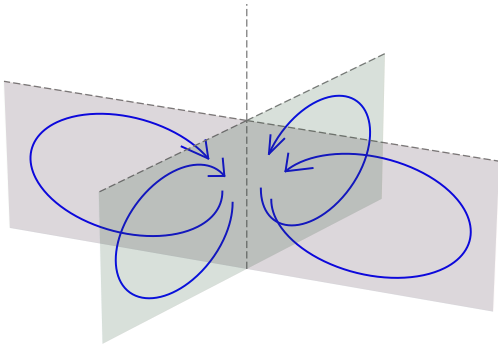
- $A_{(0,0,-1),z}$

$$B_y = A_{(0,0,-1),z} + A_{(0,0,-1),x} - A_{(-1,0,-1),z} - A_{(0,0,0),x}$$
$$B_y = A_{(0,0,-1),z} + A_{(-1,0,-1),x} - A_{(-1,0,-1),z} - A_{(-1,0,0),x}$$
$$B_x = A_{(0,0,-1),z} + A_{(0,0,-1),y} - A_{(0,-1,-1),z} - A_{(0,0,0),y}$$
$$B_x = A_{(0,0,-1),z} + A_{(0,-1,-1),y} - A_{(0,-1,-1),z} - A_{(0,-1,0),y}$$

B. Plaquette Handling

Chapter C

Frenet Serret Formula

The Frenet-Serret formulas are the central formalism of space curves, which will be introduced for the 3D case [134]. The formalism has an orthonormal basis which is build up by the tangential $\vec{t}(s)$, the normal $\vec{n}(s)$ and the binormal-vector $\vec{b}(s)$. These vectors describe the local behavior of the curvature $\vec{r}(s)$ with the curvature $\kappa(s)$ and the torsion $\tau(s)$, where s denotes the position on the curve. The derivative of the basis vectors are linear combinations of the basis vectors and the scalar parameters itself, therefore the Frenet-Serret formulas are expressed by

$$\frac{d\vec{r}(s)}{ds} = \vec{t}, \tag{C.0.1}$$

$$\frac{d\vec{t}}{ds} = \kappa\vec{n}, \tag{C.0.2}$$

$$\vec{t} \times \vec{n} = \vec{b}, \tag{C.0.3}$$

$$\frac{d\vec{b}}{ds} = -\tau\vec{n}, \tag{C.0.4}$$

$$\frac{d\vec{n}}{ds} = \tau\vec{b} - \kappa\vec{t}. \tag{C.0.5}$$

The curvature and the torsion can be described by

$$\kappa = \frac{|\dot{\vec{r}}(s) \times \ddot{\vec{r}}(s)|}{|\dot{\vec{r}}(s)|^3}, \tag{C.0.6}$$

$$\tau = \frac{(\dot{\vec{r}}(s) \times \ddot{\vec{r}}(s)) \cdot \dddot{\vec{r}}(s)}{|\dot{\vec{r}}(s) \times \ddot{\vec{r}}(s)|^2}. \tag{C.0.7}$$

In case for a Nambu-Goto string, we can identify $\vec{x}(\sigma, t)$ as $\vec{r}(s)$ and the tangential component $\vec{x}'(\sigma, t)$ as $\vec{t}(s)$.

Chapter D

Radius of Osculating Sphere

To ensure that the string core does not overlap with its own field points, we have to calculate the curvature radius, which is defined as:

$$r = \frac{1}{\kappa}.$$ (D.0.1)

To be more precise we actually have to calculate the osculating sphere of the trajectory, which is defined as:

$$r = \sqrt{\frac{1}{\kappa^2} + \frac{\kappa'^2}{\kappa\tau}}$$ (D.0.2)

The calculation for the osculating sphere is very intensive to implement as we can see from Eq. (D.0.6)

$$r_{min} = \frac{1}{\kappa} \leq \sqrt{\frac{1}{\kappa^2} + \frac{\kappa'^2}{\kappa\tau}}$$ (D.0.3)

Therefore we ensure by using the curvature radius, that the tube size always will be small enough in comparison to the smallest radius of the curve. We see by expressing the equations to their full form seen in Eq. (D.0.6) that the difference of the curvature radius compared to the radius of the osculating sphere is much more effort to implement.

$$\kappa[t] = \frac{\sqrt{\left(x_0'(t)x_1''(t) - x_1'(t)x_0''(t)\right)^2 + \left(x_2'(t)x_0''(t) - x_0'(t)x_2''(t)\right)^2 + \left(x_1'(t)x_2''(t) - x_2'(t)x_1''(t)\right)^2}}{\left(x_0'(t)^2 + x_1'(t)^2 + x_2'(t)^2\right)^{3/2}} \tag{D.0.4}$$

$$\tau[t] = \frac{x_0^{(3)}(t)\left(x_1'(t)x_2''(t) - x_2'(t)x_1''(t)\right) + x_1^{(3)}(t)\left(x_2'(t)x_0''(t) - x_0'(t)x_2''(t)\right) + x_1^{(3)}(t)\left(x_2'(t)x_0''(t) - x_0'(t)x_2''(t)\right)^2 + \left(x_1'(t)x_2''(t) - x_2'(t)x_1''(t)\right)^2}{\left(x_0'(t)x_1''(t) - x_1'(t)x_0''(t)\right)^2 + \left(x_2'(t)x_0''(t) - x_0'(t)x_2''(t)\right)^2} \tag{D.0.5}$$

$$+ \frac{x_2^{(3)}(t)\left(x_0'(t)x_1''(t) - x_1'(t)x_0''(t)\right)}{\left(x_0'(t)x_1''(t) - x_1'(t)x_0''(t)\right)^2 + \left(x_2'(t)x_0''(t) - x_0'(t)x_2''(t)\right)^2 + \left(x_1'(t)x_2''(t) - x_2'(t)x_1''(t)\right)^2}$$

$$r[t]^2 = \frac{\left(x_0'(t)^2 + x_1'(t)^2 + x_2'(t)^2\right)^6}{\left(x_0^{(3)}(t)\left(x_1'(t)x_2''(t) - x_2'(t)x_1''(t)\right) + x_1^{(3)}(t)\left(x_2'(t)x_0''(t) - x_0'(t)x_2''(t)\right) + x_2^{(3)}(t)\left(x_0'(t)x_1''(t) - x_1'(t)x_0''(t)\right)\right)^2} \tag{D.0.6}$$

$$\times \frac{\left(\dfrac{2\left(x_1^{(3)}(t)x_0'(t) - x_0^{(3)}(t)x_1'(t)\right)\left(x_0'(t)x_1''(t) - x_1'(t)x_0''(t)\right) + 2\left(x_0^{(3)}(t)x_2'(t) - x_2^{(3)}(t)x_0'(t)\right)\left(x_2'(t)x_0''(t) - x_0'(t)x_2''(t)\right) + 2\left(x_2^{(3)}(t)x_1'(t) - x_1^{(3)}(t)x_2'(t)\right)\left(x_1'(t)x_2''(t) - x_2'(t)x_1''(t)\right)}{2\left(x_0'(t)^2 + x_1'(t)^2 + x_2'(t)^2\right)^{3/2}\sqrt{\left(x_0'(t)x_1''(t) - x_1'(t)x_0''(t)\right)^2 + \left(x_2'(t)x_0''(t) - x_0'(t)x_2''(t)\right)^2 + \left(x_1'(t)x_2''(t) - x_2'(t)x_1''(t)\right)^2}} - \dfrac{3\left(2x_0'(t)x_0''(t) + 2x_1'(t)x_1''(t) + 2x_2'(t)x_2''(t)\right)\sqrt{\left(x_0'(t)x_1''(t) - x_1'(t)x_0''(t)\right)^2 + \left(x_2'(t)x_0''(t) - x_0'(t)x_2''(t)\right)^2 + \left(x_1'(t)x_2''(t) - x_2'(t)x_1''(t)\right)^2}}{2\left(x_0'(t)^2 + x_1'(t)^2 + x_2'(t)^2\right)^{5/2}} \right)^2}{\dfrac{\left(x_0^{(3)}(t)\left(x_1'(t)x_2''(t) - x_2'(t)x_1''(t)\right) + x_1^{(3)}(t)\left(x_2'(t)x_0''(t) - x_0'(t)x_2''(t)\right) + x_2^{(3)}(t)\left(x_0'(t)x_1''(t) - x_1'(t)x_0''(t)\right)\right)^2}{\left(x_0'(t)^2 + x_1'(t)^2 + x_2'(t)^2\right)^3}}$$

$$+ \left(x_0'(t)x_1''(t) - x_1'(t)x_0''(t)\right)^2 + \left(x_2'(t)x_0''(t) - x_0'(t)x_2''(t)\right)^2 + \left(x_1'(t)x_2''(t) - x_2'(t)x_1''(t)\right)^2$$

Chapter E

Loop Solutions

We will present here a small set of loop solutions of the Nambu-Goto equation, with different properties. As defined in chapter 6 the left and right moving parts can be parametrized by $\xi = \frac{2\pi}{L}(\sigma + t)$ and $\eta = \frac{2\pi}{L}(\sigma - t)$. The solution of the equation of motion is $x(\sigma, t) = \frac{a-b}{2}$ with $\dot{x}(\sigma, t) = \frac{a'+b'}{2}$ and $x'(\sigma, t) = \frac{a'-b'}{2}$.

- **Cuspless ⊠; Kinkless □; non self-intersecting ⊠** [135]

$$a' = \begin{bmatrix} \sin(p\xi + \alpha) \\ \cos(p\xi + \alpha) \\ 0 \end{bmatrix} \qquad b' = \begin{bmatrix} \sin(q\eta + \beta)\cos(\Psi) \\ \sin(q\eta + \beta)\sin(\Psi) \\ \sin(q\eta + \beta) \end{bmatrix} \tag{E.0.1}$$

Where p, q, Ψ are constants and

$$\alpha = \pi(1-p)\left[\frac{\xi}{\pi}\right] \qquad \beta = \pi(1-q)\left[\frac{\eta}{\pi}\right] + \delta. \tag{E.0.2}$$

For $\delta = \pi(2-q)/2$ the loop will not have any cusp and $[x]$ is the greatest integer less than or equal to x.

- **Cuspless □; Kinkless ⊠; non self-intersecting ⊠** [99]

$$a' = \begin{bmatrix} \frac{1}{2}\left((1-\alpha)\cos(\xi) + \frac{\alpha}{3}\cos(3\xi)\right) \\ \frac{1}{2}\left((1-\alpha)\sin(\xi) + \frac{\alpha}{3}\sin(3\xi)\right) \\ \sqrt{\alpha(1-\alpha)}\sin(\xi) \end{bmatrix} \qquad b' = \begin{bmatrix} \frac{\cos(\eta)}{2} \\ \frac{\sin(\eta)}{2} \\ 0 \end{bmatrix} \tag{E.0.3}$$

For $0 < \alpha < 1$ the string never self-intersects.

- **Cuspless ⊠; Kinkless ⊠; non self-intersecting □** [135]

$$a' = \begin{bmatrix} \frac{2(p^2+1)^2\cos 2\xi + p^2\cos 4\xi}{(p^2+2)(2p^2+1)} \\ \frac{2\sqrt{2}p\left((p^2+2)\sin\xi + \sin 3\xi\right)}{(p^2+2)(2p^2+1)} \\ \frac{(2(p^2+1)^2-4)\sin 2\xi + p^2\sin 4\xi}{(p^2+2)(2p^2+1)} \end{bmatrix} \qquad b' = \begin{bmatrix} \frac{2(p^2+1)^2\cos 2\eta + p^2\cos 4\eta}{(p^2+2)(2p^2+1)} \\ -\frac{(2(p^2+1)^2-4)\sin 2\eta + p^2\sin 4\eta}{(p^2+2)(2p^2+1)} \\ -\frac{2\sqrt{2}p\left((p^2+2)\sin\eta + \sin 3\eta\right)}{(p^2+2)(2p^2+1)} \end{bmatrix} \tag{E.0.4}$$

If $p \sim 1$ these equations describe cuspless loops.

- **Cuspless ⊠; Kinkless ⊠; non self-intersecting ⊠**

$$a' = \begin{bmatrix} \cos(\xi)\sqrt{1-a_z^2} \\ \sin(\xi)\sqrt{1-a_z^2} \\ \frac{3}{4}\cos(2(\xi)) \end{bmatrix} \qquad b' = \begin{bmatrix} \sqrt{\frac{8}{9}}\sin(2(\eta))\sqrt{1 + 8\cos^6(2(\eta))} \\ 0 \\ -(\frac{2}{3}\cos(4(\eta)) + \frac{1}{3}\cos(8(\eta))) \end{bmatrix} \tag{E.0.5}$$

Bibliography

[1] Chung-Pei Ma, RR Caldwell, Paul Bode, and Limin Wang, *The mass power spectrum in quintessence cosmological models*, The Astrophysical Journal Letters **521**, L1 (1999).

[2] N Aghanim, Y Akrami, M Ashdown, J Aumont, C Baccigalupi, M Ballardini, AJ Banday, RB Barreiro, N Bartolo, S Basak, *et al.*, *Planck 2018 results. vi. cosmological parameters*, arXiv preprint arXiv:1807.06209 (2018).

[3] Cliff Burgess and Guy Moore, *The standard model: A primer*. Cambridge University Press, 2006.

[4] Pierre Sikivie, *Axion cosmology*, in *Axions*, pp. 19–50. Springer, 2008.

[5] R. D. Peccei and H. R. Quinn, *Constraints imposed by cp conservation in the presence of pseudoparticles*, Physical Review D **16**, 1791 (1977).

[6] Albert Einstein, *Lens-like action of a star by the deviation of light in the gravitational field*, Science **84**, 506 (1936).

[7] John Archibald Wheeler, *Einsteins vision*. Springer-Verlag Berlin, 1968.

[8] Arthur Stanley Eddington, *The propagation of gravitational waves*, Proceedings of the Royal Society of London. Series A, Containing Papers of a Mathematical and Physical Character **102**, 268 (1922).

[9] Saul Perlmutter, Michael S Turner, and Martin White, *Constraining dark energy with type ia supernovae and large-scale structure*, Physical Review Letters **83**, 670 (1999).

[10] H Poincare, *The milky way and the theory of gases*, Popular Astronomy **14**, 475 (1906).

[11] E Margaret Burbidge, Geoffrey Ronald Burbidge, and Vera C Rubin, *A study of the velocity field in m 82 and its bearing on explosive phenomena in that galaxy*, .

[12] Georges Aad, Tatevik Abajyan, B Abbott, J Abdallah, S Abdel Khalek, Ahmed Ali Abdelalim, O Abdinov, R Aben, B Abi, M Abolins, *et al.*, *Observation of a new particle in the search for the standard model higgs boson with the atlas detector at the lhc*, Physics Letters B **716**, 1 (2012).

[13] Wilfried Buchmüller, Pasquale Di Bari, and Michael Plümacher, *Cosmic microwave background, matter–antimatter asymmetry and neutrino masses*, Nuclear Physics B **643**, 367 (2002).

[14] Arnold Hanslmeier, *Einführung in Astronomie und Astrophysik*. Springer, 2002.

[15] Timothy D Brandt, *Constraints on macho dark matter from compact stellar systems in ultra-faint dwarf galaxies*, The Astrophysical Journal Letters **824**, L31 (2016).

[16] Gerard Jungman, Marc Kamionkowski, and Kim Griest, *Supersymmetric dark matter*, Physics Reports **267**, 195 (1996).

[17] Steven Weinberg, *A New Light Boson?*, Phys.Rev.Lett. **40**, 223 (1978).

[18] Gerard 't Hooft, *Computation of the Quantum Effects Due to a Four-Dimensional Pseudoparticle*, Phys.Rev. **D14**, 3432 (1976).

[19] Makoto Kobayashi and Toshihide Maskawa, *Cp-violation in the renormalizable theory of weak interaction*, Progress of Theoretical Physics **49**, 652 (1973).

[20] JM Pendlebury, S Afach, NJ Ayres, CA Baker, G Ban, Georg Bison, Kazimierz Bodek, Martin Burghoff, Peter Geltenbort, Katie Green, *et al.*, *Revised experimental upper limit on the electric dipole moment of the neutron*, Physical Review D **92**, 092003 (2015).

[21] R.D. Peccei and Helen R. Quinn, *CP Conservation in the Presence of Instantons*, Phys.Rev.Lett. **38**, 1440 (1977).

[22] Jihn E Kim, *Light pseudoscalars, particle physics and cosmology*, Physics Reports **150**, 1 (1987).

[23] John Preskill, Mark B. Wise, and Frank Wilczek, *Cosmology of the Invisible Axion*, Phys. Lett. **B120**, 127 (1983).

[24] Leesa Fleury and Guy D. Moore, *Axion dark matter: strings and their cores*, Journal of Cosmology and Astroparticle Physics **2016**, 004 (2016), [`1509.00026`].

[25] Leesa M. Fleury and Guy D. Moore, *Axion String Dynamics I: 2+1D*, JCAP **1605**, 005 (2016), [`1602.04818`].

[26] Masahiro Kawasaki, Ken'ichi Saikawa, and Toyokazu Sekiguchi, *Axion dark matter from topological defects*, Phys.Rev. **D91**, 065014 (2015), [`1412.0789`].

[27] Marco Gorghetto, Edward Hardy, and Giovanni Villadoro, *Axions from strings: the attractive solution*, Journal of High Energy Physics **2018**, 151 (2018).

[28] R. L. Davis and E. P. S. Shellard, *Do Axions Need Inflation?*, Nucl. Phys. **B324**, 167 (1989).

[29] Atish Dabholkar and Jean M. Quashnock, *Pinning Down the Axion*, Nucl. Phys. **B333**, 815 (1990).

[30] C. Hagmann and P. Sikivie, *Computer simulations of the motion and decay of global strings*, Nucl. Phys. **B363**, 247 (1991).

[31] R. A. Battye and E. P. S. Shellard, *Global string radiation*, Nucl. Phys. **B423**, 260 (1994), [`astro-ph/9311017`].

[32] R. A. Battye and E. P. S. Shellard, *Radiative back reaction on global strings*, Phys. Rev. **D53**, 1811 (1996), [`hep-ph/9508301`].

[33] Sanghyeon Chang, C. Hagmann, and P. Sikivie, *Studies of the motion and decay of axion walls bounded by strings*, Phys. Rev. **D59**, 023505 (1999), [`hep-ph/9807374`].

[34] Masahide Yamaguchi, Jun'ichi Yokoyama, and M. Kawasaki, *Numerical analysis of formation and evolution of global strings in (2+1)-dimensions*, Prog. Theor. Phys. **100**, 535 (1998), [`hep-ph/9808326`].

[35] Masahide Yamaguchi, M. Kawasaki, and Jun'ichi Yokoyama, *Evolution of axionic strings and spectrum of axions radiated from them*, Phys. Rev. Lett. **82**, 4578 (1999), [`hep-ph/9811311`].

[36] Masahide Yamaguchi, *Scaling property of the global string in the radiation dominated universe*, Phys. Rev. **D60**, 103511 (1999), [`hep-ph/9907506`].

[37] Masahide Yamaguchi, Jun'ichi Yokoyama, and M. Kawasaki, *Evolution of a global string network in a matter dominated universe*, Phys. Rev. **D61**, 061301 (2000), [`hep-ph/9910352`].

[38] C. Hagmann, Sanghyeon Chang, and P. Sikivie, *Axion radiation from strings*, Phys. Rev. **D63**, 125018 (2001), [`hep-ph/0012361`].

[39] C. J. A. P. Martins, J. N. Moore, and E. P. S. Shellard, *A Unified model for vortex string network evolution*, Phys. Rev. Lett. **92**, 251601 (2004), [`hep-ph/0310255`].

[40] Olivier Wantz and E.P.S. Shellard, *Axion Cosmology Revisited,* Phys.Rev. **D82**, 123508 (2010), [0910.1066].

[41] Takashi Hiramatsu, Masahiro Kawasaki, and Ken'ichi Saikawa, *Evolution of String-Wall Networks and Axionic Domain Wall Problem*, JCAP **1108**, 030 (2011), [1012.4558].

[42] Takashi Hiramatsu, Masahiro Kawasaki, Toyokazu Sekiguchi, Masahide Yamaguchi, and Jun'ichi Yokoyama, *Improved estimation of radiated axions from cosmological axionic strings*, Phys.Rev. **D83**, 123531 (2011), [1012.5502].

[43] Takashi Hiramatsu, Masahiro Kawasaki, Ken'ichi Saikawa, and Toyokazu Sekiguchi, *Production of dark matter axions from collapse of string-wall systems*, Phys.Rev. **D85**, 105020 (2012), [1202.5851].

[44] Takashi Hiramatsu, Masahiro Kawasaki, Ken'ichi Saikawa, and Toyokazu Sekiguchi, *Axion cosmology with long-lived domain walls*, JCAP **1301**, 001 (2013), [1207.3166].

[45] Sz. Borsanyi *et al.*, *Calculation of the axion mass based on high-temperature lattice quantum chromodynamics*, Nature **539**, 69 (2016), [1606.07494].

[46] Michael E Peskin, *An introduction to quantum field theory*. CRC Press, 2018.

[47] Steven Weinberg, *The u (1) problem*, Physical Review D **11**, 3583 (1975).

[48] Frank Wilczek, *Problem of Strong p and t Invariance in the Presence of Instantons*, Phys.Rev.Lett. **40**, 279 (1978).

[49] G't Hooft, *How instantons solve the u (1) problem.*, Physics Reports **142**, 357 (1986).

[50] John S Bell and Roman Jackiw, *A pcac puzzle*, Il Nuovo Cimento A (1965-1970) **60**, 47 (1969).

[51] Thomas Schäfer and Edward V Shuryak, *Instantons in qcd*, Reviews of Modern Physics **70**, 323 (1998).

[52] Varouzhan B., *Cp-nonconserving effects in quantum chromodynamics*, Physical Review D **19**, 2227 (1979).

[53] Jack Dragos, Thomas Luu, Andrea Shindler, Jordy de Vries, and Ahmed Yousif, *Confirming the existence of the strong cp problem in lattice qcd with the gradient flow*, arXiv preprint arXiv:1902.03254 (2019).

[54] S. Yu Khlebnikov and M.E. Shaposhnikov, *Extra space-time dimensions: Towards a solution to the strong cp-problem*, Physics Letters B **203**, 121 (1988).

[55] G. Schierholz, *Towards a dynamical solution of the strong cp problem*, Nuclear Physics B-Proceedings Supplements **37**, 203 (1994).

[56] H. Georgi, *Model of soft cp violation*, Hadronic J.;(United States) **1**, (1978).

[57] David J. Gross, Robert D. Pisarski, and Laurence G. Yaffe, *QCD and Instantons at Finite Temperature*, Rev. Mod. Phys. **53**, 43 (1981).

[58] Giovanni Grilli di Cortona, Edward Hardy, Javier Pardo Vega, and Giovanni Villadoro, *The QCD axion, precisely*, JHEP **01**, 034 (2016), [1511.02867].

[59] Marco Gorghetto and Giovanni Villadoro, *Topological susceptibility and qcd axion mass: Qed and nnlo corrections*, Journal of High Energy Physics **2019**, 33 (2019).

[60] Michael S. Turner, *Cosmic and Local Mass Density of Invisible Axions*, Phys. Rev. **D33**, 889 (1986).

[61] P Thomas Jahn, Guy D Moore, and Daniel Robaina, *Topological susceptibility to high temperatures via reweighting*, arXiv preprint arXiv:1810.13218 (2018).

[62] W. A. Bardeen, R. D. Peccei, and T. Yanagida, *Constraints on variant axion models*, Nuclear Physics B **279**, 401 (1987).

[63] J. E. Kim, *Weak-interaction singlet and strong cp invariance*, Physical Review Letters **43**, 103 (1979).

[64] M. A. Shifman, A.I. Vainshtein, and V.I. Zakharov, *Can confinement ensure natural cp invariance of strong interactions?*, Nuclear Physics B **166**, 493 (1980).

[65] M. Dine, W. Fischler, and M. Srednicki, *A simple solution to the strong cp problem with a harmless axion*, Physics letters B **104**, 199 (1981).

[66] A.R. Zhitnitskij, *On possible suppression of the axion-hadron interactions*, .

[67] R. D. Peccei, *The strong cp problem and axions*, in *Axions*, pp. 3–17. Springer, 2008.

[68] Igor G Irastorza and Javier Redondo, *New experimental approaches in the search for axion-like particles*, Progress in Particle and Nuclear Physics **102**, 89 (2018).

[69] Guido Mueller, Pierre Sikivie, DB Tanner, and Karl van Bibber, *Detailed design of a resonantly enhanced axion-photon regeneration experiment*, Physical Review D **80**, 072004 (2009).

[70] R Ballou, G Deferne, M Finger Jr, M Finger, L Flekova, J Hosek, S Kunc, K Macuchova, KA Meissner, P Pugnat, *et al.*, *New exclusion limits on scalar and pseudoscalar axionlike particles from light shining through a wall*, Physical Review D **92**, 092002 (2015).

[71] E Armengaud, FT Avignone, M Betz, P Brax, P Brun, Giovanni Cantatore, JM Carmona, GP Carosi, F Caspers, S Caspi, *et al.*, *Conceptual design of the international axion observatory (iaxo)*, Journal of Instrumentation **9**, T05002 (2014).

[72] V Anastassopoulos, S Aune, K Barth, A Belov, H Bräuninger, Giovanni Cantatore, JM Carmona, JF Castel, SA Cetin, F Christensen, *et al.*, *New cast limit on the axion–photon interaction*, Nature Physics **13**, 584 (2017).

[73] Allen Caldwell, Gia Dvali, Béla Majorovits, Alexander Millar, Georg Raffelt, Javier Redondo, Olaf Reimann, Frank Simon, Frank Steffen, MADMAX Working Group, *et al.*, *Dielectric haloscopes: a new way to detect axion dark matter*, Physical review letters **118**, 091801 (2017).

[74] Ian Stern, *Admx status*, arXiv preprint arXiv:1612.08296 (2016).

[75] Dieter Horns, Joerg Jaeckel, Axel Lindner, Javier Redondo, Andreas Ringwald, *et al.*, *Searching for wispy cold dark matter with a dish antenna*, Journal of Cosmology and Astroparticle Physics **2013**, 016 (2013).

[76] B Majorovits *et al.*, *Madmax: A new road to axion dark matter detection*, arXiv preprint arXiv:1712.01062 (2017).

[77] Alexander Friedman, *Über die krümmung des raumes*, Zeitschrift für Physik A Hadrons and Nuclei **10**, 377 (1922).

[78] Georges Lemaître, *Expansion of the universe, the expanding universe*, Monthly Notices of the Royal Astronomical Society **91**, 490 (1931).

[79] Arthur Geoffrey Walker, *On milne's theory of world-structure*, Proceedings of the London Mathematical Society **2**, 90 (1937).

[80] A. Vilenkin and E.P.S. Shellard, *Cosmic Strings and Other Topological Defects*. Cambridge Monographs on Mathematical Physics. Cambridge University Press, 2000.

[81] O. Wantz and E.P.S. Shellard, *Axion cosmology revisited*, Physical Review D **82**, 123508 (2010).

[82] Steven Weinberg, *Gravitation and cosmology: principles and applications of the general theory of relativity*, vol. 1. Wiley New York, 1972.

[83] L.F. Abbott and P. Sikivie, *A cosmological bound on the invisible axion*, Physics Letters B **120**, 133 (1983).

[84] S. Borsanyi, M. Dierigl, Z. Fodor, S. D. Katz, S. W. Mages, D. Nogradi, J. Redondo, A. Ringwald, and K. K. Szabo, *Axion cosmology, lattice QCD and the dilute instanton gas*, Phys. Lett. **B752**, 175 (2016), [1508.06917].

[85] Barton Zwiebach, *A first course in string theory*. Cambridge university press, 2004.

[86] Kei-ichi Maeda and Neil Turok, *Finite-width corrections to the nambu action for the nielsen-olesen string*, Physics Letters B **202**, 376 (1988).

[87] Michael Kalb and Pierre Ramond, *Classical direct interstring action*, Phys. Rev. **D9**, 2273 (1974).

[88] Alexander Vilenkin and Tanmay Vachaspati, *Radiation of Goldstone Bosons From Cosmic Strings*, Phys. Rev. **D35**, 1138 (1987).

[89] EB Bogomol'Nyi, *The stability of classical solutions*, Sov. J. Nucl. Phys.(Engl. Transl.);(United States) **24**, (1976).

[90] Holger Bech Nielsen and Poul Olesen, *Vortex-line models for dual strings*, Nuclear Physics B **61**, 45 (1973).

[91] Laurence Jacobs and Claudio Rebbi, *Interaction energy of superconducting vortices*, Physical Review B **19**, 4486 (1979).

[92] Vincent B. Klaer and Guy D. Moore, *How to simulate global cosmic strings with large string tension*, 1707.05566.

[93] Tetsuo Goto, *Relativistic quantum mechanics of one-dimensional mechanical continuum and subsidiary condition of dual resonance model*, Prog. Theor. Phys. **46**, 1560 (1971).

[94] P. Goddard, J. Goldstone, C. Rebbi, and Charles B. Thorn, *Quantum dynamics of a massless relativistic string*, Nucl. Phys. **B56**, 109 (1973).

[95] Yoichiro Nambu, *Strings, Monopoles and Gauge Fields*, Phys. Rev. **D10**, 4262 (1974).

[96] Christopher T Hill, Alexander L Kagan, and Lawrence M Widrow, *Are cosmic strings frustrated?*, Physical Review D **38**, 1100 (1988).

[97] Alexander Vilenkin, *Cosmic strings*, Phys. Rev. D **24**, 2082 (1981).

[98] Thomas Walter Bannerman Kibble and Neil Turok, *Self-intersection of cosmic strings*, Physics Letters B **116**, 141 (1982).

[99] Neil Turok, *Grand unified strings and galaxy formation*, Nuclear Physics B **242**, 520 (1984).

[100] Neil Turok and Pijushpani Bhattacharjee, *Stretching Cosmic Strings*, Phys. Rev. **D29**, 1557 (1984).

[101] David P. Bennett and Francois R. Bouchet, *High resolution simulations of cosmic string evolution 1. Network evolution*, Phys. Rev. **D41**, 2408 (1990).

[102] Richard A Matzner, *Interaction of u (1) cosmic strings: numerical intercommutation*, Computers in physics **2**, 51 (1988).

[103] Vincent B.. Klaer and Guy D. Moore, *The dark-matter axion mass*, JCAP **1711**, 049 (2017), [1708.07521].

[104] Mark Hindmarsh, Kari Rummukainen, Tuomas V. I. Tenkanen, and David J. Weir, *Improving cosmic string network simulations*, Phys. Rev. **D90**, 043539 (2014), [1406.1688].

[105] P. Weisz, *Continuum Limit Improved Lattice Action for Pure Yang-Mills Theory. 1.*, Nucl. Phys. **B212**, 1 (1983).

[106] G. Curci, P. Menotti, and G. Paffuti, *Symanzik's Improved Lagrangian for Lattice Gauge Theory*, Phys. Lett. **130B**, 205 (1983).

[107] Guy D. Moore, *Improved Hamiltonian for Minkowski Yang-Mills theory*, Nucl. Phys. **B480**, 689 (1996), [hep-lat/9605001].

[108] K. Kajantie, M. Karjalainen, M. Laine, J. Peisa, and A. Rajantie, *Thermodynamics of gauge invariant U(1) vortices from lattice Monte Carlo simulations*, Phys. Lett. **B428**, 334 (1998), [hep-ph/9803367].

[109] Mark Hindmarsh, Joanes Lizarraga, Jon Urrestilla, David Daverio, and Martin Kunz, *Scaling from gauge and scalar radiation in Abelian Higgs string networks*, 1703.06696.

[110] Vincent B. Klaer and Guy D. Moore, "Global string networks and the one-scale model (in preparation).".

[111] C. J. A. P. Martins and E. P. S. Shellard, *Quantitative string evolution*, Phys. Rev. **D54**, 2535 (1996), [hep-ph/9602271].

[112] C. J. A. P. Martins and E. P. S. Shellard, *Extending the velocity dependent one scale string evolution model*, Phys. Rev. **D65**, 043514 (2002), [hep-ph/0003298].

[113] David Daverio, Mark Hindmarsh, Martin Kunz, Joanes Lizarraga, and Jon Urrestilla, *Energy-momentum correlations for Abelian Higgs cosmic strings*, Phys. Rev. **D93**, 085014 (2016), [1510.05006].

[114] Bruce Allen and E. P. S. Shellard, *Cosmic string evolution: a numerical simulation*, Phys. Rev. Lett. **64**, 119 (1990).

[115] Jose J Blanco-Pillado, Ken D Olum, and Benjamin Shlaer, *Large parallel cosmic string simulations: New results on loop production*, Physical Review D **83**, 083514 (2011).

[116] Luca Visinelli and Paolo Gondolo, *Dark Matter Axions Revisited*, Phys. Rev. **D80**, 035024 (2009), [0903.4377].

[117] L. Visinelli and P. Gondolo, *Axion cold dark matter in view of BICEP2 results*, Phys. Rev. Lett. **113**, 011802 (2014), [1403.4594].

[118] Planck collaboration, P. A. R. Ade *et al.*, *Planck 2015 results. XIII. Cosmological parameters*, 1502.01589.

[119] Olivier Wantz and E. P. S. Shellard, *The Topological susceptibility from grand canonical simulations in the interacting instanton liquid model: Chiral phase transition and axion mass*, Nucl. Phys. **B829**, 110 (2010), [0908.0324].

[120] Evan Berkowitz, Michael I. Buchoff, and Enrico Rinaldi, *Lattice QCD input for axion cosmology*, Phys. Rev. **D92**, 034507 (2015), [`1505.07455`].

[121] Peter Petreczky, Hans-Peter Schadler, and Sayantan Sharma, *The topological susceptibility in finite temperature QCD and axion cosmology*, Phys. Lett. **B762**, 498 (2016), [`1606.03145`].

[122] Yusuke Taniguchi, Kazuyuki Kanaya, Hiroshi Suzuki, and Takashi Umeda, *Topological susceptibility in finite temperature (2+1)-flavor QCD using gradient flow*, Phys. Rev. **D95**, 054502 (2017), [`1611.02411`].

[123] Florian Burger, Ernst-Michael Ilgenfritz, Maria Paola Lombardo, Michael Müller-Preussker, and Anton Trunin, *Topology (and axion's properties) from lattice QCD with a dynamical charm*, in *26th International Conference on Ultrarelativistic Nucleus-Nucleus Collisions (Quark Matter 2017) Chicago,Illinois, USA, February 6-11, 2017*, 2017, `1705.01847`, https://inspirehep.net/record/1598136/files/arXiv:1705.01847.pdf.

[124] J. Frison, R. Kitano, H. Matsufuru, S. Mori, and N. Yamada, *Topological susceptibility at high temperature on the lattice*, JHEP **09**, 021 (2016), [`1606.07175`].

[125] Claudio Bonati, Massimo D'Elia, Marco Mariti, Guido Martinelli, Michele Mesiti, Francesco Negro, Francesco Sanfilippo, and Giovanni Villadoro, *Axion phenomenology and θ-dependence from $N_f = 2+1$ lattice QCD*, JHEP **03**, 155 (2016), [`1512.06746`].

[126] Claudio Bonati, Massimo D'Elia, Marco Mariti, Guido Martinelli, Michele Mesiti, Francesco Negro, Francesco Sanfilippo, and Giovanni Villadoro, *Recent progress on QCD inputs for axion phenomenology*, EPJ Web Conf. **137**, 08004 (2017), [`1612.06269`].

[127] Jihn E. Kim, *Weak Interaction Singlet and Strong CP Invariance*, Phys. Rev. Lett. **43**, 103 (1979).

[128] Mikhail A. Shifman, A. I. Vainshtein, and Valentin I. Zakharov, *Can Confinement Ensure Natural CP Invariance of Strong Interactions?*, Nucl. Phys. **B166**, 493 (1980).

[129] Jihn E. Kim, *A COMPOSITE INVISIBLE AXION*, Phys. Rev. **D31**, 1733 (1985).

[130] Patrick Fox, Aaron Pierce, and Scott D. Thomas, *Probing a QCD string axion with precision cosmological measurements*, `hep-th/0409059`.

[131] Malte Buschmann, Joshua W Foster, and Benjamin R Safdi, *Early-universe simulations of the cosmological axion*, arXiv preprint arXiv:1906.00967 (2019).

[132] G. J. Verbiest and A. Achucarro, *High speed collision and reconnection of Abelian Higgs strings in the deep type-II regime*, Phys. Rev. **D84**, 105036 (2011), [`1106.4666`].

[133] Ken D. Olum and Vitaly Vanchurin, *Cosmic string loops in the expanding Universe*, Phys. Rev. **D75**, 063521 (2007), [`astro-ph/0610419`].

[134] Wolfgang Kühnel, *Differentialgeometrie*, vol. 2003. Springer, 1999.

[135] David Garfinkle and Tanmay Vachaspati, *Radiation from kinky, cuspless cosmic loops*, Physical Review D **36**, 2229 (1987).

Danksagung

Ein langer Weg geht mit dieser Arbeit zu Ende und ich möchte mich an dieser Stelle bei allen sehr herzlich bedanken, die mir immer unterstützend zur Seite standen und mir dadurch diesen Weg ebneten.

Zu allererst gilt mein besonderer Dank meinem Doktorvater Guy Moore, der mich über den gesamten Zeitraum stets gefördert und unterstützt hat, so wie immer! Zeit für einen hatte. Insbesondere danke ich für die diversen konstruktiven Gespräche, die auch über die Physik hinaus gingen, die immer sehr aufschlussreich waren und Vermeintlich Probleme in erreichbare Ziele umgewandelt haben.

Für die Annahme meiner Doktorarbeit als zweite Gutachterin und die netten Gespräche sowie Anregungen danke ich ebenso Prof. Dr. Tetyana Galatyuk.

Ebenfalls möchte ich Prof. Dr. Jens Braun für zielführenden Gespräche, die während der PhD-committee meetings stattfanden, sehr herzlich danken.

Für die finanzielle Unterstützung während meiner Promotionszeit danke ich der TU Darmstadt sowie dem Stipendium der Helmholtz-Graduiertenschulen, die mir ebenfalls die Möglichkeiten eröffneten, an spannenden Kursen teilzunehmen. Das alles wäre ohne die freundliche Hilfe von Genette nicht so ohne weitreres möglich gewesen.

Es hat mir immer besonders viel Freude bereitet mit meinen Kollegen Thomas, Niels, Max, Martin und Daniel ein Büro zu teilen und angenehme sowie kontroverse Diskussionen zu führen. Dies gilt ebenso für Jillur und Deniz, die leider nicht immer in unserem Büro sein konnten. Ebenfalls vielen Dank an Genette, für vielfältige Hilfe mit Bürokratie und Verwaltung. Ebenso vielen Dank an Michael, für die netten und interessanten Gespräche.

Große Dankbarkeit empfinde ich bei der Hilfe von Guy, Tina, Riccarda, Kassandra, Verena und Niels, die tatkräftig bei der Fehlersuche in dieser Arbeit geholfen haben.

Das regelmäßige Frühstück freitagsmorgens mit Verena, Tina, Katha, Flo und Simon hat immer einen guten Start in den Tag beschert und so manchen Unmut aufgelöst.

Neben vielen Freunden gilt mein besonderer Dank meinen Eltern Gisela und Ralph, die mich in meinen Vorhaben bisher immer mit großem Engagement unterstützt haben, sowie meinen Geschwistern Kassandra und Riccarda, die immer ein offenes Ohr für ihren kleinen Bruder haben.
Der größte Dank gebührt meiner Verlobten Verena, die immer auf meiner Seite steht, wenn es darauf ankommt und all meine Eigenheiten zu schätzen weiß.

Curriculum Vitae

Name: Vincent Benedikt Klaer
Geburtstag: *30.06.1991
Geburtsort: Duisburg

Werdegang

10.2016 – 11.2019   **Promotionsstudium Physik**
Technische Universität Darmstadt
„Axions, Strings, and Dark Matter Cosmology"

10.2014 – 09.2016   **Master of Science in Physik**
Technische Universität Darmstadt
Master Thesis (betreut von Guy D. Moore):
„Numerical simulations of global and local U(1) string networks"
Nebenfach: Flugsysteme und Flugantriebe sowie BWL

10.2011 – 08.2014   **Bachelor of Science in Physik**
Technische Universität Darmstadt
Bachelor Thesis (betreut von Robert Roth):
„Konsistente Ab-Initio Rechnung der Radien von 4,6,8-He"
Nebenfach: Informatik

10.2010 – 07.2011   **Fachhochschulreife**
Berufskolleg Glockenspitz Krefeld

04.2011   **Ausbildereignung** (Meisterkurs Teil IV)
IHK Düsseldorf

10.2007 – 07.2010   **Chemikant**
Bayer in Uerdingen